



THE HONG KONG
POLYTECHNIC UNIVERSITY

香港理工大學

Pao Yue-kong Library

包玉剛圖書館

Copyright Undertaking

This thesis is protected by copyright, with all rights reserved.

By reading and using the thesis, the reader understands and agrees to the following terms:

1. The reader will abide by the rules and legal ordinances governing copyright regarding the use of the thesis.
2. The reader will use the thesis for the purpose of research or private study only and not for distribution or further reproduction or any other purpose.
3. The reader agrees to indemnify and hold the University harmless from and against any loss, damage, cost, liability or expenses arising from copyright infringement or unauthorized usage.

IMPORTANT

If you have reasons to believe that any materials in this thesis are deemed not suitable to be distributed in this form, or a copyright owner having difficulty with the material being included in our database, please contact lbsys@polyu.edu.hk providing details. The Library will look into your claim and consider taking remedial action upon receipt of the written requests.

**REMOTE SENSING OF MOUNTAIN
GLACIERS OVER THE QINGHAI-TIBET
PLATEAU**

KE LINGHONG

Ph.D

The Hong Kong Polytechnic University

2016

The Hong Kong Polytechnic University
Department of Land Surveying and Geo-informatics

**Remote Sensing of Mountain Glaciers over
the Qinghai-Tibet Plateau**

KE Linghong

A thesis submitted in partial fulfilment of the requirements
for the degree of Doctor of Philosophy

July 2015

CERTIFICATE OF ORIGINALITY

I hereby declare that this thesis is my own work and that, to the best of my knowledge and belief, it reproduces no material previously published or written, nor material that has been accepted for the award of any other degree or diploma, except where due acknowledgement has been made in the text.

_____ (Signed)

KE Linghong (Name of student)

Abstract

The mountain glaciers over the Qinghai-Tibet Plateau (QTP) and its surrounding areas represent an important part of fresh water reserve on the earth. The melt water from these glaciers is critical for water supply for the plateau and feeds many major river systems of Asia. As a key indicator of climate change, glacier change provides an important clue to climate variations in the remote high altitude areas, and impacts various aspects of the environment. In-situ observations of glaciers over the plateau are very limited in spatial and temporal coverages due to the inaccessibility and logistical difficulties, while remote sensing techniques can bridge the gap by providing various information about the glaciers over an extensive region, from different aspects and with regular revisit time. At present, spatial variability of glacier changes and the driving forces over different regions has not been well understood, due to the highly variable topographical and climate conditions which pose challenges for remote sensing techniques. There is necessity to address many key issues in remote sensing of mountain glaciers, such as mapping debris-covered glaciers and estimating glacier mass balances, and more observations are required to improve understanding of the heterogeneity of glacier changes and the mechanisms.

In this context, this thesis illustrates the use of remote sensing techniques for glacier mapping, glacier change detection and mass balance estimates in different parts of the plateau, from the monsoon-influenced southeast to the central inland area and the northwest regions mainly controlled by westerlies. First, a semi-automated method is developed for mapping the clean-ice and debris-covered glaciers over the heavily cloud-affected southeastern (SE) QTP, by integration of multi-temporal and multi-source observations from Landsat satellites and InSAR techniques. The compiled new glacier inventory is a baseline data for exploring the characteristics of glaciers in the SE QTP and for various studies related to glacier changes. In a second study, the ICESat laser altimetry measurements (2003-2008) are deployed to derive elevation changes of the mountain glaciers, with a case study on the Dongkemadi glaciers (DKMD) located in the central QTP. Then with the ICESat data, in combination with observations from the Landsat imagery,

quantitative estimates of glacier elevation changes and mass balances are given over three glacierized regions (SE QTP, DKMD region, and the western Kunlun Mountain (WKM)). The results reveal a contrasting pattern of glacier behaviors over different parts of the plateau in the past decade, from the strongest mass loss of temperate glaciers (-0.72 ± 0.20 m water equivalent per year (w.e.a⁻¹)) in the SE QTP, to moderate mass loss of semi-continent glaciers (-0.42 ± 0.15 m w.e.a⁻¹) over the central plateau and to most significant mass gain of continental glaciers (0.17 ± 0.08 m w.e.a⁻¹) over the WKM in the northwest.

The glacier changes and glacier-climate interactions over the three sub-regions are analyzed separately. For temperate glaciers over the SE QTP, ICESat data reveal strong glacier mass loss (4.71 ± 1.30 Gt a⁻¹, 0.012 ± 0.005 mm sea level rise) and remarkable variability among the sub-regions (ranging from -0.38 ± 0.27 to -1.05 ± 0.36 m w.e.a⁻¹), which is generally consistent with GRACE observations. Faster thinning rate is found over the debris-covered ice (-0.96 ± 0.34 m w.e.a⁻¹) than that of the clean-ice parts (-0.78 ± 0.20 m w.e.a⁻¹). Climatic data at meteorological stations show that the SE QTP experienced dramatic rise of temperature in warm seasons in the past decade ($0.43^\circ\text{C}/10\text{a}$ over 2003-2013), which is probably responsible for the widespread glacier thinning. The difference in precipitation variations and the varying altitudes contributed to the spatial variability of glacier changes.

For sub-continental glaciers over the DKMD region, the study finds significant inter-annual variation of the glacier area which showed sensitive response to local temperature and precipitation variations over 1976-2013. The annual mean temperature exerts strongest impact on the regional glacier changes, despite the high level of precipitation in the recent decade. In contrary to traditional assumptions on the dominant control of the Indian summer monsoon, this study shows that the continental westerly circulations dominate local climate variations and are closely connected with glacier changes in the past decades. The glacier variation shows tele-connection to large-scale atmospheric circulations associated with NAO (North Arctic Oscillation) and ENSO (La Niña) events.

The continental glaciers in the WKM region exhibited high heterogeneity in surface elevation changes, which may be associated with individual glacier parameters including altitude, aspect, glacier hypsometry, ice flow, as well as with glacier surging events which are not directly driven by climate change. The Landsat observations confirm the relatively stable terminus of most glaciers in the WKM in the past 16 years and show three surging events characterized by different pattern of advancements. The pattern of glacier changes is similar to the ‘Karakorum anomaly’ which was found over the Karakorum glaciers in the northwestern QTP, while the overall mass gain in the WKM ($0.20\pm 0.04 \text{ m a}^{-1}$, over 2003-2008) is the highest over the plateau.

The techniques presented in this dissertation promote the use of multi-mission remote sensing observations for glacier mapping and analyzing glacier changes, and the study can be extended to other parts of the plateau. The research results contribute to a better understanding of the challenges in glacier mapping, the complexity and uncertainties of glacier changes, and the effects of the changing climate on the glacier mass balances.

Publications arising from the thesis

This thesis comprises contents from the following papers (published or under review):

Ke, L., Ding, X., & Song, C. (2015). Heterogeneous changes of glaciers over the western Kunlun Mountains based on ICESat and Landsat-8 derived glacier inventory. *Remote Sensing of Environment*, 168, 13-23

Ke, L., Ding, X., & Song, C. (2015). Estimation of mass balance of Dongkemadi glaciers with multiple methods based on multi-mission satellite data. *Quaternary International*, 371, 58-66

Ke, L., Ding, X., Zhang, L., Hu, J., Shum, C.K., & Lu, Z.. Compiling a new glacier inventory for Southeastern Qinghai-Tibet Plateau from Landsat and PALSAR data. (*Journal of glaciology*, in press)

Ke, L., Ding, X., & Song, C. The relationship of glacier wreckage in the central Qinghai-Tibet Plateau to climate change and potential links to atmospheric circulations. (*International Journal of Climatology*, under review)

Acknowledgements

Approaching the end of this Ph.D study, all thoughts lead to my deep gratitude to all the people and events that helped the culmination of this thesis.

Firstly, I would like to express my deepest gratitude to my supervisor: Prof. Xiaoli Ding, a highly respected scientist and gentleman. Thank you Prof. Ding for guiding me into the field of remote sensing and glaciology, and providing an excellent work environment allowing free explore of the fresh research realm and interdisciplinary discussion. I really appreciate the trust and support which has encouraged me to face the challenges and helped me to overcome difficulties at many stages. Also special thanks to my co-supervisor Prof. Janet Elizabeth Nichol who encouraged me to take the opportunity of studying at PolyU and has inspired my dream to become an excellent researcher as well as a graceful lady.

There are so many people at the Hong Kong Polytechnic University (PolyU) who I own thanks for their friendship and support of my work. Lei Zhang, Mi Jiang, Jun Hu, Chisheng Wang and Wu Zhu are all brilliant Ph.D specializing in InSAR techniques, and I appreciate their share of knowledge and expertise in processing and interpreting InSAR data. Special thanks to Lei Zhang and Jun Hu for the unreserved support in my learning of InSAR techniques. I sincerely appreciate my group mates Bochen Zhang, Wenkun Yu for their kindness in both work and life.

I treasure the memory of living with my roommate Anshu Zhang who is such a considerate, smart and hardworking company. I also feel grateful to the staff in the department of Land surveying and Geo-informatics at (PolyU). They are always ready to provide help in various academic and living issues.

I deeply appreciate the Ph.D scholarship of PolyU which made this research possible.

Finally, I would like to express my sincere gratitude to Dr. Chunqiao Song who provided many insightful suggestions for this study. This thesis is dedicated to my parents for their constant love and unreserved support.

Table of contents

Abstract	i
Publications arising from the thesis	iv
Acknowledgements	v
Table of contents	vii
List of tables	x
List of figures	xi
Chapter 1	1
Introduction	1
1.1. Motivation.....	1
1.2. Study area.....	3
1.3. Previous research	6
1.3.1. Glacier mapping and glacier changes over the QTP.....	6
1.3.2. Climate change and glacier-climate relationships	8
1.4. Objectives and organization of the thesis.....	9
Chapter 2	12
Remote sensing of glaciers	12
2.1. Introduction.....	12
2.2. Proxy measures	13
2.2.1. Mapping and extraction of glacier parameters	13
2.2.2. Challenges and limitations.....	17
2.3. Geodetic methods.....	18
2.3.1. Satellite altimetry.....	19
2.3.2. DEMs differencing	19
2.3.3. Gravimetric measurements	21
2.4. Climatic data for studying glacier-climate relationship	23
Chapter 3	27
Compilation of a new glacier inventory for the Southeastern QTP from Landsat and PALSAR data	27
3.1. Introduction.....	27
3.2. Study region and datasets.....	29
3.2.1. Extent of mapped glaciers	29
3.2.2. Landsat imagery.....	30
3.2.3. SAR image pairs.....	31
3.2.4. DEM data.....	32
3.3. Methodology	32
3.3.1. Mapping clean-ice	33
3.3.2. Mapping debris-covered ice	37
3.3.3. Delineation of ice divides	42

3.3.4.	Estimation of ELAs	43
3.3.5.	Creation of manual digitized outlines.....	43
3.4.	Results.....	44
3.5.	Discussion	49
3.5.1.	Glacier inventory data and accuracy.....	49
3.5.2.	Semi-automated debris mapping with coherence	52
3.6.	Conclusions.....	54
Chapter 4	55
Estimates of glacier mass balances over the central QTP with multi-source data....		55
4.1.	Introduction.....	55
4.2.	Study area and datasets	56
4.2.1.	Study area	56
4.2.2.	Datasets.....	57
4.3.	Methodology	59
4.3.1.	Mapping glacier extent and the areal changes	59
4.3.2.	Determination of glacier elevation changes.....	59
4.3.3.	Estimation of glacier mass balances	62
4.4.	Results and discussion	63
4.4.1.	Areal changes	63
4.4.2.	Elevation changes	64
4.4.3.	Volumetric changes and mass balances.....	67
4.4.4.	Uncertainties, limitations and implications	68
4.5.	Conclusions.....	70
Chapter 5	72
Recent glacier changes in the southeastern QTP and the climate forcing.....		72
5.1.	Introduction.....	72
5.2.	Study area.....	73
5.3.	Data and methods.....	77
5.3.1.	ICESat data and glacier thickness changes.....	77
5.3.2.	GRACE data and regional mass variations.....	78
5.3.3.	Climate data and climate change analysis	79
5.4.	Results.....	80
5.4.1.	Glacier surface elevation changes over 2003-2008	80
5.4.2.	Climate change over the SE QTP during 1992-2013	85
5.4.3.	Analysis of climate forcing on the glacier mass balances	87
5.5.	Discussion	89
5.5.1.	ICESat-based glacier changes.....	89
5.5.2.	GRACE observations.....	92
5.6.	Conclusions.....	93

Chapter 6	95
Glacier-climate interactions in the DKMD region, central QTP	95
6.1. Introduction	95
6.2. Study area	96
6.3. Datasets and methods	98
6.3.1. Landsat images over 1976-2013	98
6.3.2. Local climatic variables and reanalysis data	99
6.4. Results	100
6.4.1. Glacier area changes over 1976-2013	100
6.4.2. Long-term variation of temperature and precipitation	102
6.4.3. Relationship between glacier variation and climate variables	103
6.4.4. Correlations between climate variables	105
6.5. Discussion	107
6.5.1. The sensitivity of glacier variations to local climate change	107
6.5.2. Potential links among glacier variation, local climate and atmospheric circulations	108
6.6. Conclusions	111
Chapter 7	113
Heterogeneity of glacier changes in the West Kunlun Mountain region	113
1.1. Introduction	113
1.2. Study area	114
1.3. Data and methods	116
1.3.1. Mapping glacier inventory	116
1.3.2. Elevation trends from ICESat data	118
1.3.3. Glacier terminus changes based on Landsat data	119
1.4. Results	120
1.4.1. Glacier distribution	120
1.4.2. Glacier thickness changes	122
1.4.3. Glacier surging and terminus changes	127
1.5. Discussion	131
1.5.1. Glacier inventory data and accuracy	131
1.5.2. Uncertainties and implications of glacier dynamics	132
1.6. Conclusions	133
Chapter 8	135
Conclusions and outlook	135
Appendix	139
References	146

List of tables

Table 2.1 General parameters of main Landsat satellites/sensors.....	14
Table 2.2 The characteristic of spectral channels for L5 and L7	14
Table 3.1 List of satellite data used for mapping SE QTP glaciers	31
Table 3.2 glacier parameters per sub-region of SE QTP. ELA values are estimated based on inflection of elevation contour lines on the topographic map (SRTM DEM).	48
Table 4.1 List of Landsat images used in this study	58
Table 4.2 Distribution of footprints in autumn (October/November).....	65
Table 5.1 Annual mean temperature and precipitation totals at the 10 stations around the study area. Values are based on the period of 1992-2013.....	75
Table 5.2 Glacier elevation changes in SE QTP and mass balances for the clean ice area, debris-covered parts and the whole glacier areas.	81
Table 5.3 Statistics of glacier area, the number of ICESat measurements, and trends of glacier elevation changes and mass balances over 2003-2008 for selected sub-regions.....	85
Table 6.1 List of Landsat images used in this study. Images marked with • are partly cloud covered and those marked with * were used for reference	98
Table 6.2 Correlation between glacier area and climate variables.....	104
Table 6.3 Correlation matrix of relationships between climate variables after de-trending the original time series data.	106
Table 7.1 List of Landsat scenes used in the WKM region	117
Table 7.2 Trends of elevation differences (dh) for different parts of the glaciers based on multi-season ICESat measurements and general statistics about glaciers. The, N, S and C denotes the northern, southern and central parts respectively. Bold numbers indicate trends are significant at 95% significance level.....	124

List of figures

Fig. 1.1 Overview of glacier distribution over the Qinghai-Tibet Plateau (QTP) and the location of study region.	4
Fig. 1.2 Multi-year mean 2 m air temperatures in warm season (May to October) (a) and cold season (November, December, January to April) (b), mean precipitation totals in warm season (c) and cold season (d) over 2001-2012 as resolved by the 10 km High Asia Reanalysis data.	5
Fig. 2.1 Distribution of weather stations in and around QTP	24
Fig. 3.1 Overview of the study area and satellite data including Landsat 8/OLI images in false color composite (RGB 754 for Landsat 8) and the frame of PALSAR images.	30
Fig. 3.2 Selected key processing steps in clean-ice mapping: clean-ice mask (a) and water mask (b).....	34
Fig. 3.3 Distribution of mean slope of all water polygons in the study area.....	36
Fig. 3.4 Schematic workflow for mapping clean ice and debris-covered parts in the SE QTP.....	38
Fig. 3.5 Illustration of key processing steps in debris mapping.....	40
Fig. 3.6 Distribution of NDVI in one Landsat scene	41
Fig. 3.7 Comparison of basins derived from SRTM DEM (red lines), ASTER DEM (white lines) and manually corrected divides (yellow lines).	43
Fig. 3.8 Distribution of the number of glaciers (in %), glacier area (in %), and mean glacier elevations in m, (a) per size class, (b) per aspect sector.....	45
Fig. 3.9. Spatial distribution of inventoried glaciers (including the debris-covered parts and clean-ice parts) and data gaps where images are always cloud covered.	46
Fig. 3.10. Hypsometry of all glaciers in the study region.	46
Fig. 3.11. Map of mean glacier elevation of individual glaciers and the relative amount of debris cover in different elevation ranges.....	47
Fig. 3.12. Contour maps for typical glaciers in SE QTP and the estimated ELA.	49
Fig. 3.13. The 2013 glacier inventory generated in this study compared with a couple of manually digitized glacier outlines and the second CGI (CGI2).	51
Fig. 3.15 An illustration of challenging conditions for identifying debris-covered ice over the SE QTP.	53
Fig. 4.1 Overview of the study region and glaciers the Tanggula Mountains, in the central QTP and the crossing ICESat tracks.	57
Fig. 4.2 Variation of glacier area in the DKMD reigon from 2000 to 2011.	64

Fig. 4.3 Robust fit of linear relationship between elevation differences and SRTM for different laser periods (a)~(f), for all measurements (g), and (h) for off-glacier footprints.	66
Fig. 4.4 The over-glacier elevation difference trends based on mean values before and after correction and the off-glacier elevation difference.	66
Fig. 4.5 Comparison of volume changes since 2000 derived from volume-scaling model with ICESat-based estimates.	67
Fig. 4.6 Comparison of in-situ cumulative mass balance with mass balance based on ICESat data (a) and with volume-scaling model (b).	68
Fig. 5.1 Overview of the southeastern QTP, location of the climate stations (circles) and ICESat data coverage.	74
Fig. 5.2 Climate diagrams showing five typical climate characteristics at five weather stations. The statistics is based on the period of 1992-2013.	76
Fig. 5.3 Mean elevation difference between ICESat and SRTM (dh) for each laser period and the trends over the clean-ice parts (a) and debris-covered parts (b).	82
Fig. 5.4 Mean elevation difference (dh) and estimated trends for selected sub-regions of the SE QTP.	83
Fig. 5.5 Trends of elevation differences between ICESat and SRTM, for each sub-region and individual cells in the SE QTP, in comparison to in situ mass balance measurements of the Parlung glaciers ($-1.1 \text{ m w.e.a}^{-1}$ equivalent to -1.3 m a^{-1}).	84
Fig. 5.6 Time-series and linear fitting of mean anomalies of climatic variables: (a) the mean summer temperature, (b) mean winter temperature, (c) mean summer precipitation, (d) mean winter precipitation.	86
Fig. 5.7 Changes of temperature and precipitation in warm seasons over 1992-2013, measured at the ten stations.	87
Fig. 5.8 Mean annual glacier thickness changes in the SE QTP in relation to mean summer temperature anomaly and summer precipitation anomaly.	88
Fig. 5.9 Linear fitting of mean annual glacier thickness changes in the SE QTP with respect to summer temperature anomaly.	88
Fig. 5.10 ICESat footprint distribution in each sub-region (A, B, C, D, E and F).	90
Fig. 5.11 ICESat footprint distribution over the clean ice and debris-covered in terms of elevation (a) and slope (b).	91
Fig. 5.12 Spatial pattern of mass budgets between 2003 and 2009 in the SE QTP derived from the GRACE gravimetry observations.	92
Fig. 5.13 Comparison of over-glacier thickness changes (mean dh) with the regional mass anomaly from GRACE observations.	93
Fig. 6.1 The glaciers in the DKMD region in central Qinghai-Tibet Plateau and the influence of atmospheric circulations.	97

Fig. 6.2 Inter-annual variability in glacier area (a) in relation to temperature (b), precipitation (c), winter Southern Oscillation Index (SOI) (e), North Atlantic Oscillation (NAO) (d), and Indian Monsoon Index (IMI) (f) over 1976-2013.	101
Fig. 6.3 Time-series variation in winter mean temperature (T_winter) and winter total precipitation totals (P_winter) between 1976 and 2013.....	102
Fig. 6.4 The relationship between glacier area and annual temperature in the DKMD region.	103
Fig. 6.5 The relationship between average thickness changes and the annual temperature (a) and winter precipitation (b) between 2003 and 2008	105
Fig. 6.6 Three-year moving averages of time-series climatic variables: (a) NAO and summer temperature; (b) NAO and summer precipitation; (c) SOI and winter temperature and (d) SOI and winter precipitation.....	107
Fig. 7.1 Overview of the study area in the Western Kunlun Mountains (WKM)...	116
Fig. 7.2 Glaciers over the WKM on the false-color composite (RGB from Band 754) of Landsat 8/OLI images and the coverage of ICESat footprints.	117
Fig. 7.3 Distribution of the number of glaciers (yellow), glacier area (green), and mean glacier elevations (circles), (a) per size class. (b) per aspect sector.	121
Fig. 7.4 Map of the inventoried glaciers and the mean glacier elevations.	122
Fig. 7.5 Trends of elevation differences between ICESat and SRTM (dh) over 2003–2008 for different glaciers and glacier accumulation/ablation parts in the WKM area.....	123
Fig. 7.6 Elevation trends of different glaciers in relation to mean elevation (a) and aspect (b).....	125
Fig. 7.7 Distribution of ICESat footprints within different parts of glaciers and the linear trends: the Kunlun glacier (Glacier ID 109, upper row) and the northern Guliya Ice caps (Glacier ID 112, lower row).	126
Fig. 7.8 Glacier surging detected by ICESat over the Zhongfeng Glacier.....	128
Fig. 7.9 Trends for different parts of the Zhongfeng Glacier in the caves in the accumulation area (a), and other accumulation regions(b).	128
Fig. 7.10 Glacier terminus changes between 1998/1999 and 2013. Significant retreat or advancement is shown with black dots at approximate location of the examined frontals.	129
Fig. 7.11 Glacier surging during 1998/1999 and 2013 for three glaciers: glacier ID 70 (left), glacier ID 133 (middle) and glacier ID 64 (right).	130
Fig. 7.12 Illustration of problems in previous glacier outlines (RGI is same with GLIMS and CGI1).	131

Chapter 1

Introduction

1.1. Motivation

The mountain glaciers over the Qinghai-Tibet Plateau (QTP) and its surrounding areas represent an important part of fresh water reserve on the earth. These glaciers are located in the headwaters of many major river systems of Asia, including the Yangtze, Yellow River, Lancang, Yarlung Tsangpo, Indus and Ganges, and make important contributions to water sources for the river upper reaches, particularly during dry seasons. Billions of people living in the downstream regions depend to a varying extent on the refresh water supply. The QTP is thus referred as the 'Asian Water Tower' (Immerzeel et al., 2010). Furthermore, glaciers show sensitive response to climate forcing, and changes in glacier mass balances are considered as key indicators for climate variability (Dyurgerov & Meier, 2000). Thus changes of mountain glaciers provide important clues for climate variations in the remote and high-altitude areas with rare or non-existent meteorological observations. In the context of warming climatic in recent decades, the glacier mass loss has raised wide concerns about the environmental, social and economic impacts. In particular, there are growing concerns about the influence of glacier changes on regional water supplies, contribution to sea level rise and outburst of natural hazards such as glacial lake outburst flooding and serious glacial debris flow hazards (Kehrwald et al., 2008, Immerzeel et al., 2010, Bolch et al., 2012). In order to assess the impacts, it is crucial to derive adequate observations of the ongoing glacier changes, in particular the mass balances of glaciers over the QTP.

Observations of mountain glaciers over the QTP are yet far from sufficient. There is lack of information on the numerous climatic, topographic and glaciological parameters that can be closely connected with glacier distribution and fluctuations. In-situ field observations of such climatic and glaciological information, as well as mass balance measurements, are

sparse and limited to a small number of sites over the plateau, mainly due to complex terrain, logistic difficulties (accessibility and costs) and geopolitical reasons in performing in-situ surveys. The increasing availability of multi-mission remote sensing observations enables mapping and monitoring glaciers over an extensive region, from different aspects and with regular revisit time (e.g. Andreassen et al., 2008, Bhambri et al., 2011, Veettil, 2012). Although remote sensing observations have provided evidences of significant glacier changes and the spatial variability over the QTP (e.g. Yao et al., 2012, Bolch et al., 2012), the cause of heterogeneous glacier changes and the relationship between climate forcing and glacier variation over different regions are not well understood. Applying remote sensing for depicting a clear picture about glacier changes and the driving forces is still challenged by 1) limitations of different remote sensing techniques due to inherent sensor limitations (e.g. spatio-temporal gaps in the coverage, cloud cover and sensor saturation), 2) complex mapping conditions (complicated terrain and varying landscapes), and 3) integrated analysis of different source of observations with varying spatial and temporal resolution and observing aspects (area, length, velocities, mass balances, etc.). In particular, mapping debris-covered glaciers and estimating glacier mass balances are challenging issues in remote sensing studies.

Recent remote sensing studies have shown the potential of extracting glacier information based on new data such as SAR (Synthetic Aperture Radar) observations (e.g. Atwood et al., 2010, Frey et al., 2012) and deriving mass balance estimates of mountain glaciers from new satellite observations such as the laser altimetry (e.g. Kääb et al., 2012, Gardner et al., 2013, Neckel et al., 2014) and satellite gravimetry (e.g. Chen et al., 2006, Jacob et al., 2012, Yi & Sun, 2014). The availability of climatic observations from meteorological stations and reanalysis data also contributes to further investigation into the response of glaciers to climate change.

There is a need for detailed information about QTP glaciers, including the climate dynamics, glacier distribution and characteristics, regional glacier mass balances, and landscape

factors that control the accumulation and ablation. In this context, this dissertation illustrates the use of remote sensing techniques for glacier mapping, glacier change detection and mass balance estimates in different parts of the plateau, from the monsoon-influenced southeast to the central inland area, and to northwest where the westerlies dominate. The techniques presented here promote the use of multi-mission remote sensing observations for mapping and analyzing glacier changes, and can be extended to other parts of the plateau. With the case studies, this thesis attempts to improve understanding of the characteristics of glaciers in different climate regimes of the plateau, their behaviors in recent years and the possible driving forces.

1.2. Study area

The QTP, also known as the Tibet Plateau (TP) in some literature, is the highest plateau on the earth, with mean altitude above 4500 m a.s.l. and a total area about 2.5 million km² (Fig. 1.1). The plateau lies in the region between 26°N - 38 °N latitude and 76°E - 102°E longitude, and normally defined within the territory of China, surrounded by the Himalayas in the south and the Pamir and Karakoram in the northwest (Fig. 1.1). As a result of collision and post-collisional convergence of the Indian subcontinent with Eurasia at ~50 Ma (Royden et al., 2008), the plateau is still uplifting in contemporary times (Shen et al., 2001, Clark et al., 2005, Royden et al., 2008). With the crustal moving and uplift, high relief topography are found along the southern and eastern margins of the plateau including the Nyainqêntanglha Ranges, the Transhimalaya, and the Himalayas; while the central and northern part of the plateau is relatively flat with low terrain gradients (Fielding et al., 1994). A number of major Asian rivers originate from the southern and eastern plateau, including Yarlung Tsangpo (Brahmaputra), Salween (Nu River), Lancang River (Mekong), Yangtze and Yellow River (Fig. 1.1).

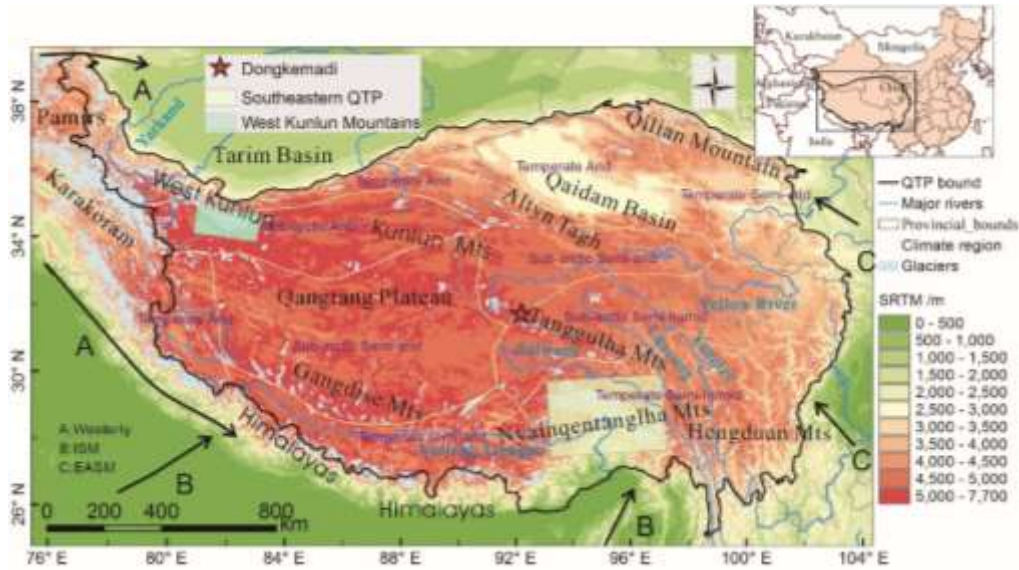


Fig. 1.1 Overview of glacier distribution over the Qinghai-Tibet Plateau (QTP) and the location of study region.

The QTP is commonly referred as the ‘Roof of the World’, which implies its significant influences on regional environment through thermal forcing mechanisms (Duan & Wu, 2005). The great mountain ranges act as natural barriers and affect large-scale atmospheric circulations including the westerlies and the Asian summer monsoons (the Indian summer monsoon (ISM) and the East Asian summer monsoon (EASM)) (Kutzbach et al., 1993, Zhisheng et al., 2001, Liu & Yin, 2002). The three atmospheric circulations dominate in different seasons over different regions, resulting in strong seasonality and spatial variability of climate over the plateau (Tian et al., 2007). In winter, the mid-latitude circulation systems are dominant over the QTP and there is little precipitation except for some parts of the western plateau; while in summer, the ISM and EASM bring heavy rainfalls to the southern and eastern plateau, resulting in relatively humid climate over these regions (Xu et al., 2011, Yao et al., 2012). Such contrasted spatial variability of precipitation in warm and cold season is well reflected in Fig 1.2, which is based on the 10 km High Asia Reanalysis (HAR) data (Maussion et al., 2014). The annual precipitation totals decrease from about 1000 mm in the southeast to less than 50 mm in the Tarim basin. There are also strong gradients for the mean seasonal temperatures which reach over 5 °C (-10°C) in the southeast in summer (winter) to below -10°C (-20°C) in the northwestern

part of the plateau (Fig. 1.2).

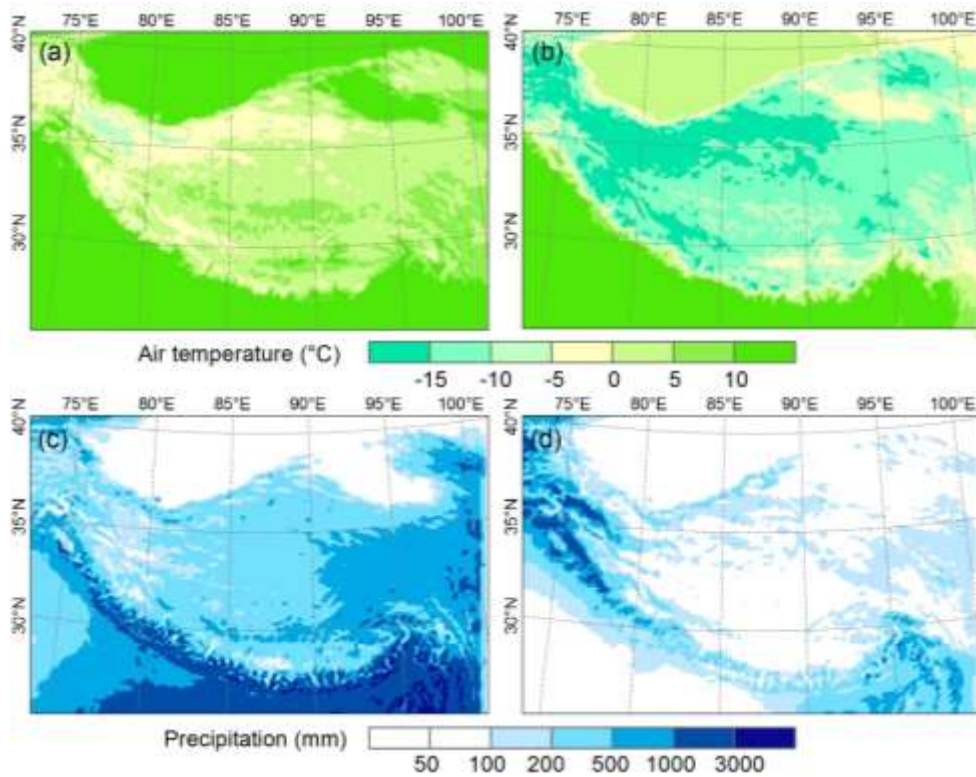


Fig. 1.2 Multi-year mean 2 m air temperatures in warm season (May to October) (a) and cold season (November, December, January to April) (b), mean precipitation totals in warm season (c) and cold season (d) over 2001-2012 as resolved by the 10 km High Asia Reanalysis data.

The spatial-temporal pattern in precipitation and temperature determines different characteristics of glaciers across the plateau, for example, varying thermal and accumulation regimes. According to the thermal regime, glaciers over the QTP can be divided into three categories: monsoonal (temperate) type, sub-continental (sub-polar) type and continental (polar) type. Different types of glaciers show distinguished features in terms of ablation and accumulation periods, ice velocity and sensitivity to temperature and precipitation changes (Oerlemans & Fortuin, 1992, Dyurgerov & Meier, 2000, Fujita, 2008). Temperate glaciers are mainly distributed in southeastern QTP including the east Himalayas and the middle and east Nyainqêntanglha Range, while continental glaciers are presented in the extremely cold and dry northwestern plateau, mainly over the western Kunlun Mountains, eastern Pamirs, western Tanggulha Mountains, and western Qilian Mountains. In the central plateau, sub-continental glaciers are widely distributed over the

eastern part of ranges including the Kunlun Mountains, Tanggulha Mountains and Gangdise Mountains. While temperate glaciers gain most of their ice accumulation in summer seasons and have long and less concentrated ablation season, most polar-type glaciers gain accumulation in winter seasons and have concentrated ablation season from May to September (Shi et al., 2000, Shi & Liu, 2000, Shen, 2004).

1.3. Previous research

1.3.1. Glacier mapping and glacier changes over the QTP

First scientific observations of glaciers over the QTP were obtained by cartographic expeditions and in-situ field surveys. The Chinese glaciologists started field investigations on several glaciers since the 1960s and intensive topographic mapping and aerial photogrammetric surveys were conducted from the 1950s to the 1980s (Li & Cheng, 1978). The first Chinese Glacier Inventory (CGI) was initiated in 1979 and completed in 2002 based on topographical maps and aerial photographs acquired from the 1950s to the 1980s (Shi et al., 2010). According to the first CGI, there are about 36,800 glaciers over the plateau, covering a total land area of 49,873 km² and having a total volume of about 4,561 km³ (Yao et al., 2007). The first CGI was then incorporated into the world glacier inventory such as GLIMS (Global Land Ice Measurements from Space) and RGI. The latter two glacier inventories updated glacier outlines with Landsat imagery in parts of the Karakorum and Himalaya regions, while over the main inland QTP the three glacier inventories are similar and the glacier outlines suffer from errors such as location shift and shape distortion, due to inaccurate geometric basis of the source data and overestimation of glacier extents by mistaking extensive snow cover for permanent ice (Pfeffer et al., 2014).

In recent years, glacier mapping over the QTP has been improved by using contemporary satellite observations, particularly with optical imagery from the Landsat satellite series. Updating the glacier inventory has been conducted over some clean ice glaciers with a purpose on detection of glacier area changes (e.g. Bolch & Kamp, 2006, Ye et al., 2006,

Shangguan et al., 2007, Bolch et al., 2010a). The investigated regions are mainly in the central or western parts where the influences of summer monsoon are less prominent, while there are few efforts on glacier mapping in areas with frequent cloud cover and seasonal snow cover such as the most glacierized region in the southeastern QTP. Mapping debris-covered glacier over the plateau has been challenging, and previous applications mainly rely on manual digitization (e.g. Frey et al., 2012). Several studies employed semi-automated methods based on thermal data or in combination with high-accuracy DEM, and most of them were applied for one or several small glaciers in the Himalayas (Paul et al., 2004, Shukla et al., 2010). At present, updating glacier inventory for the QTP, particularly for the monsoon-influenced temperate glaciers and the debris-covered ice, requires further efforts.

Since the 1990s, the retreat of glaciers and negative mass balances have been reported based on the in-situ field investigations (Yao et al., 2007, Kang et al., 2010). In recent decades, with increasing observations from optical sensors, a number of studies have investigated the glacier area or length changes by comparing new glacier extents with historical maps or aerial photographs (e.g. Su & Shi, 2002, Ding et al., 2006, Ye et al., 2006, Shangguan et al., 2007, Yao et al., 2007, Massif & Ladakh, 2012). These studies showed spatial variability of glacier area and length, with the most serious retreat in the southeastern QTP and eastern Himalayas, in comparison with slight retreat or advance of glaciers in the central and northwestern part of the plateau. The regional difference of glacier changes was also confirmed by Yao et al. (2012) with analysis on glacier area changes of 82 glaciers between the 1970s and 2000 and mass balance estimates of 15 glaciers over 2006-2010.

Geodetic method by examining glacier surface elevation changes was also applied for several glaciers with elevation measurements acquired in different years. Li et al. (2010) reported an average thinning rate of -0.67 m a^{-1} during 1970s-2000 for the Da Dongkemadi glacier (DDG) in the central QTP by comparing the difference of DEM acquired from

historical topography maps and the C-band SRTM (Shuttle Radar Topography Mission). A recent study estimated global glacier mass changes by combining in situ mass balance measurements, ICESat data and observations from the Gravity Recovery and Climate Experiment (GRACE) (Gardner et al., 2013). For the QTP, the glacier mass balances over 2003-2009 derived from ICESat (Gardner et al., 2013) show similar spatial patterns with the results from Yao et al. (2012). These large-scale spatial variability over the QTP was also discussed with GRACE-derived mass balance estimates (Matsuo & Heki, 2010, Jacob et al., 2012). However, in comparison with other sources of data, the exact glacier mass balances from GRACE might have large uncertainty over some regions (Yao et al., 2012, Bolch et al., 2012), due to misinterpretation of signals from surrounding regions and other physical process including changes of snow cover, precipitation, river discharges and lakes in endorheic basins (Immerzeel et al., 2009, Zhang et al., 2013, Song et al., 2014) . Hence it is important to investigate the present changes in glacier volume in much more detail for a reliable estimate of the released melt water from glaciers in different regions of the plateau (Ding et al., 2006; Kang et al., 2010).

1.3.2. Climate change and glacier-climate relationships

Many studies have shown significant warming trends in the QTP during the last half century, based on observational data from meteorological stations, remote sensing data and reanalyses of existing datasets (Liu & Chen, 2000, Niu et al., 2004, Liu et al., 2006, You et al., 2008, Zhang et al., 2007, Rangwala et al., 2010). The linear rates of temperature increase during 1955–1996 are about 0.16 °C/decade for the annual mean and 0.32 °C/decade for the winter mean, which exceed those for the Northern Hemisphere as a whole and for the same latitudinal zone (Liu & Chen, 2000). Several studies noted the temporal and spatial variability of climate change over the QTP. The most pronounced characteristics is varying rates of warming and the inverse trends of precipitation over the south and north (Yin et al., 2000, Niu et al., 2004). The southeastern and southwestern parts of QTP becomes warmer and wetter over 1961-1998; while the northeastern part of QTP turned warmer and drier (Niu et al. 2004). In the temporal span, warming in winter and

summer has been found to be more significant than that in spring (Liu et al., 2006, Jun, 2001, Niu et al., 2004). Rangwala et al. (2009) found that spring and summer months appeared to have warmed rapidly between 1991 and 2000. The reported results tend to be slightly different with use of other datasets and focus on different study periods.

Recently, regional or large-scale atmospheric circulations have been linked with the climate variability in the QTP (You et al., 2010, Yao et al., 2012, Yin et al., 2000), and show significant contributions to glacier dynamics over different regions (Kang et al., 2002, Thompson et al., 2006, Kang et al., 2007, Wang et al., 2007, Kang et al., 2010). The precipitation decrease in the Himalayas is suggested to be linked with the weakening trend of ISM, which may deteriorate the recessing state of glaciers in the eastern and central Himalayas, whereas the weak recessing state or advance of glaciers in the Karakoram and eastern Pamir regions might be attributable to the increased precipitation due to strengthening westerlies (Yao et al., 2012). However, the influence of atmospheric circulations is rather complex due to the high relief, complex topography and unique environment in and around QTP, and the dominating atmospheric circulations over different parts of QTP is still unclear. Glacier dynamics on regional or local scales, and the explanations for the changes (both climatic and non-climate related) require further investigations.

1.4. Objectives and organization of the thesis

The apparently insufficient research on glaciers over the QTP stresses the necessity for more investigations into glacier parameters and their changes. It is also necessary to compare and combine different measurements to enrich knowledge about glacier variations from different perspectives and to resolve controversies about status and rates of glacier changes across the QTP. The main objective of this dissertation is to quantify and interpret glacier characteristics, recent glacier changes and their sensitivity to climate change over the QTP. The results will contribute to better understanding of the pattern, the relationships

between glacier changes and the driving forces of glacier dynamics over different regions of the plateau. For this purpose, various remote sensing observations including optical imagery, SAR, satellite altimetry and gravimetry are explored and results from different data and approaches are compared and evaluated. Glacier changes are analyzed on fine spatial scales over three regions, southeastern (SE) QTP, DKMD region in central QTP and west Kunlun Mountains (WKM) in the northwestern QTP. The three regions cover the southeast-northwest climatic and topographic gradient and with different glacier types (temperate, sub-continental, and continental) (Fig. 1.1). Furthermore, the patterns of glacier changes over each sub-region and the possible driving mechanisms are analyzed, with a focus on the glacier-climate relationship. Specifically, the structure of the dissertation is organized as follows:

Chapter 1 highlights the significance of the research topic and gives an introduction to the study area, a short review of previous research, the research objectives and the structure of the thesis.

Chapter 2 gives a short introduction to the various data and methods for glacier mapping and glacier change investigations, with a focus on the application of remote sensing techniques.

Chapter 3 presents a semi-automated method for the generation of complete glacier inventory over the extensive and densely glacierized southeastern QTP, based on integration of multi-temporal Landsat scenes and InSAR coherence observations.

Chapter 4 discusses the suitability of ICESat elevation data in determining thickness changes of mountain glaciers, with a test over the DKMD glaciers located in the central QTP.

Chapter 5 presents the quantification and interpretation of mass balances of temperate

glaciers over the southeastern QTP based on ICESat measurements and GRACE observations, followed by analysis on the sensitivity of glacier changes to local climatic dynamics based on meteorological observations.

Chapter 6 analyzes long-term glacier area variations (1970s-2013) over the DKMD region and the relationship with local climatic variables and large-scale atmospheric circulations.

Chapter 7 depicts special behavior of continent glaciers over the west Kunlun Mountains (WKM) in the northwestern QTP, which is characterized by significant mass gain in recent years, high spatial heterogeneity and glacier surging. The possible mechanisms and implications are discussed.

Chapter 8 concludes the dissertation and gives an outlook on future research on monitoring glaciers over the TP.

Chapter 2

Remote sensing of glaciers

2.1. Introduction

In remote areas such as the glacierized region where physical access is difficult, remote sensing seems to be the only practical approach for assessing regional glacier mass balances (Bamber & Rivera, 2007). According to the characteristics of observations, there are two different ways to estimate mass balance based on remote sensing data, proxy measures and geodetic methods. Proxy measures refer to one-dimensional or two-dimensional (2D) information (area, length) or indicators (e.g. ELA: Equilibrium-Line Altitude), which are mainly derived from glacier mapping, to infer mass balance indirectly; while space geodetic methods are based on various geodetic measurements (surface elevation changes or mass change) to estimate glacier mass balances in a relatively direct way (Bamber & Rivera, 2007, Racoviteanu et al., 2008a). Geodetic measurements can be derived from satellite altimetry data, InSAR and satellite gravimetry observations. Proxy measures and geodetic methods are distinguished in terms of observed variables, data acquisition techniques and analyzing methods.

This chapter presents datasets and methods involved in the mapping and monitoring of glaciers over the QTP, focusing on their basic principles, advantages and challenges. Firstly proxy measures are introduced, with a focus on deriving glacier parameters from optical images of Landsat satellites. Then geodetic methods are introduced, highlighting the potential of glacier mass balances based on elevation data from satellite altimetry and DEM difference, and mass anomaly from GRACE. The last section describes common data and indicators used for analyzing local climatic changes and large scale atmospheric circulations.

2.2. Proxy measures

2.2.1. Mapping and extraction of glacier parameters

Glacier mass balances can be inferred from changes of various glacier parameters, such as glacier terminus, length, area, median elevations, ELA, and hypsometry maps. Currently these parameters are generally extracted from multispectral satellite images in combination with DEMs in a GIS (Geographical Information System) environment. Since 1970s, optical imagery of medium resolution (10-90 m) can be derived from different spaceborne sensors including Landsat MSS (Multispectral Scanner System) /TM (Thematic Mapper) /ETM+(Enhanced Thematic Mapper Plus), ASTER (Advanced Space-borne Thermal Emission and Reflection Radiometer), LISS (Linear Imaging Self Scanning Sensor), SPOT (System Pour l'Observatoire de la Terre) and the recent ALOS AVNIR-2 (Advanced Land Observing Satellite). Other optical sensors such as IKONOS, Quickbird and GeoEye-1 provide satellite imagery with meter and sub-meter spatial resolution, are suitable for glacier studies at basin scales. However, the high costs, narrow swath size long revisit intervals of a few months limit their use at large spatial scales. Sensors with medium spatial resolutions are capable of acquiring data in multispectral mode, with relatively large swath widths (185 km for Landsat, and 60 km for ASTER) and short revisit times (16 days for ASTER), makes them useful for regular glacier mapping over wide areas. In particular, Landsat satellite series provide multi-spectral optical images with the longest record of satellite-based observations (1972 to current) of earth surface among all the satellites onboard with optical sensors, and are of high value for retrieving glacier parameters and the changes in a long time span. ASTER images are also suitable for monitoring of glacier parameters with high spectral resolution and spatial resolution (15m), but the temporal span of data is limited in the past decade (February 2000 to present).

The Landsat satellite series consists of seven satellites that have been successfully sent into the space. The earliest Landsat data from MSS sensors can be dated back to 1978, and have a coarser resolution than the followed TM/ETM sensors (Table 2.1). The parameters of

Landsat satellite series are listed in Table 2.2). Landsat 5 and landsat 7, and the recently launched Landsat 8 are operational in the orbit. With improved stability and quality, the number of useful images from TM and ETM is higher than that from previous sensors. The two sensors also share similar characteristic of spectral channels (Table 2.2). Note that all ETM+ images from Landsat 7 acquired after May 2003 have an anomaly caused by the failure of the scan line corrector (SLC), resulting in 22% data loss of one scene on average. Landsat 8 started normal operations on May 30, 2013, and provides images with more spectral bands and improved signal to noise radiometric performance, enabling better characterization of land cover state and condition (U.S. Geological Survey, 2013).

Table 2.1 General parameters of main Landsat satellites/sensors

Satellite	Main sensors	Launch date	Decommission	Revisit cycle (Days)	number of bands	Spatial resolution (panchromatic/thermal bands) (m)
L1	MSS	23-Jul-72	7-Jan-78	18	4	60
L2	MSS	22-Jan-75	25-Feb-82	18	4	60
L3	MSS	5-May-78	31-Mar-83	18	4	60
L4	MSS	16-Jul-82	30-Jun-01	16	7	60
L5	TM	1-Mar-84	Operational	16	7	30 (~120)
L7	ETM+	15-Apr-99	Operational	16	8	30 (15/60)
L8	OLI	11-Feb-13	Operational	16	9	30 (15)
	TIRS				2	100

Table 2.2 The characteristic of spectral channels for L5 and L7

Band number	Band type	L5 TM		L7 ETM+	
		Band region/ μm	Spatial resolution/m	Band region/ μm	Spatial resolution/m
1	Blue~green	0.45~0.52	30	0.450~0.515	30
2	Green	0.52~0.60	30	0.525~0.605	30
3	Red	0.63~0.69	30	0.630~0.69	30
4	Near IR	0.76~0.90	30	0.775~0.90	30
5	SWIR	1.55 ~ 1.75	30	1.550~1.75	30
6	LWIR	10.4 ~ 12.	120	10.40~12.5	60
7	SWIR	2.08 ~ 2.35	30	2.090~2.35	30
8	Pan			0.520~0.90	15

Manual digitization was firstly used to delineate glacier outlines from aerial photographs

and satellite images, but this method is time-consuming for extensive areas and subject to human errors. Various semi-automated or automated mapping methods have been developed by exploring spectral characteristics of glaciers on optical images. Such methods mainly comprise band combination techniques (various forms of band ratio and thresholds of reflectance), unsupervised classification and supervised classification techniques. Among these, the band combination techniques have been proved to be a well-established procedure for clean-ice mapping for their straightforward implementation and high effectivity.

Automatic band combination techniques delineate clean ice by employing spectral characteristics of snow/ice in the visible and near-IR part of the electromagnetic spectrum (Landsat TM bands 2, 4 and 5). As snow and ice are characterized by high reflectivity (albedo) in the visible wavelengths (0.4–0.7 μ m) and low reflectance at short-wave IR channel (0.8–2.5 μ m), single band ratios such as TM3/TM5, TM4/TM5 and the Normalized Difference Snow Index (NDSI) $((\text{Green}-\text{SWIR})/(\text{Green}+\text{SWIR}))$ can effectively distinguish the bright areas (snow and ice) from surrounding non-glacier dark areas such as rock, soil and vegetation (Hall et al., 1995b, Racoviteanu et al., 2008a). The band combination techniques can effectively distinguish snow cover from thick clouds which are both highly reflective in the VIR and at 1.6–1.7 mm wavelengths (TM band 5). A binary map of glacier and non-glacier areas can be obtained by segmenting the band ratios or NDSI images. Thresholds for the segmentation are dependent on the used band ratios and different regions, and are mainly empirically determined.

It is difficult to distinguish certain land covers, including water bodies (pro-glacial and supra-glacier lakes) and dense vegetation cover, from snow/ice as they show similar high NDSI values. Therefore the automated mapping procedure requires other constrains. For example, threshold on TM band 4 has been widely deployed for effective discrimination of snow/ice from surface water bodies, and threshold for TM band 2 can be used to differentiate certain dense vegetation from snow/ice (Riggs et al., 2006). Post-processing

is commonly necessary to correct misclassifications due to shadow and thin cloud contamination near glacier fringes.

Various topographic information about the glacier can be extracted from the delineated glacier extent and a DEM model. In particular, mean and median elevation are often regarded as approximations of long-term mean ELA. The percentage of accumulation area and ablation area can be derived by the ELA estimates, and the changes can affect internal mass balances of glaciers. There are two nearly-global DEMs available for glacier mapping over the QTP, the SRTM and the ASTER GDEM. SRTM is the first near global elevation dataset which was developed from the C-band (5.6 cm) SAR images acquired from SRTM, flown in February 2000 by NASA. SRTM has been widely utilized in monitoring glacier mass balances (Berthier et al., 2007, Li et al., 2010b). SRTM data cover land surfaces between 60N and 56S at a resolution of 30 m for the USA and 90 m for elsewhere with a 7-m vertical accuracy and 90-m horizontal posting (Rabus et al., 2003). The ASTER GDEM was constructed by applying automated photogrammetric techniques to all suitable scenes available from the ASTER data and covers 99% of the earth surface at a resolution of 30m. ASTER GDEM Version V002 has been issued on October 2011 with vertical accuracy about 20m and 30 m for planimetric precision, and are readily available from the Land Processes Distributed Active Archive Center (LP DAAC, <http://edcdaac.usgs.gov>).

Volume and mass changes can be estimated from the glacier area using the area-volume scaling relationship and with density assumptions. The scaling relationship states that glacier volume (V), area (A) and length (L) are related by logistical relationships such as $A = L^\alpha$ and $V = A^\beta$, where α and β are coefficients that are determined empirically. The formula was developed empirically by (Bahr, 1997b, Pfeffer et al., 1998, Bahr et al., 1998) based on samples of area data and field-based observations, and has been widely applied in glacier mass balance studies. Bahr (1997a) found that β to be 1.36 and for valley glaciers and 1.25 for ice sheets, based on field observations. Liu et al., 2003 suggest a

threshold of 1.35 based on field measurements of glacier thickness in Tianshan in the northern QTP. Volume estimates determined from scaling relationships can be converted to mass balance by assuming a value for the density of glacier lost or gained. A density of ice of 900 kg/m^3 is usually assumed for the conversion of volume changes to mass balance in the ablation zone. In the accumulation area, the density of gained or lost material can range from 900 kg/m^3 (ice) to $550\text{-}600 \text{ kg/m}^3$ (firn). The volume/area scaling approach is fast, convenient, and widely applied for very large samples of glaciers in cases where only 2D information is available.

2.2.2. Challenges and limitations

Automated or semi-automated classification methods, including single band ratios and NDSI have been successfully applied for mapping clean ice over extensive areas. However, some difficulties in automatic mapping of glaciers using band ratios remain due to the presence of seasonal snow and debris-cover on the glacier surface. Generally it is required that the images used for mapping glaciers are acquired at the end of ablation season to ensure seasonal snow cover. Another challenge of glacier mapping lies in the discrimination of debris cover on glaciers which has similar VIS/NIR spectral signature to the surrounding moraines. In such cases, spectral information alone is insufficient for mapping ice covered by debris. Combining topographic information, morphometric information or the difference in the temperature recorded by the thermal bands have been proposed for semi-automated mapping of debris-covered glaciers (e.g. Bolch et al., 2007, Paul et al., 2004, Taschner & Ranzi, 2002). However, most DEM-based approaches require an up to date high-accuracy DEM which is usually available in the rugged QTP and there are difficulties in applying the method in an extensive area due to various assumptions in the glacier characteristics and weather conditions (Racoviteanu et al., 2008a).

Although straightforward and easily applicable, glacier change mapping with optical images has limitations to daylight, cloud-free conditions and has logistical difficulty in automated discrimination of debris-covered glaciers, which constrain its applications over

extensive glacierized areas (Dozier, 1989; Paul et al., 2004; Adina et al., 2008). Moreover, determining a volume or mass change just based on area or length can be inaccurate without information about the change of thickness over the whole glacier, especially in the accumulation zone. Observations from other active microwave systems, such as SAR which are less sensitive to weather conditions, are potential for providing information on glacier distribution (Atwood et al., 2010, Jiang et al., 2011, Frey et al., 2012). The main problem of SAR data lies in geometric and radiometric distortions and speckles (“noise”), which require complicated processing and accurate DEMs which are not always readily available. Other techniques such as space geodetic techniques including InSAR, laser altimetry and satellite gravimetry show promise for increasing our understanding of glacier characteristics and the changes with time, which is introduced in the followed section.

2.3. Geodetic methods

Geodetic approach based on elevation data has been currently recognized as the most successful approach for quantitative observations of regional glacier mass balances, and has been applied to study mass balances over a variety of glaciers, including the Greenland and Antarctic ice sheets (Davis et al., 2005, Helsen et al., 2008), Patagonia icefield (Rivera et al., 2007), Alaskan glaciers (Arendt et al., 2002), Himalaya glaciers (Berthier et al., 2007, Kääb et al., 2012). Geodetic elevation measurements can be classified into three groups: 1) point measurements such as in-situ GPS measurements, space altimetry data (laser altimetry and radar altimetry); 2) raster DEMs derived from photogrammetry or InSAR techniques. GPS measurements are of high level accuracy (decimeter) but have limitations in regional glacier monitoring for poor spatial sampling, difficult accessibility and the logistical difficulty of field work, as a consequence they are often used as adjustments for raster DEMs or ground control points (GCPs).

2.3.1. Satellite altimetry

Data obtained from satellite laser or radar altimetry are average surface elevation within a footprint which is sampled along tracks on the ground. Altimetry measurements can achieve accuracy on the order of decimeter, and they are advantageous for providing multi-data elevation data with relatively short time intervals. Radar altimetry data have a relatively long history and have been successfully used to derive elevation changes of large glacierized areas with low relief (e.g. Davis et al., 2005, Helsen et al., 2008).

The development of laser altimetry in recent years, particularly the availability of elevation measurements from GLAS (Geoscience Laser Altimeter System) onboard ICESat, enables investigation of glacier elevations changes over the rugged mountain areas. GLAS/ICESat employs a near infrared (1064 nm) laser pulses to measure elevations within a diameter of 70m footprint spaced at 172 m along-track. After finishing the calibration campaign (laser period 1AB) in 8-day repeat orbit, the ICESat satellite operated in a 3 by 30-day orbit, with a total number of 18 operational laser periods (Laser 1AB~3K) spanning from February 2003 to November 2009. Compared to radar altimetry, the differences result in significant improvements in spatial resolution and accuracy. With small footprints, the accuracy of ICESat elevation data is generally higher than radar altimetry data and can achieve accuracy on the order of centimeters (Ewert et al., 2012, Shuman et al., 2006). Data from GLAS/ICESat have been widely explored to estimate glacier changes in Antarctica and Greenland, by comparison of ground overlapping footprints, or crossover elevation, or DEMs derived from different GLAS campaigns (Slobbe et al., 2008, Smith et al., 2005, Ewert et al., 2012).

2.3.2. DEMs differencing

The geodetic approach measures elevation changes over time (dh/dt) from various DEMs

constructed over the glacier area to estimate mass balance without direct field measurements. Elevations from older DEMs, often constructed from historical topographic maps, are subtracted from more recent DEMs derived from various contemporary geodetic techniques. Based on pixel by pixel calculation, overall mass change G (kg) over a glacier area can be estimated from observed elevation change Δh over time-span Δt :

$$G = \bar{\rho} \sum A_p * \Delta h \quad (2-1)$$

where A_p denotes the pixel area, $\bar{\rho}$ represents the average density of glacier/firn. By assuming that an n -year balance measurement can be seen as a total of a series of hypothetical annual measurements, the mean annual balance G (kg/a) can be estimated in 2-1. To avoid assumption on glacier density, some studies used the volume change in $\text{km}^3 \text{a}^{-1}$ in water equivalent or the average elevation change expressed as m a^{-1} by dividing total volume loss with the total area.

The geodetic method generally relies on the assumption that 1) no change in the elevation of the bedrock due to tectonic activity or isostatic glacier rebound; 2) the density of the ice mass remain consistent over the time period; and 3) no significant area changes in case of calculating mass change. As the density changes of glaciers are unlikely to exceed a few centimeters per year and the bedrock changes generally have smaller order of magnitude, the assumptions stay reasonable or are not a significant issue if elevation changes observed are in the order of m a^{-1} (Bamber & Rivera, 2007). Generally a sufficiently long time interval (on decadal or longer time scales) is required to allow convincing interpretation of significant inter-annual mass change (Bamber & Rivera, 2007, Racoviteanu et al., 2008a), especially for some marine glaciers with high natural inter-annual variability. Results in form of annual mass balance should be carefully evaluated in terms of uncertainty as the calculation is based on assumption that inter-annual mass dynamics is linear (Berthier et al., 2007).

The availability of new and old DEM is the key for the DEM differencing method. SRTM

DEM is an important dataset in previous studies and it was compared with other DEM from historical maps (e.g. Rignot et al., 2003, Li et al., 2010b) or from satellite stereo images (e.g. Berthier et al., 2007, Gardelle et al., 2012). Research on constructing DEMs with interferometric SAR techniques is demanding, particularly with the availability of data from satellite missions TerraSAR-X (launched in 2007) and TanDEM-X (launched in 2010). It seems likely, therefore, that there will be no shortage of suitable geodetic data in the future, although, in the case of InSAR and photogrammetry, adequate GCPs will still be required.

2.3.3. Gravimetric measurements

The invention and development of satellite technology provide possibility for direct measurement of the Earth's gravity field. With the launch of a series of satellite gravimetry mission, such as CHAMP (Challenging Minisatellite Payload, 2000), GOCE (Gravity Field and Steady-State Ocean Circulation Explorer, 2009) and GRACE (Gravity Recovery and Climate Experiment 2002), techniques of accurate monitoring and quantifying gravity variability on global or regional scales have made great breakthrough. In particular, the release of GRACE gravity model has greatly boost research into global or regional mass variability which is closely associated with hydrological process. A series of significant research findings have been published on glacier mass balance estimation based on GRACE data (Chen et al., 2006, Jacob et al., 2012, Gardner et al., 2013).

The objective of the newest satellite gravity mission GRACE, developed by collaboration of NASA and German Aerospace Center (DLR), is to map the Earth's gravity field at high accuracy with a spatial resolution over 250 km and at ~30-day intervals (Wahr et al., 2004). GRACE deploys K-band ranging (KBR) system to measure the change of the distance between the twin satellites, from which the spatial variability of the gravity field is inverted. GRACE data are classified into four levels: Level-0, level-1A, level-1B and Level-2, each processed on the priori dataset. Level-2 datasets evolved from RL01, RL02, RL03 to RL04 version, each with different geophysical model and improved data quality. Especially RL04

version data offer significantly improved spatial resolution in the order of 300 km. All level-2 products are released to the public through two websites, Physical Oceanic DAAC of NASA's Jet Propulsion Laboratory (JPL-PO DAAC) and Information System and Data Center (ISDC) at German Physical Research Center.

Compared with elevation-based geodetic measurements such as those from photogrammetry or InSAR techniques, GRACE measurements are advantageous for their wide coverage and high temporal resolution, which facilitates monitoring of seasonal or inter-annual mass balances at regional or global scale. GRACE-based measurements of glacier mass balance can be an independent evidence of glacier changes apart from topographic and cartographic data.

The errors of GRACE-based glacier mass change measurements mainly result from errors connected with decorrelation smoothing, spatial average and leakage reduction. One weakness of the GRACE measurements is that they are incapable of discriminating between mass changes from water, snow, or ice (Wahr et al., 1998). For intensively glacierized surfaces, the assumption that glacier mass changes are the dominating signals that cause annual gravity changes of the regions is reasonable; however, whether the mass change of glaciers will definitely lead to variation of the regional gravity field that are detectable with GRACE need detailed investigation. This is not only related to the magnitude of the mass change signal but also linked with the pattern of regional hydrological circle (out flow or endorheic basin). The recent debate on the contrasting results from GRACE observations (4 ± 20 Gt/year in Jacob et al., 2012) and non-GRACE measurements (-55 Gt/year in Gardner et al., 2013) is probably caused by lake expansion in endorheic basins where glacier melt water drained into closed lakes rather than flowing to sea (Zhang et al., 2013, Song et al., 2014).

Other limitations of GRACE include that its low spatial resolution (improved to the order of 300 km for Level-2 RL04 products) which makes it unsuitable for individual glacier monitoring, and the relatively short time spans (about 10 year). The challenging of utilizing

GRACE data for glacier mass determination includes effective resolving of signal leakage problem, accurate correction of hydrological and PGR signal with independent models and quantified uncertainty estimates of the final results. Fortunately, GRACE data themselves can also serve as useful sources for promoting understanding of the complex hydrological and PGR processes which in turn can be used for correction. With the development of new post-processing techniques and improved models, GRACE gravity observations can provide unprecedented comprehensive and reliable measurements of global and regional glacier mass balances.

2.4. Climatic data for studying glacier-climate relationship

The main difficulty of assessing climate change lies in deriving long-term reliable climatic records. This section introduces available climatic datasets from weather stations, reanalysis, remote sensing observations and other products. Characteristics of different sources of data are discussed in terms of resolution, spatial and temporal coverage, and reliability.

Local temperature and precipitation data from weather stations are generally considered as most direct and reliable. In China, there are about 136 weather stations located in and around QTP (Fig. 2.1). Most of the stations were established during the 1950s. Station-based data are free of noise and highly consistent. However, a major problem of this kind of data is that the distribution of the stations is biased to the eastern, lower elevation and populated areas. In particular, weather stations over the QTP are concentrated in the eastern part, while there are few stations in the northwestern and interior QTP, such as over the Chiangtang Plateau and the Pamir, due to inaccessibility and logistical difficulty in field observations. Based on station observations, assessments of climate change around glaciers should take into account the altitude-dependence of climate, as glaciers are situated at altitudes that are far higher than locations of most weather stations.

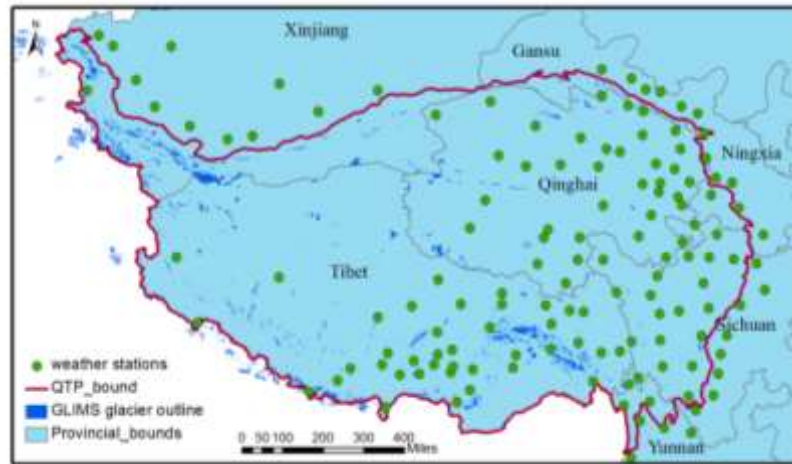


Fig. 2.1 Distribution of weather stations in and around QTP

Compared to station-based data, remote sensing data are spatially continuous, thus are favorable for remote regions. One widely used dataset is MODIS LST (Land Surface temperature) data at 1km resolution spanning from 2002 to present. Similar to other remote sensing LST products, the major limitation of MODIS LST data lies in uncertainties associated with noises and validation difficulties. Reanalysis is a systematic approach which incorporates millions of observations into a stable data assimilation system and model(s) to produce data sets for climate monitoring and research. The output of such process is referred as reanalysis data. Two temperature datasets, ERA-Interim reanalysis and NCEP reanalysis have been widely used. Previous studies suggest that ERA and NCEP reanalysis temperature data can capture the extreme events and inter-annual variability very well (Frauenfeld et al., 2005). ERA-Interim reanalysis data was produced by the ECMWF and covers the period Jan. 1979 to present with a spatial resolution of $2.5^{\circ} \times 2.5^{\circ}$ grid (Simmons et al., 2007). The NCEP/NCAR 2m air temperature is a standard modeled field, which represents a linear interpolation between the surface skin temperature and free-air temperature at the lowest model sigma level (Kalnay et al., 1996). This dataset covers Jan 1948 to present with the spatial resolution of $2.5^{\circ} \times 2.5^{\circ}$ (Kalnay et al., 1996).

There are various reanalysis precipitation dataset provided by different institutions. The GPCP (Global Precipitation Climatology Project) precipitation dataset provides monthly

rainfall on a 2.5-degree global grid from 1979 to the present. This dataset is a schematic combination of data from rain gauge stations, satellites, and sounding observations. The GPCP data have proven to be capable of revealing precipitation changes on seasonal to inter-annual time scales, and serves as validation of results generated from re-analysis systems, such as those from NCEP/NCAR and ECMWF. GPCP offers the potential of studying long-term precipitation changes on large spatial scale (Yao et al., 2012).

The changes of regional and large-scale atmospheric circulations can be depicted by various index computed from reanalysis data, mainly the SLP. Listed below are some key indices that are commonly used to represent the strengths of atmospheric circulations impacting climates over different parts of QTP.

NAO: North Arctic Oscillation (NAO) is a climatic phenomenon in the North Atlantic Ocean, represented by fluctuations in the difference of atmospheric pressure at sea level between the Icelandic low and the Azores high. NAO is closely connected with the strength and direction of westerly winds which affect climate in north and mid-latitude Asia. The principal component (PC)-based NAO is the time series of the leading Empirical Orthogonal Function (EOF) of SLP anomalies over the Atlantic sector (20°-80°N, 90°W-40°E).

NAM: the North Annular Mode (NAM) index, indicating anomalies in NH SLP, is the first EOF of winter SLP data (DJFM: Dec-Mar) over the North Hemisphere (NH: 20°-90°N).

SOI: The El Niño and La Niña episodes can be represented by the Southern Oscillation Index (SOI) which is calculated as the normalized anomaly of mean SLP difference between Tahiti and Darwin. The negative (positive) SOI values coincide with abnormally warm (cold) ocean waters across the eastern tropical Pacific in typical El Niño (La Niña) episodes.

EASMI: the East Asian Summer Monsoon Index (EASMI) is defined as an area-averaged seasonally (JJA: Jun. to Aug.) dynamical normalized seasonality at 850 hPa within the domain (10°N-40°N, 110°E-140°E) (Li & Zeng, 2002).

IMI: the normalized anomalies of SLP difference between the Indian sea zone (40E-80E, 5N-15N) and central Asia (70E-90E, 20N-30N) (Wang et al., 2001).

NPI: The anomalies of SLP over north pacific. The area-weighted SLP over the region 30N-65N, 160E-140W (Trenberth & Hurrell, 1994).

The NAO, NAM, NPI and SOI index were all obtained from Climate Analysis Section (NCAR). The annual, summer (JJA: Jun.-Aug.) and winter (DJFM: Dec.-Mar.) NAO time series can be used to evaluate the influence on time scale of yearly, warm season and cold season. SOI was also aggregated to two seasons accordingly. NAM and NPI are both pronounced in winter seasons (DJFM and NDJFM respectively), therefore only winter average was used. The summer monsoon index including IMI and EASMI are pronounced in summer seasons, thus JJA means were respectively obtained from Asia-Pacific Data-Research Center (<http://iprc.soest.hawaii.edu/users/ykaji/monsoo/seasonal-monidx.htm>) and Li's page (<http://ljp.lasg.ac.cn/dct/page/65577>).

Chapter 3

Compilation of a new glacier inventory for the Southeastern QTP from Landsat and PALSAR data

3.1. Introduction

A large number of studies have been devoted to investigation of mountain glacier changes and their impacts on hydrological cycles and water resource as a result of anthropogenic warming (e.g., Shi et al., 2010, Kaser et al., 2006, Gardner et al., 2013, Huss, 2011, Grinsted, 2013, Song et al., 2015, Andreassen et al., 2008, Bolch et al., 2010b). These studies critically depend on a fundamental baseline dataset in a complete and reliable glacier inventory (e.g. Cogley, 2010, Ohmura, 2010). In general, a glacier inventory provides essential information about the distribution of glaciers, and a variety of parameters of glaciers such as the spatial extents and the topographical features. However, mapping glaciers over areas with rugged terrain and frequent clouds, and/or with optically thick debris cover, is still a challenging issue in remote sensing (Raup et al. 2007, Racoviteanu et al., 2010), which results in the unavailability of reliable glacier inventories for some regions, particularly over the mountainous central Asian region including the QTP.

At present, digital glacier inventory for the SE QTP is provided in four datasets, CGI1 (the first version of China Glacier Inventory), GLIMS (Global Land Ice Measurements from Space), RGI (Randolph Glacier Inventory) and CGI2 (the second version of glacier inventory). The CGI1 was completed in 2002 based on topographical maps and aerial photographs acquired from the 1950s to the 1980s (Shi et al., 2010), and was then incorporated into the world glacier inventory including GLIMS and RGI. The glacier outlines in the first three datasets are similar for most of regions in the QTP, and show serious quality issues due to problems of source data in the CGI1 (Pfeffer et al., 2014). Although strong efforts have been made to produce reliable glacier outlines for the QTP by using recent satellite data, the latest glacier outlines provided in CGI2 show little updates

over the SE QTP, where no good quality Landsat images without snow and cloud cover could be acquired (Guo et al., 2015). The potential errors in the glacier inventory will result in great uncertainties about regional glacier changes, as well as generalization of local information to the regional. Uncertainties and the limited knowledge about glaciers in the SE QTP are obvious from the lack of documentations and discussions on estimates of the glacier mass loss, despite that strong thinning and mass loss of several glaciers were reported based on field observations (Shen, 2004; Yang et al., 2008; Yao et al., 2012). The absence of reliable glacier inventory for the region hinders detailed studies on glacier characteristics, estimating or modeling of regional glacier changes and assessment of the environmental impact.

The SE QTP presents extremely challenging condition for mountain glacier mapping due to prevalent orographic clouds which obscure observations from optical sensors, seasonal snow cover and debris cover. The cloud coverage is particularly serious in summer seasons due to influence of Asian summer monsoons, resulting in absence of cloud-free scenes. Another challenge in glacier mapping is identification of debris-covered glaciers which show similar spectral characteristics with the surrounding non-glacier areas. In previous studies, the debris-covered glaciers were mainly delineated by manual delineation which is time-consuming and highly dependent on the researcher's skill and expertise. In addition, the spectral similarity of various surrounding objects renders the decision-making difficult. Semi-automated methods for retrieving debris-covered ice have been proposed in previous studies by combining multi-spectral optical data and DEM (Paul et al., 2004), and based on thermal data (Shukla et al., 2010, Karimi et al., 2012); however these methods are hard to apply to an extensive region due to the dependences on cloud-free images, up-to-date high quality DEM or local environmental characteristics such as snow cover, weather conditions, and the thickness of debris (Racoviteanu et al., 2008, Veettil, 2012).

This section presents a semi-automated approach for generating a digital glacier inventory based on latest multi-source and multi-temporal satellite data. Both multi-spectral Landsat

imagery and non-polarimetric SAR data are used in a systemic scheme for glacier mapping in the SE QTP where there are frequent orographic clouds, seasonal snow and highly debris-covered glacier tongues. Results from multi-temporal Landsat scenes are employed to compensate the effect of clouds. A semi-automated framework is developed to retrieve debris-covered glacier tongues based on coherence maps derived from the ALOS PALSAR (Phased Array type L-band Synthetic Aperture Radar) sensor, and information from Landsat imagery and DEMs.

3.2. Study region and datasets

3.2.1. Extent of mapped glaciers

The study region in the SE QTP covers an area more than 100,000 km². It constitutes a series of grand mountain ranges including the central and eastern Nyainqentanglha ranges, eastern Himalayas and western Hengduan Mountains (Fig. 3.1). The northern limit is defined by the Salween and the southern limit by the Yarlung Tsangpo. The majority of the region belongs to the Yarlung Tsangpo basin and some glacierized region in the east drains into the Salween. The SE QTP area is under the influence of both continental climate of central Asia and the Asian summer monsoon systems, and the latter bring plenty of precipitation in summer seasons (May to October). Glaciers in this region are typical temperate glaciers (Su & Shi, 2002, Yang et al., 2010).

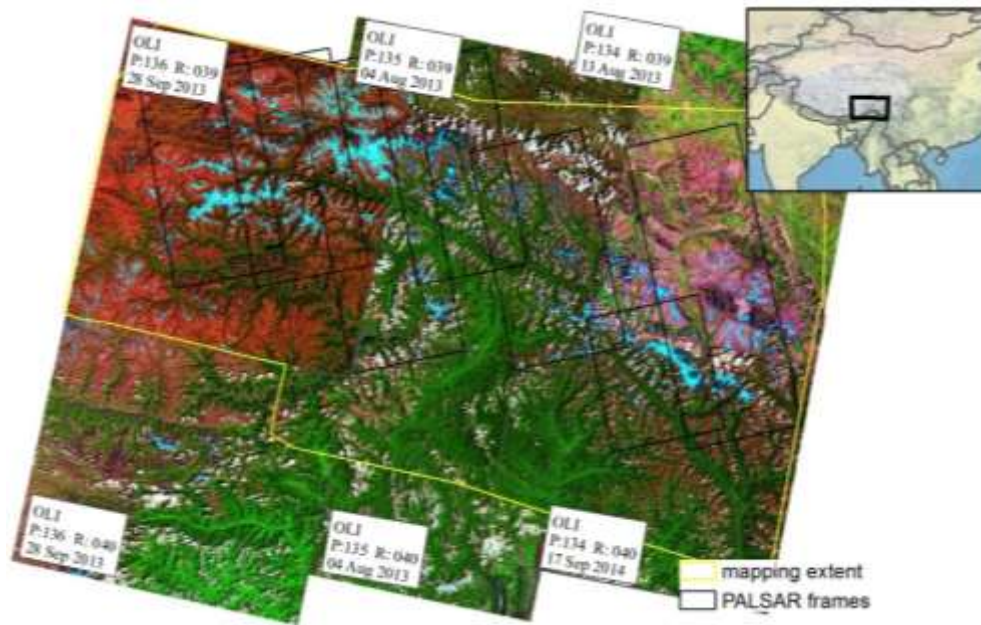


Fig. 3.1 Overview of the study area and satellite data including Landsat 8/OLI images in false color composite (RGB 754 for Landsat 8) and the frame of PALSAR images.

3.2.2. Landsat imagery

Images from the Landsat sensors including Landsat 8/OLI, Landsat 7/ETM+ and Landsat 5 TM, acquired in the period of 2011-2013 are used for glacier mapping (Table 3.1). All available scenes are inspected to select images that are cloud-free over the glaciers and with minimal seasonal snow cover. However, it is almost impossible to get one image that is totally free from clouds in the summer season, due to frequent cloud activities and prevalent orographic clouds in the monsoon season. Meanwhile, there is significant contrast in seasonal snow/ice coverage in warm and cold seasons. As a compromise between minimal seasonal snow cover and cloud cover, all available scenes acquired in August/September 2011-2013 with low cloud coverage (at most 40%) are employed to mapping glaciers in a schematic overlay frame (see the method section).

Table 3.1 List of satellite data used for mapping the SE QTP glaciers

Purpose	Platform and sensor	ID(p=path, R=row, T=track, F=frame, B=baseline)	Date(mm/dd/yyyy)	Bands used
Glacier mapping	Landsat8/OLI	P:134, R:39	08/13/2013	Band 3,4,5,6, 7
	Landsat8/OLI	P:134, R:39	09/14/2013	Band 3,4,5,6, 7
	Landsat8/OLI	P:135, R:39	08/04/2013	Band 3,4,5,6, 7
	Landsat7/ETM+	P:135, R:39	08/12/2013	Band 2,3,4,5, 7
	Landsat7/ETM+	P:135, R:39	08/23/2011	Band 2,3,4,5, 7
	Landsat5/TM	P:135, R:39	08/31/2011	Band 2,3,4,5, 7
	Landsat7/ETM+	P:135, R:39	09/08/2011	Band 2,3,4,5, 7
	Landsat8/OLI	P:136, R:39	08/11/2013	Band 3,4,5,6, 7
	Landsat8/OLI	P:136, R:39	09/28/2013	Band 3,4,5,6, 7
	Landsat8/OLI	P:134, R:40	09/17/2014	Band 3,4,5,6, 7
	Landsat8/OLI	P:134, R:40	08/13/2013	Band 3,4,5,6, 7
	Landsat8/OLI	P:134, R:40	09/14/2013	Band 3,4,5,6, 7
	Landsat8/OLI	P:135, R:40	08/04/2013	Band 3,4,5,6, 7
	Landsat8/OLI	P:136, R:40	09/28/2013	Band 3,4,5,6, 7
	Coherence images	ALOS PALSAR	T:488, F:570-590, B:83m	6/16/2009, 9/16/2009
ALOS PALSAR		T:489, F:570, B:183m	8/21/2010, 10/6/2010	
ALOS PALSAR		T:490, F:580-590, B:17m	7/23/2010, 9/7/2010	
ALOS PALSAR		T:491, F:590-600, B:323m	8/9/2010, 9/24/2010	
ALOS PALSAR		T:492, F:580-600, B:408m	7/11/2010, 8/26/2010	
ALOS PALSAR		T:493, F:590-600, B: 391m	7/28/2010, 10/28/2010	
ALOS PALSAR		T:494, F:590-600, B: 234m	6/26/2009, 9/26/2009	

This study uses standard L1T products performed with systematic radiometric and geometric correction and in Universal Transverse Mercator (UTM) projection. The study area is covered by five scenes with different path/row (Table 3.1 and Fig. 3.1). For practical purpose, this study adopted UTM zone 46N as the projection for all mosaicked images and inventory.

3.2.3. SAR image pairs

For mapping debris-covered glaciers, coherence images from seven ALOS PALSAR image pairs are used. The ALOS PALSAR sequential scenes were acquired from the ascending orbit in Fine-Beam Dual mode (FBD-HH/HV) with perpendicular baselines less than 410 m and a time interval of 46 or 92 days during the snow-free period of 2009 or 2010 (Table 3.1, Fig. 3.1). The PALSAR FBD data have an off-nadir angle of 34.3°, and the resolution

is about 4.5 m in the azimuth direction and 9.6 m in the range resolution. The L-band PALSAR data is preferred to the C- or X-band systems because the low-frequency system is less sensitive to decorrelation factors; thus severe temporal decorrelations associated with changes in surface properties can be enhanced. In order to mitigate the effect of spatial deceleration, SAR image pairs with small baseline are preferred. The derived ALOS PALSAR data cover the most glacierized region (over 95%).

3.2.4. DEM data

For the study region, there are no available local or national DEM of high quality. Two elevation datasets are available with near-global coverage: the DEM from the SRTM and the ASTER GDEM, which are both accurate enough for compiling topographic glacier inventory data (Frey & Paul, 2012). However, a subtraction of the ASTER GDEM from the SRTM DEM (version 3 SRTM provided by CIGAR) reveals in some regions differences of several hundred meters up to 1 km. Visual check in hill shade view confirms the systematic shifts in some regions of the interpolated SRTM elevations, indicating that the large bias is probably caused by erroneous interpolations in the SRTM data voids. This study replaces the erroneously interpolated values of SRTM3v4 with the corresponding ASTER GDEM (smoothed to reduce artificial bumps and holes and resampled to 90 m resolution before merging). The new SRTM DEM is void-free and smooth in hill shade view, and used in compilation of the glacier inventory and processing of the ALOS PALSAR coherence images. The percentage of replaced data over the region is less than 1%, mainly out of the glacierized region.

3.3. Methodology

Generation of the glacier inventory in SE QTP consists of three major parts including mapping clean ice with Landsat imagery, mapping debris-covered ice by combining Landsat, coherence images and DEM, and generation of ice divides and glacier parameters.

3.3.1. Mapping clean-ice

This study presents a semi-automatic procedure for mosaic of partly cloud-covered glacier masks to generate a final cloud-free mask. For clean ice mapping, key steps involve generation of a series of mask from each scene: glacier mask, cloud mask, open water surface mask and vegetation mask.

1. Preprocessing of Landsat scenes

The production of the mask relies on band reflectance of TM/ETM+/OLI scenes. Calibration of Landsat scenes from raw digital numbers (DN) values to Top-of-Atmosphere (TOA) reflectance is processed in ENVI/IDL platform. For Landsat8/OLI images, such calibration is done by referring to gain and offset parameters readily provided in metadata files. For TM/ETM+ images, the calibration needs extra references to parameters such as mean exoatmospheric solar irradiance (ESUN) and earth-sun distances which are summarized by Chander et al. (2009). We use TOA planetary reflectance instead of DN, as it is preferable to work with data expressed in physical units and these calibrations may help standardize scenes from different dates and/or sensors (Burns and Nolin, 2014). The data gaps in the Landsat 7/ETM+ scenes due to failure of scan-line corrector are masked out with no-data filling value.

2. Generation of glacier masks

Segmentation of NDSI images is used to generate single clean ice mask from individual Landsat scenes. NDSI is computed as the normalized difference of the reflectance of green band and short-wave infrared band (SWIR) (Landsat 8/OLI: $(B3-B6)/(B3+B6)$; Landsat 7/ETM: $(B2-B5)/(B2+B5)$). In comparison to single band ratios such as $B3/B5$, NDSI is effective in removing some of the illumination effects present on glaciers and yielding satisfactory results in shaded ice (Racoviteanu et al., 2008a). Pixels with $NDSI \geq 0.4$ are classified as potential clean-ice glaciers (value 1), and pixels with $NDSI < 0.4$ are set to 255 in the mask image, and no-data filling pixels are set to 0. The original NDSI image is shown for a sub-region in the central study area (Fig. 3.2a(1)). The thresholds of 0.4 have

been developed based on experiments of glaciers sampled all over the world, and been widely used in previous studies (Hall et al., 1995a). Mapping results are not sensitive to the changes of thresholds between 0.39 and 0.41.

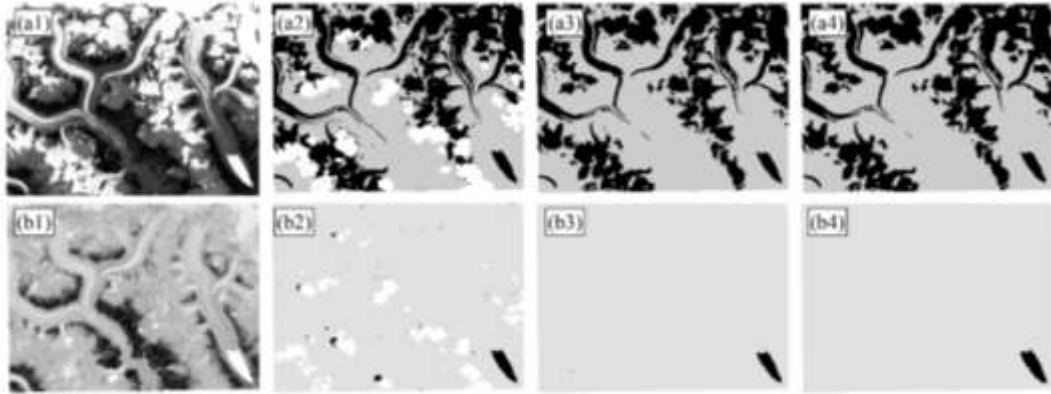


Fig. 3.2 Selected key processing steps in clean-ice mapping: clean-ice mask (a) and water mask (b). Column 1 is ratio image (NDSI/NDWI) of a single scene; column 2 is the result of thresholding (binary image in black and grey) and then cloud masking (cloud in white); column 3 is the map of overlay and mosaic of all mask; column 4 is the final result after post processing.

3. Generation of cloud masks

As most of the used Landsat scenes are partly cloud-covered, a prerequisite step before mosaicking clean-ice mask scenes is to identify which part of the images are contaminated by clouds. Such cloud-cover identification is implemented with the Fmask tool which is available at <https://code.google.com/p/fmask/>. The latest Fmask tool v3.2 is able to process Landsat 4, 5, 7, and 8 images with an easy execution of fmask.exe file in the command window (Zhu et al., 2015). This tool can generate cloud mask (with a value of 4) with high accuracy by applying a proper probability threshold (ranging from 0 to 100) in the input. This study tested a series of thresholds on different scenes and found that a threshold of 95-100 produced most accurate result for most scenes. The percentage of cloud area identified generally increases with the applied probability threshold, and stabilized after the threshold of 95. However, for several scenes which have low-terrain thick clouds, such as the LE7/ETM+ image acquired on 8/23/2013, a high probability threshold failed to identify the thick clouds densely distributed along the mountainsides. In such cases, a threshold of 50-60 can produce satisfactory results. To maintain the highest percentage of clear pixels while

identifying cloud coverage at most, it is recommended to verify the accuracy of individual cloud mask by superimposing it on the false color composite image.

4. Overlay and mosaic of glacier masks

The cloud masks generated by Fmask are used to mask those cloud-covered pixels to filling value 0 (no information), and then the masked image is smoothed with a 3×3 kernel-size median filter to remove isolated pixels and fill small gaps. The resulted map is shown in of Fig. 3.2a(2). All masks are finally mosaicked and overlaid in with the ‘Maximum’ mosaic method. With this overlay, the non-glacier values (255) is priori to glacier value 1, and the lowest priority is value 0 denoting filling values and the cloud-covered parts. The mosaic can retrieve minimum clean ice extent from multiple scenes and the cloud-covered parts can be automatically removed and substituted by the clear parts in other scenes. The result is illustrated in Fig. 3.2 a(3).

The mosaicked mask is smoothed with morphological operators (open and close operation with disk structural element of 1-pixel radius). Smoothing is necessary to fill small holes and remove small patches that originate from seasonal snow, mosaicking, cloud-detection and water-mask uncertainty. The minimum size of glaciers to be included in the glacier inventory was set to 0.02 km², and therefore small patches < 20 pixels are removed. The choice of the minimum glacier size depends on seasonal snow coverage and the resolution of Landsat images, and consistence with other Landsat-based glacier inventory (Bajracharya & Shrestha, 2011, Frey et al., 2012). Part of the smoothed clean-ice mask is shown in Fig. 3.2 a(4).

5. Generation, overlay and mosaic of water masks

Note that the smoothed clean-ice mask contain misclassifications including lakes, pre-glacial lakes and wide rivers, as these water bodies usually show high NDSI values. A common solution in previous studies is to apply a threshold on the NIR band reflectance (TM/ETM band 4, OLI band 5) to eliminate water surfaces which are characterized by low reflection at the NIR band. This method, however, will eliminate the shadowed or

illuminated ice which has been successfully identified by the NDSI approach at the same time, and can affect delineation of the glacier tongues due to strong melting.

This study produces a water mask to remove water bodies, in a way similar to the generation of glacier mask. The method mainly includes four steps: 1) generation of ratio index image, 2) segmenting ratio image and masking cloud, 3) mosaic and overlay of all scenes, 4) smoothing and post-process. The Normalized Difference Water Index (NDWI) image is used as a main base for identifying water bodies. NDWI is computed as the normalized difference of the reflectance of green band and near infrared (NIR) band (TM/ETM+: $(B2-B4)/(B2+B4)$; OLI: $(B3-B5)/(B3+B5)$) (McFeeters, 1996). In the NDWI image, the unfrozen open water surfaces generally show high NDWI values, in contrast of the slightly positive or negative NDWI shown by the non-water areas. A threshold of 0.15 is applied to segment NDWI image into open water surface (value 1), non-water areas (255) and filling values (0). A major problem with the water masking is that the shadowed areas will be included. The misclassifications are effectively reduced by thresholding on the mean slope of each water patch. If the polygon represents real water surfaces, the mean slope should be very small. According to the bimodal distribution of the slope of water polygons (Fig. 3.3), a threshold of 15 degree is selected to remove polygons with large mean slope. This method is more effective than a pixel-by-pixel filtering with slope image, as the DEM is not up-to-date and some lakes may cover large slope areas due to expansion. During post processing, the polygons are dilated with about 2 pixels, and then used to erase water parts from the clean ice masks. Key steps in processing water mask is presented in Fig.3.2b.

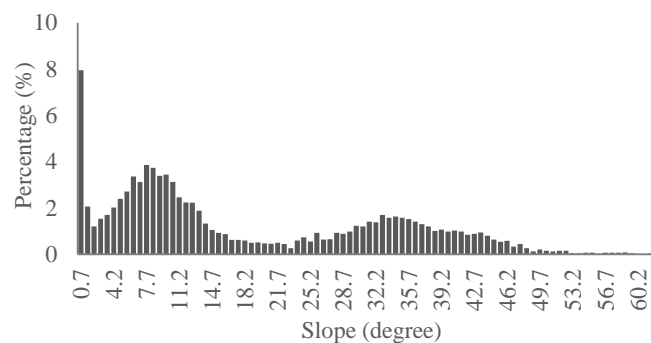


Fig. 3.3 Distribution of mean slope of all water polygons in the study area

3.3.2. Mapping debris-covered ice

As an alternative to optical imagery, SAR data from active radar sensors are independent of weather and solar illuminations. One important estimate from SAR data is the coherence map which shows the correlation of images pairs used for interferometry. Since coherence is defined by phases and image intensities related to radar backscattering, the magnitude of coherence depends on many factors including sensor parameters (wavelength, polarization, system noise, slant range resolution), parameters related to the observation geometry (baseline, local incidence angle), and the surface properties (Frey et al., 2012, Jiang et al., 2015). The influences of sensor- and geometry-dependent factors can be mitigated by appropriate interferometric processing. Volume decorrelation caused by penetration of the radar and temporal decorrelation caused by changes of target surface (i.e. motion and change of the scatterers) between image acquisitions are important to characterize properties of the observed surfaces. In particular, temporal decorrelation over glaciers can be severe in summer seasons, due to melting and freezing of ice and significant glacier flow which cause surface scattering and geometry changes. Thus the low coherence can be used as a proxy for identifying glaciers.

One main concern of SAR estimates, including the coherence maps, is geometric distortions including layover and shadow which lead to data gaps over certain areas. Fortunately, the debris-covered glacier tongues which are characterized by smooth terrain with small slopes, are generally free from the layover and shadow problems. Therefore it is feasible to retrieve complete debris-covered tongues from the coherence map. As there are other contributors to the low coherence values, such as melt of seasonal snow and growth of vegetation, this study developed a multi-source method for mapping debris-covered tongues, by using coherence information as a base and other additional information including surface slope and land cover classifications (vegetation, glacier and water bodies). Specifically, the debris-covered parts are determined by six rules: 1) coherence < 0.15; 2) slope is in the range of 0-24°; 3) not clean ice (value = 255 in the clean ice mask); 4) not vegetation cover (value =1 in the vegetation mask, introduced

below); 5) not water bodies (value = 0 in the water mask); and 6) connected with clean ice. The processing workflow is drawn schematically in

Fig. 3.4, and introduced in details in the following sections.

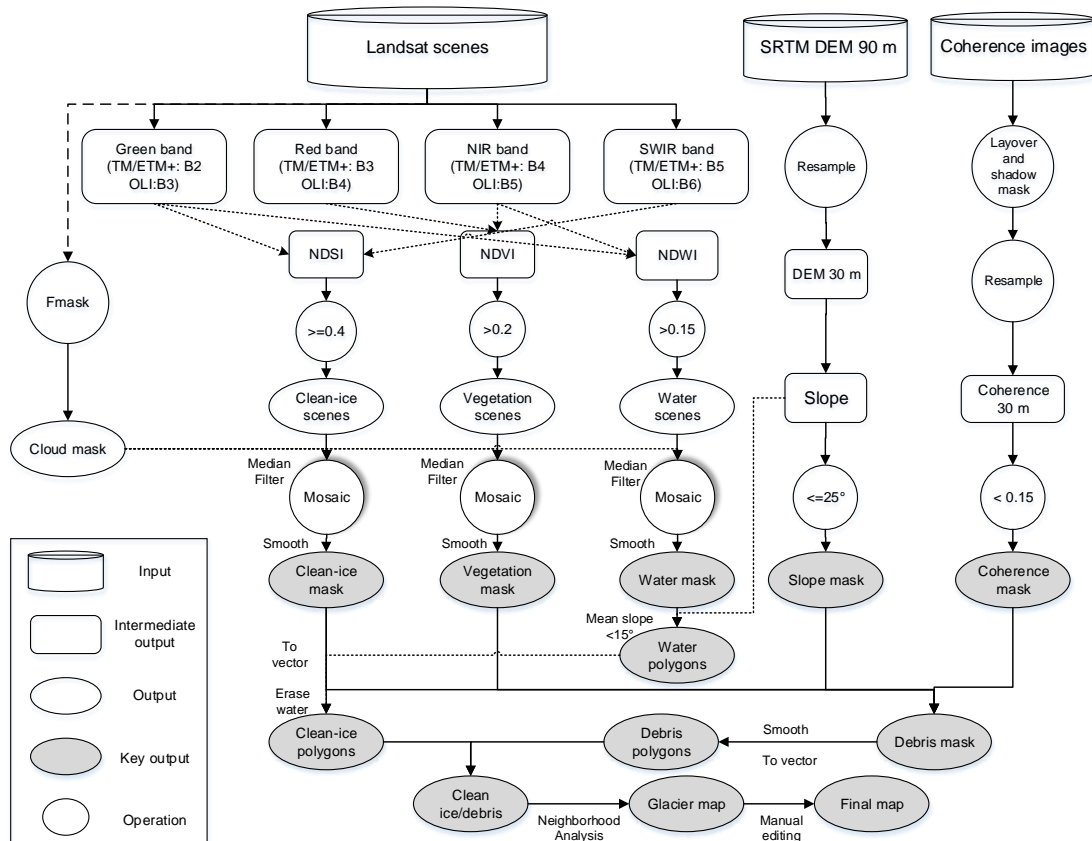


Fig. 3.4 Schematic workflow for mapping clean ice and debris-covered parts in the SE QTP.

1. Generation and segmentation of coherence images

This study uses the Gamma Remote Sensing interferometric tools (GAMMA) to derive single look complex (SLC) images pairs and interferometric coherence from the Level 1.0 ALOS PALSAR data. Firstly, five pairs of single look complex (SLC) images are derived after preprocessing of raw data, concatenating scenes along the track, range and azimuth compression, and absolute radiometric calibration. The SLC image pairs are then co-registered with references to topographic information from the corrected SRTM3v4 DEM. Due to rugged terrain, simulated topographic phase are computed from the SRTM DEM

and subtracted from the interferometric phase. In process of the interferograms, common band filtering and a multi-looking of 6 by 14 cells in the range and azimuth direction respectively are performed to reduce phase noises and reach approximately square pixels on the ground. An adaptive phase filter based on phase gradient (Goldstein & Werner, 1998) is applied to maximize the difference between the decorrelated and coherent areas. For coherence estimation an adaptive window size varied between 3 x 3 and 9 x 9 pixels were used for the interferogram. In addition, a weighting function, decreasing linearly with increasing distance, was applied (Wegmüller & Werner, 1997). After terrain correction and geocode, the coherence images are generated in UTM projection at a spatial resolution about 45 m.

Glaciers and water bodies show very low coherence values (dark) in the resulting coherence images (Fig. 3.5a(1)). Areas with interpolated coherence values due to layover and shadow are identified with reference to SAR reference geometry and topographic information (Fig. 3.5a(2)). To extract the low-coherence areas, the coherence image is segmented by applying a threshold which is determined empirically based on testing the distribution of coherence values over several large debris-covered glaciers. The control glaciers are manually delineated by referring to the false composite of Landsat images. The average value of the tested glacier parts is 0.15 with standard deviation of 0.04. The low-coherence areas (coherence < 0.15) are extracted (Fig. 3.5a(3)) and then smoothed with morphological operators to remove small holes and noises in the mask.

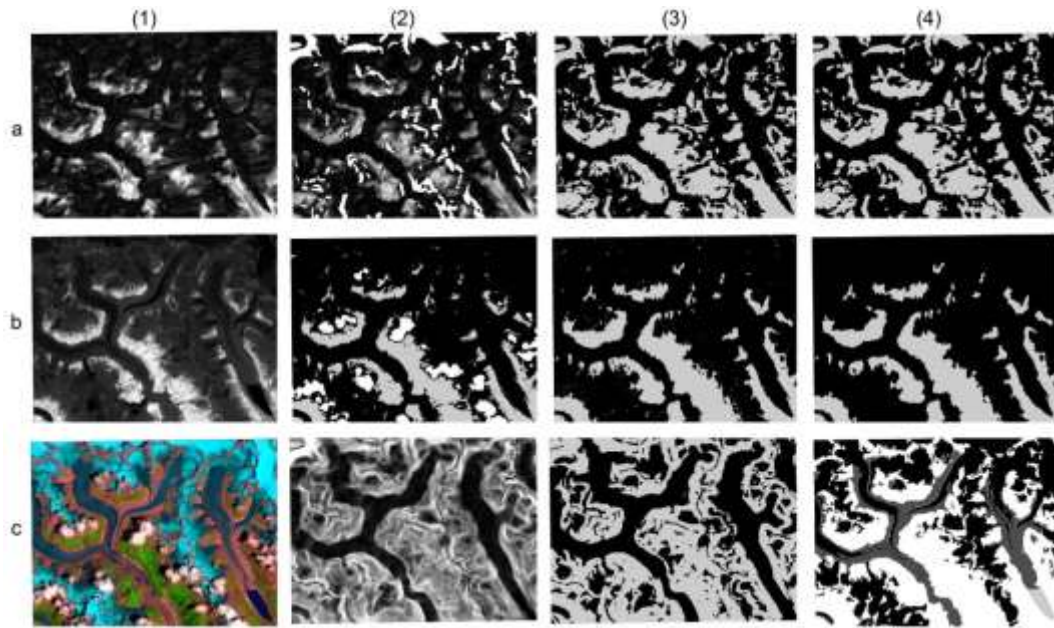


Fig. 3.5 Illustration of key processing steps in debris mapping.

Row a: a(1) coherence image; a(2) coherence with data gaps masked; a(3) resulting binary map of low-coherence areas(black) and others (data gaps and high-coherence areas in grey) after thresholding; a(4) final binary coherence mask after smoothing.

Row b: b(1) NDVI image of a single scene; b(2) resulting map of thresholding and cloud masking (cloud in white, vegetation in grey and non-vegetation in black); b(3) mosaic of all vegetation masks; b(4) final binary vegetation mask after smoothing.

Row c: c(1) false-color composite of Landsat 8 image; c(2) slope map of SRTM; c(3) resulting map after segmenting slope with a threshold of 25;c(4) overlay of the binary coherence (a4), vegetation (b4), slope map(c3), clean-ice(Fig. 3.2 a(4)), water (Fig. 3.2 b(4)), showing clean-ice in black, debris-covered ice in dark grey, water in light grey.

2. Generation of vegetation masks and slope masks

The generation of vegetation mask is similar to that of water mask and clean ice mask. The Normalized Difference Vegetation Index (NDVI), is used to segment the scenes into vegetation and non-vegetation areas. NDVI is computed as the normalized difference of the reflectance of near infrared (NIR) band and red band (TM/ETM: $(B4-B3)/(B4+B3)$; OLI: $(B5-B4)/(B5+B4)$). Similar to NDSI and NDWI, NDVI can highlight the contrast between certain types of land cover, specifically, vegetation areas (high NDSI) and other land cover areas (low or negative NDSI values). The Landsat images were acquired in summer season, thus they are suitable to define the maximum coverage of vegetation. This study uses a threshold of 0.2 to segment the vegetation-covered areas ($NDVI > 0.2$: value

255) and non-vegetation areas ($\text{NDSI} < 0.2$: value 1), according to the bimodal distribution of NDVI values in the scene (Fig. 3.6). All vegetation masks are cloud masked, smoothed and then mosaicked to a single mask with the ‘maximum’ rule setting, which means a maximum vegetation cover retrieved by the mosaicking. Selected steps for deriving the vegetation mask is shown in Fig. 3.5 b(1-4).

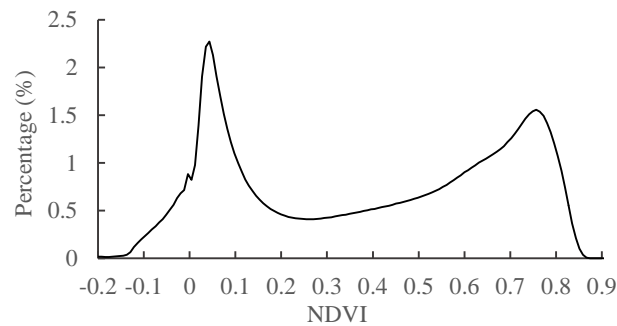


Fig. 3.6 Distribution of NDVI in one Landsat scene

Thresholding on slope image have been proven to be effective in extracting areas with glacier tongue like topography (Paul et al., 2004, Veettil, 2012). Paul et al (2004) demonstrated the slope of glacier tongues in a mountain glacier in the Swiss Alps does not exceed 24° . Similar to previous studies, this study applied a threshold of 25° to segment the slope map. The slope mask effectively limits potential debris-covered areas over the relatively flat terrain.

3. *Overlay of all masks and post processing*

By overlaying the coherence mask, clean ice mask, vegetation mask, water mask and slope mask, the general distribution of the debris-covered ice can be derived (Fig. 3.5c(4)). Smoothing is performed for the binary mask with the morphological operators. The mask may contain sliver polygons or small isolated patches that are far from the clean-ice covered region, which is a result of various uncertainties in the datasets. The artifacts are removed with the neighborhood-analysis. The smoothed binary mask is transformed to vector format with the raster to polygon conversion, and then by using the ‘select by location’ tool in the ARCGIS software only polygons connected with the clean-ice polygons are retrieved.

The final post processing involves editing of the clean-ice and debris-covered polygons to ensure seamless joint. Then the debris-covered ice and clean ice polygons are merged to form a complete glacier outline. The separate mapping of clean ice and debris-covered ice allows a straightforward distinction of the two type of glaciers and calculation of the percentage of debris cover for each glacier.

3.3.3. Delineation of ice divides

The last but most time-consuming step of mapping glacier inventory is to separate individual glaciers along the hydrological divides. For compiling of glacier drainage basins, this study follows the automated approach described by Bolch et al. (2010b) and derived hydrological basins by watershed analysis with the SRTM DEM that has been clipped to a buffer of 1km around the glacier outlines. The automatically derived drainage divides contain errors due to inaccurate estimates in the DEM, particularly in the accumulation area and along the glacier margins, e.g. inaccurate delineation of ridges in the mountainous area and many silver polygons along the glacier margins (Fig. 3.7). This study hence inspect the errors and manually improved the divides with the help of DEM in hillshade view and Landsat scenes. The Landsat scenes can help in delineating ridges in some regions due to illumination differences, and in interpretation of steep, snow/ice-free rocks which acts as natural separation of glaciers. Small polygons with area less than 0.02 km² are omitted in the final glacier inventory. The omitted area is less than 0.04%. With reference to the DEM, glacier-specific parameters including topographic information (minimum, maximum, mean and median elevation, mean slope and mean aspect in degree and mean aspect sector) can be calculated for each glacier. In addition, an internal ID and the percentage of debris cover were also assigned to each glacier.

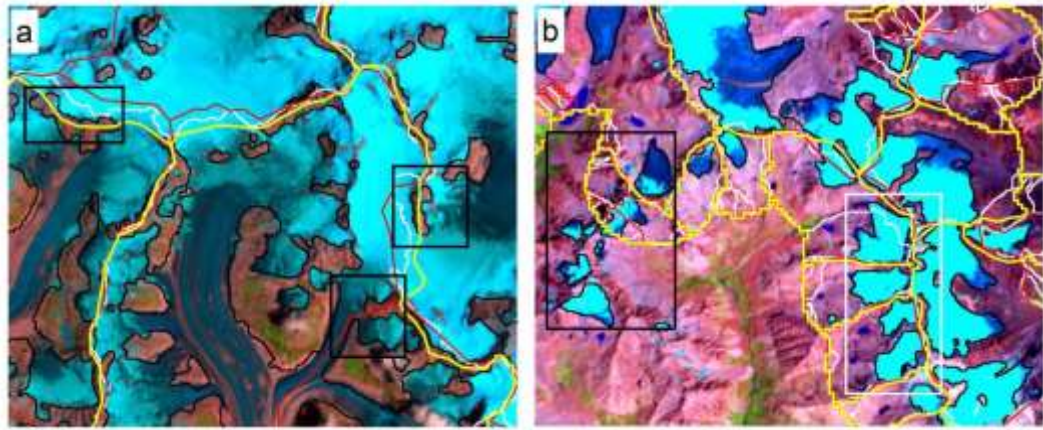


Fig. 3.7 Comparison of basins derived from SRTM DEM (red lines), ASTER DEM (white lines) and manually corrected divides (yellow lines).

Basins derived from SRTM and ASTER DEM show large discrepancy along the margins in the upper parts of glaciers (black boxes in a). Many glaciers are already separated by ridges and do not need to be divided by drainage divides (black box in b) or can be easily isolated by one divides along the ridges (white box in c).

3.3.4. Estimation of ELAs

Estimating ELA of mountain glaciers has been difficult due to a lack of field observations. This study estimated the average ELA for each sub-region of the QTP by averaging kinematic ELAs over typical large glaciers. The kinematic ELAs are determined by employing the ‘Hess method’ (Leonard & Fountain, 2003) which is based on inflection of elevation contour lines on the topographic map. According to this method, the transition or inflection from a concave to convex contour should be close to the location of the long-term average ELA, which can be explained by the glacier motion characteristics (Leonard & Fountain, 2003).

3.3.5. Creation of manual digitized outlines

Outlines of 55 glaciers (~170 km²) are manually digitized to test the accuracy of our mapping method. The digitization is based on Landsat imagery in a GIS and modified with reference to a slope map. We use the same ice divides to separate the glacierized area. The manually digitized outlines fall within different Landsat Path-Row combinations and cover

clean-ice and debris-covered glaciers with a wide range of size classes (0.03 km² - 66 km²). Although a manually digitized data set is considered highly precise, there is inherent error in any GIS-based manual digitization (e.g. Paul and others, 2013) and determination of debris-covered glaciers is particularly difficult. We use surface features such as pro-glacial ponds and deposits in the glacier forefield as a sign of glacier termination when digitizing glacier outlines.

3.4. Results

The 2013 glacier inventory of the SE QTP includes 6892 glaciers larger than 0.02 km², covering a total area of 6566 km². The distribution of glaciers by number and by area per size class (Fig. 3.8a) and per mean aspect sector (Fig. 3.8b) shows the typical patterns of mountain glaciers (e.g. Andreassen et al., 2008, Frey et al., 2012). In this region, glaciers smaller than 1 km² accounted for 83.7% of the total number, but they share only 20.6% of the total area. On the other hand, the 10 largest glaciers (size larger than 50 km²) cover about 13% of the glacierized area (865 km²). The mean elevation of different size glaciers indicated that small-size glaciers (less than 1 km²) are distributed at higher elevations (95 m higher) than large-size glaciers. Analyzing the distribution of glaciers versus aspect sector reveals that with the SE-NW direction as a divide, the number and area of glaciers facing the northeast-bound sectors (N, NE and E) notably exceeds that in the southwest-bound sectors (S, SW and W) (Fig. 3.8b). About 55% of the total glacierized area are lying in the northeast-bound sectors. Meanwhile, the mean elevation of glaciers in northeast-bound sectors (5190 m) is 66 m lower than that of the southwest-bound sectors (5256 m).

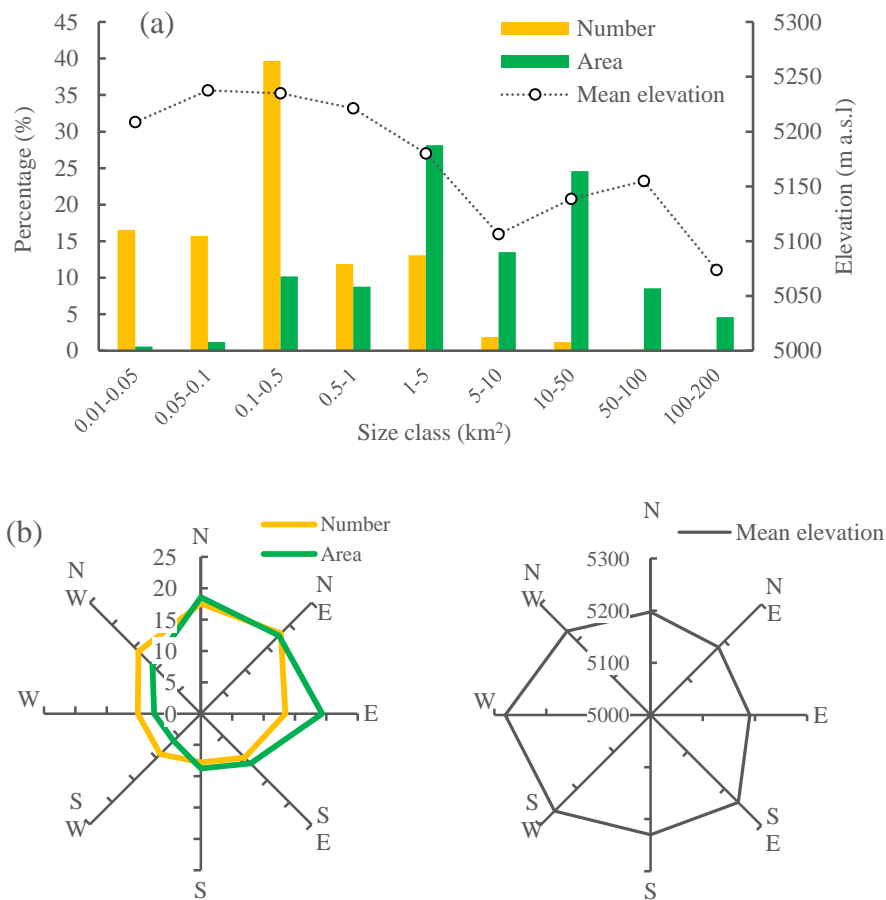


Fig. 3.8 Distribution of the number of glaciers (in %), glacier area (in %), and mean glacier elevations in m, (a) per size class, (b) per aspect sector.

The distribution of clean-ice glaciers and debris-covered glaciers is shown in Fig. 3.9. The number of glaciers with debris-cover is 337, covering about 8% (531.6 km²) of the total glacierized region. Clean-ice (debris-covered) parts have an overall mean elevation about 5234 m a.s.l. (4337 m a.s.l.) with a mean slope of 23.3° (12.1°). All glaciers larger than 50 km² and 84% of the glaciers larger than 10 km² are partly debris-covered. This is consistent with previous observations that debris-covered parts are distributing at the low-lying and less inclined tongues of large valley glaciers (Paul et al., 2004, Frey et al., 2012). The hypsometry of all analyzed glaciers for the study region is shown in Fig. 3.10. Although almost 92% of the total glacier area is debris free, the amount of debris-covered ice is dominant below 4100 m. With the increase of mean elevation, the amount of debris cover shows a general decreasing gradient from about 28% in the southeast (mean elevation < 4500 m a.s.l.) to only 3% in the northwest (mean elevation > 5500 m a.s.l.).

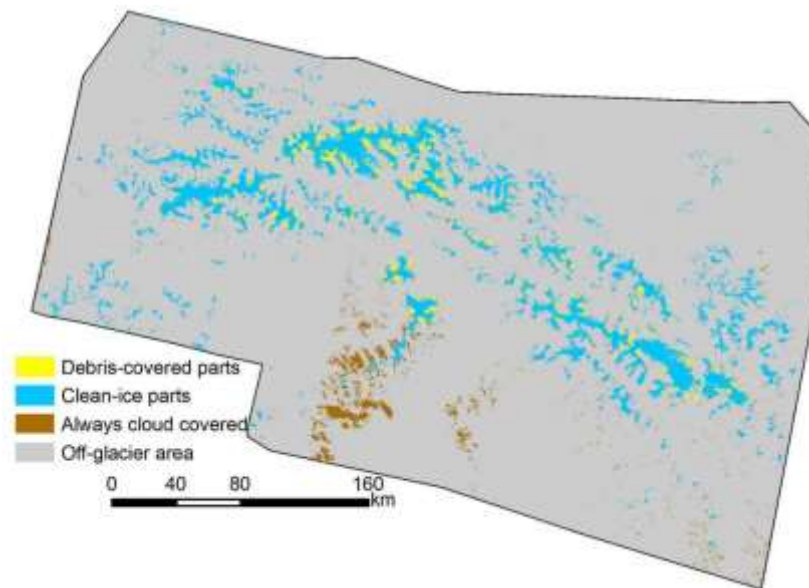


Fig. 3.9. Spatial distribution of inventoried glaciers (including the debris-covered parts and clean-ice parts) and data gaps where images are always cloud covered.

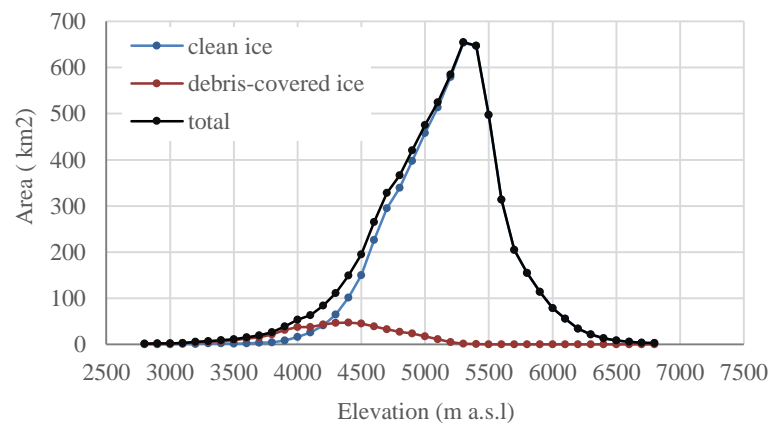


Fig. 3.10. Hypsometry of all glaciers in the study region.

Mean elevation is often used as a good approximation for the balance-budget ELA and thus a suitable parameter to analyze the governing climatic conditions. The spatial distribution of glacier-specific mean elevations reflect such climate dependences in the SE QTP (Fig. 3.11). Following the Yarlung Tsangpo great canyon in a south-north extending, the ISM brings moisture inward, which results in relatively maritime climate in the southern slope and eastern facets of mountain ranges and lowest mean elevation of glaciers (below 4500 m) around the Great Bend of Yarlung Tsangpo (Fig. 3.11). From this place, the mean elevation increases in the direction of southeast-northwest and southwest-northeast

(indicated with white lines with directions in Fig. 3.11), with highest mean elevations (above 5500 m a.s.l. .) in the northwestern and southeastern margins of the study region. The two directions of gradients reflect changes of climate conditions associated with both the extension of large canyons which serve as important moisture transportation path and the raise of high mountain ranges which block intrusion of vapor to the leeward facet and inner highlands.

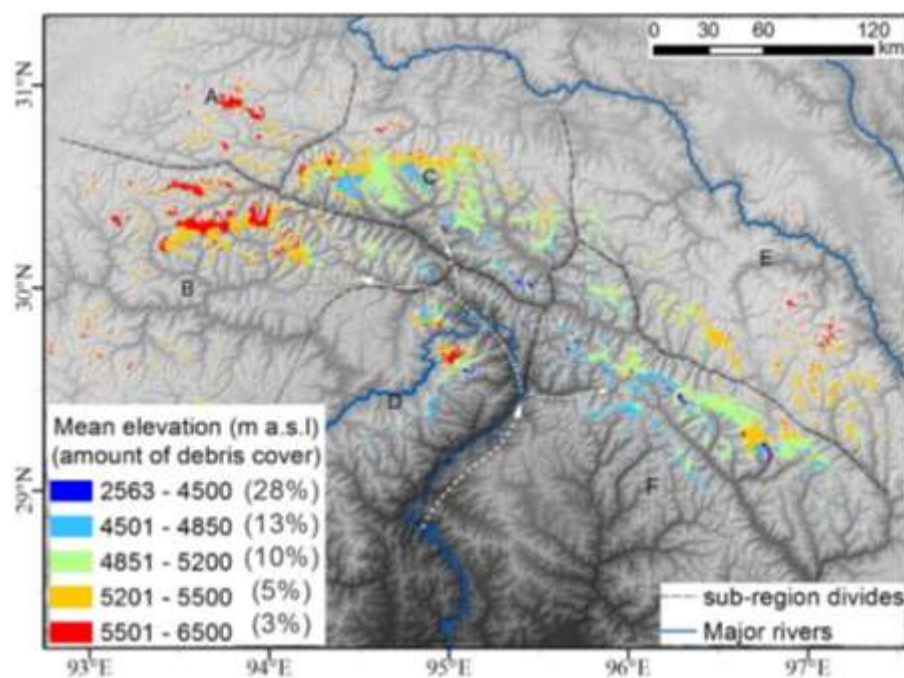


Fig. 3.11. Map of mean glacier elevation of individual glaciers and the relative amount of debris cover in different elevation ranges.

The great bend of Yarlung Tsangbo region have a most humid climate and the mean elevation is increasing in both the northwest and southeast direction (indicated by the white dashed lines). The debris coverage (indicated by the number in brackets in the legend) decreases with the increase of elevation.

The vapor transportation paths along with topography variations result in regional difference in glacier distributions. The study region is divided into six sub-regions, roughly along the major canyons which act as natural divides of different mountain ranges and climate differentiation (Fig. 3.11). Table 3.2 gives a summary of selected parameters for each sub-region, and it shows regional difference of glacier distribution in terms of size, mean elevations and debris cover. Sub-region A in the northwest represent the high inner

plateau where climate is relatively dry-cold and less influenced by the monsoon. Glaciers over the regions are characterized by high elevations, low coverage of debris cover and small sizes (mean size below km²). Sub-region C, D and F in the south and east have relatively maritime climate due to influences from the summer monsoon, resulting in low mean elevations, high amount of debris cover and large glacier sizes (dominated by size class between 10 and 50 km²) (Table 3.2). About 48%, 22%, 12% of the total debris-covered area are distributed in sub-region C, F and D respectively (Fig. 3.11). It is interesting to note that glaciers in sub-region F in the south bank of Parlung Tsangpo have lowest mean elevation (below 5000 m), in contrast with 400 m higher elevation over sub-region E in the north bank, which reflect maritime/dry climate in the south/north side of mountain ranges. The mean size of glaciers over sub-region C is largest (1.71 km²). The estimated mean ELA for each sub-region is consistent with the pattern of mean glacier elevations (Table 3.2 and Fig. 3.12). Based on the Hess method, lowest mean ELA (4800m) are found in sub-region D and F, while mean ELAs in the sub-region A and E are over 300 m higher than that in D and F (Table 3.2).

Table 3.2 glacier parameters per sub-region of SE QTP. ELA values are estimated based on inflection of elevation contour lines on the topographic map (SRTM DEM).

Sub regions	Num of glaciers	Glacier area (km ²)	Mean glacier size (km ²)	Mean elevation (m a.s.l.)	Median elevation (m a.s.l.)	Mean slope (°)	ELA (m)	Debris coverage (%)
A	731	333.3	0.5	5484	5457	21.9	5150	3.2
B	1945	1459.3	0.8	5372	5420	26.0	5000	4.7
C	1169	1906.5	1.7	5096	5153	21.8	4850	13.3
D	324	383.0	1.2	5056	5003	29.9	4800	16.3
E	1366	752.3	0.6	5316	5344	16.9	5300	2.8
F	1336	1740.2	1.3	4951	4935	21.0	4800	6.7

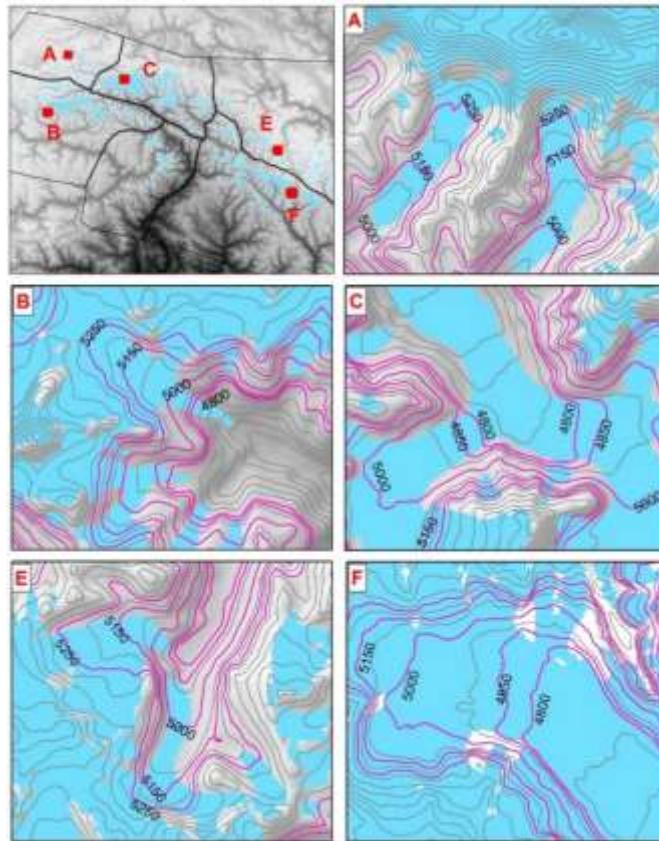


Fig. 3.12. Contour maps for typical glaciers in SE QTP and the estimated ELA. The red rectangles in the overview map indicate the location of glaciers shown in A, B, C, E and F which are respectively located in the selected five sub-regions. Purple contours with black labels in the map are contours for the ELA estimates (4800 m, 4850m, 5000m, 5150m and 5250m). Blue filled polygons are inventoried glaciers and the grey topography contours are in 100 m interval.

3.5. Discussion

3.5.1. Glacier inventory data and accuracy

The manually digitized glacier outlines (as control data set) are distributed over four heavily glacierized sub-regions (Fig. 3.13). There is good agreement between our glacier inventory and the control data set, despite that the former exhibits noise edges ((Fig. 3.13). The 55 control glaciers have a total area of 176.3 km² in the control data set, compared with 171.4 km² in our generated glacier inventory. This is equal to an overall -2.9% percentage difference (total areal difference divided by the total glacier area). The 30 median-to-large glaciers (>0.2 km²), covering 95% of total area, show stable extents in the two data sets, with areal percentage difference varying between -7% and 3% (-2.5% on average); while

10 smallest glaciers ($< 0.1 \text{ km}^2$) tend to be 10% smaller on average in our generated glacier inventory than in the control data set. This is reasonable as our retrieved outlines represent conserved glacier extents by mapping minimal area with multi-temporal Landsat scenes, whereas the manual digitized data set is referred to a single Landsat scene. This effect can be particularly obvious for small glaciers which tend to show fast temporal variations (Dyurgerov and Meier, 2000). Although the number of digitized glaciers may be not enough, we consider the validation as roughly representative and estimate an uncertainty of 3% for the total mapped glacier area (6566 km^2).

The total number of mapped glaciers (6892) depends on the minimum size threshold (here, 0.02 km^2). If this value is set to 0.05 km^2 , the number reduces to 5783, covering a total area of 6529 km^2 . In the CGI2, the total number of glaciers $>0.05 \text{ km}^2$ is 6122 and the total area is 9744.6 km^2 . The considerable difference in the glacier area ($>3000 \text{ km}^2$) may partly be explained by glacier changes (retreat). However, it is more likely that the glacierized area in the CGI2 was overestimated due to errors such as misclassification of proglacial lakes, seasonal snow cover and inaccurate inner ice boundaries (Fig. 3.13). The quality of CGI2 is inconsistent across the study area, with remarkable overestimation in the heavily glacierized region in the central and southeastern part, yet acceptable quality in the northeastern part (Fig. 3.13). We speculate that the inconsistent quality is probably associated with different qualities of reference data for updating CGI2, despite that it is unclear which images were used for different parts.

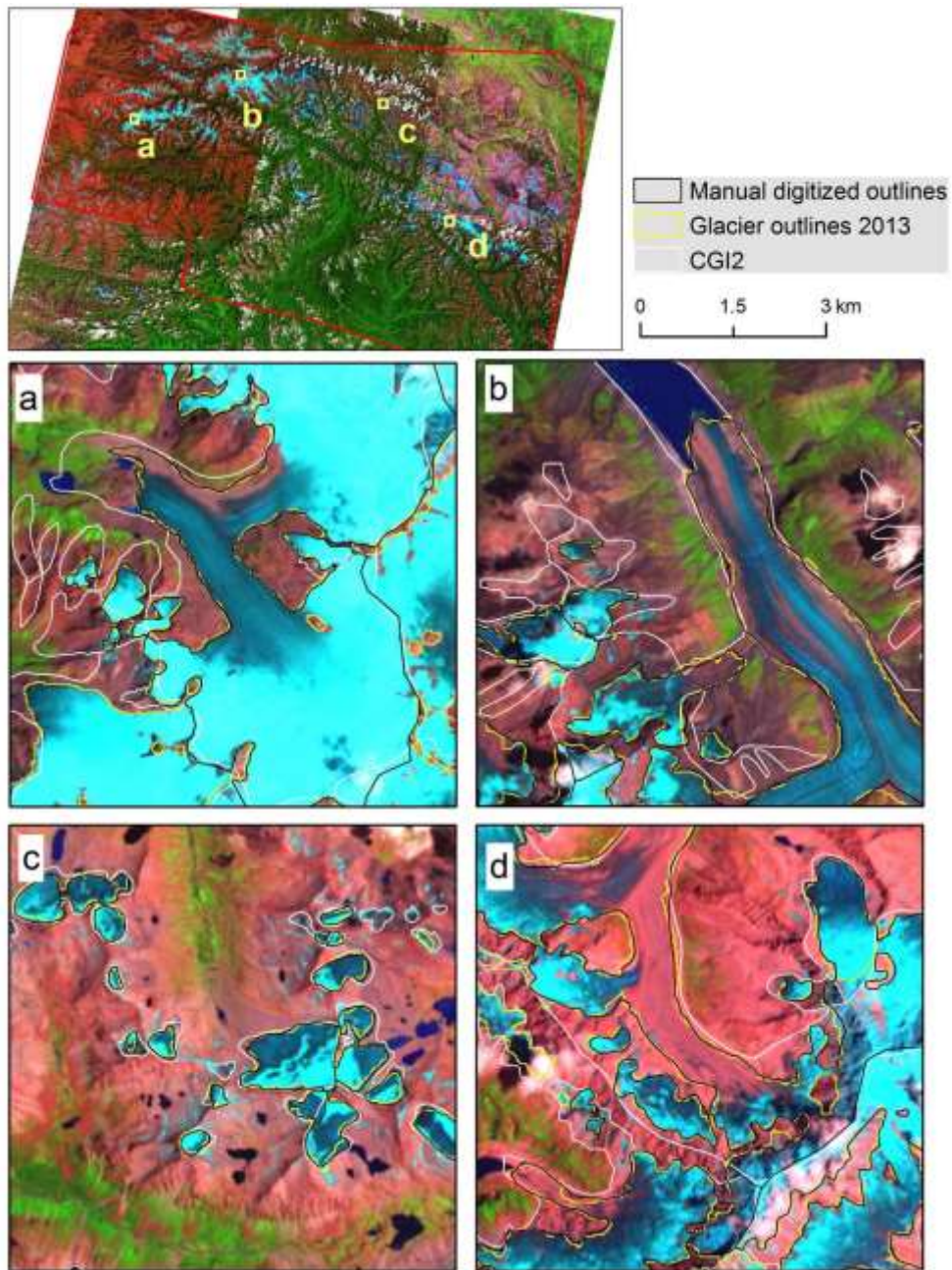


Fig. 3.13. The 2013 glacier inventory generated in this study compared with a couple of manually digitized glacier outlines and the second CGI (CGI2).

Outlines are superimposed on false color composite of Landsat 8/OLI images (b754) acquired in September 28, 2013 (A) and August 4 2013(B,C and D).

Under cloud-free conditions, the automated clean ice mapping method is assumed to have an uncertainty of ± 1 pixel (30 m) in the outline positions, according to previous validations (e.g. Paul et al., 2002, Andreassen et al., 2008). The primary uncertainties lie in use of partly cloud-covered images, which demands high accuracy of cloud mask generation and

geometric accuracy of different images. The failure of identifying clouds over the glacierized area probably leads to erroneous classification as non-glacier in the final result. Fortunately, the Fmask tool can produce high-accuracy result and the threshold parameters in the tool are flexible to derive cloud extents in different probability. It is better to check the accuracy the cloud mask and dilate it with 1-3 pixels to ensure complete mask out of cloud-affected region. The Landsat 1G products, particularly the Landsat 8 scenes, have high geometric accuracy within 13 meters (less than on-pixel resolution (Storey et al., 2014) , making the based of accurate mosaic of different scenes. Note that data gaps still exist in the south of region due to persistent orographic cloud cover, despite of use of several scenes (Fig. 3.9). However, they only account for a small percentage of the total study area (6%), and these regions are less glacierized according to CGI1. The glacier extent over these regions were manually determined by referring to CGI1 and PALSAR coherence which is helpful to reshape the glacier outlines.

The accuracy of applied DEM affect the glacier inventory mainly in two ways: the generation of glacier divides and the retrieved topographic parameters of glaciers. There may be local shifts between the Landsat imagery and SRTM, as revealed by the differences between drainage divides derived from SRTM and interpreted from Landsat (Fig. 3.7). The uncertainties in glacier divides, however, have little influence on the total mapped glacier area. By taking account of these error sources, an additional 3% uncertainty was estimated in the generated glacier outlines.

3.5.2. Semi-automated debris mapping with coherence

The semi-automated mapping of debris-covered ice by applying thresholds and overlay of multi-source masks is straightforward and efficient to map glaciers in an extensive region. However, quantitative assessment of mapped debris-covered parts is hardly possible due to absence of ground truth. Qualitative validation was conducted by comparing the outlines with manually delineated outlines which were referred to coherence images, slope and Landsat false-color composites. The validation confirms the differences in area are below

4%. It is worth noting that manual interpretation of debris-covered parts solely based on slope and Landsat images can be misleading as there are many glacier-tongue shapes which turn out to be non-glaciers with high coherence values (Fig. 3.14). This demonstrates the necessity of employing coherence information in debris-covered ice mapping. The absence of ice under these glacier-tongue regions may be a consequence of de-glaciation in recent decades due to warming climate.

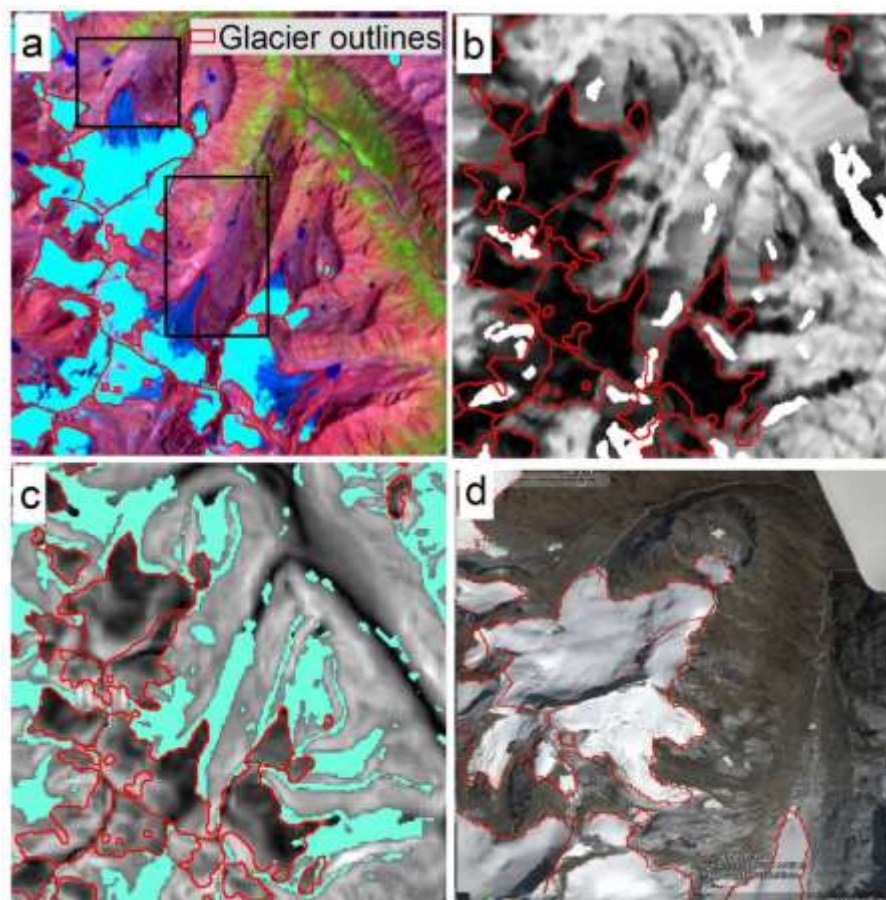


Fig. 3.14 An illustration of challenging conditions for identifying debris-covered ice over the SE QTP.

Some areas (black rectangle in (a)) with glacier tongue-like topography and connected with a clean-ice glacier turns out not to be debris-covered glacier, as (b) shows relatively high coherence values compared with the surrounding non-glacier region. The shaded green areas in (c) highlight tongue-like topography determined by overlaying non-clean-ice, low slope, non-water and non-vegetation masks. (d) Close-up detail about the black rectangle area based on high-resolution images (acquired on 8 November 2014) from Google Earth.

3.6. Conclusions

With a combination of multi-source information from the latest Landsat observations, SRTM DEM and SAR data, this section presents a semi-automated approach for generating a glacier inventory for the SE QTP under challenging mapping conditions (significant terrain relief, debris cover and serious effects from clouds). We propose a semi-automated scheme to combine the multi-temporal and multi-source data, based on simple rules of data selection and processing. Most thresholds used for map segmentations are based on distribution of image values (e.g., NDSI, NDVI, and NDWI) and most processing steps are semi-automated and pixel-based, significantly reducing the requirement of manual editing and improving the accuracy of glacier mapping. To map debris-covered glacier tongues, we have extended the multi-source method proposed by Paul et al (2004) by adding coherence images from SAR data. Including such information is essential and necessary as many glacier-tongue shapes turn out to be non-glaciers in this region. The proposed method can potentially be used for glacier mapping in similar regions including the Himalaya.

The new glacier inventory for the SE QTP is the most comprehensive to date for the region. The study has also revealed that the glacierized area in CGI2 was significantly overestimated (>30%) probably due to the use of cloud-free images that may contain large seasonal snow cover. The new glacier inventory identifies 6892 glaciers >0.02 km², covering a total area of 6566±197 km² (3% uncertainty). The debris-covered glacierized areas account for about 8% of the total area (532 km²), and they are restricted to lower elevations (mostly below 4600 m) with moderate terrain gradients. From the eastern and southern Nyainqentanglha ranges to the inner plateau in the northwest, there is an increase gradient in the mean glacier elevation and a general decreasing trend of debris coverage, reflecting different climatic, topographic and geological conditions. The new glacier inventory will benefit future glacier studies including assessment and modelling of glacier changes and the impacts on run-off, projecting glacier developments and glacier lake hazards.

Chapter 4

Estimates of glacier mass balances over the central QTP with multi-source data

4.1. Introduction

Glacier mass balances over the QTP have been reported in previous literature based on different methods and data. These investigations can be roughly classified into in-situ mass balance determination and remote sensing based results. The in-situ mass balance measurements by glaciological methods are direct and reliable, but such observations are limited to a very small number of small-scale glaciers and biased to low-lying and more accessible glaciers. The development of remote sensing techniques enables comprehensive investigation of glaciers from different aspects. At present, a number of glacier parameters, including length, area, elevation and ice velocity, and the changes in them can be determined by different remote sensing data, with near global coverage and regular revisit.

Numerous studies have investigated the areal or length changes of glaciers by using optical images derived from Landsat MSS/TM/ETM+, ASTER, LISS, CEBERS and SPOT (Lu et al., 2002, Narama et al., 2010, Yao et al., 2012). Such one- or two-dimensional glacier change measurements are now complemented by the 3D dimensional observations, i.e., glacier-thickness (or elevation) changes. The thickness or elevation information is mainly from geodetic measurements such DEMs derived from data of different dates and GPS (Rignot et al., 2003, Berthier et al., 2007, Shanguan et al., 2008, Li et al., 2010b). Recently, multi-date elevation data are available from the new generation of satellite laser altimetry GLAS carried by ICESat which was operational from 2003 to 2009. GLAS/ICESat data have been widely applied in monitoring glacier changes in Antarctica and Greenland (Smith et al., 2005, Slobbe et al., 2008, Ewert et al., 2012). The application of ICESat data over mountain glaciers, however, requires special analyzing method because of the sparser

distribution of measurements over the low-latitude region and the more rugged terrain compared to ice-sheets over the Polar Regions (Sauber et al., 2005, Kääb et al., 2012).

In general, mass balances, area or length changes and thickness changes are measured in different dimensions (three dimensional, two dimensional or one dimensional), derived from various source of data (e.g. in-situ, optical images, geodetic data), and they are often interpreted separately. These measurements can be linked internally, whereas their consistency is seldom evaluated. Different types of data have different limitations (spatial and temporal coverage, resolution, types of observation, etc.), and the applied methods for estimating glacier changes are mostly based on certain assumptions. To derive consistent estimates of glacier changes, these limitations and uncertainties need to be addressed. On the other hand, the increased availability of observations from different sensors provides a potential of a consensus estimate of glacier changes by combining the multi-source data. For example, with glacier mapping from optical data and elevation change from geodetic estimates, it is now possible to estimate glacier mass balance with improved accuracy over extended regions (Barry, 2006, Kääb et al., 2012).

In this section, with a focus on glaciers in the Dongkemadi (DKMD) region in the central QTP, glacier changes in recent years are investigated by combining sequential multi-spectral images from Landsat satellites and elevation measurements from ICESat. All available high quality Landsat scenes are selected to detect the glacier areal changes since 2000. Volume changes and mass balances of regional glaciers are then estimated based on the areal and elevation data, and the results are evaluated with in-situ measurements.

4.2. Study area and datasets

4.2.1. Study area

The glaciers are located at the headwaters of the Yangtze River on the northern slope of the Tanggula Mountain (33°3' -33°10'N, 91°59' -92°8'E). The study glaciers consist of a

cluster of valley glaciers developed along broad U-shaped valleys and ice caps over the mountain tops (Fig. 4.1). The relatively smooth glacier surface without any avalanche or surface moraines makes it an ideal place for remote sensing based mass balance study (Pu et al., 2008). The XDG in the southern slope of the ice body is relatively accessible due to its low elevation ranges and smooth surface and has been monitored with field measurements of mass balances since 1989.

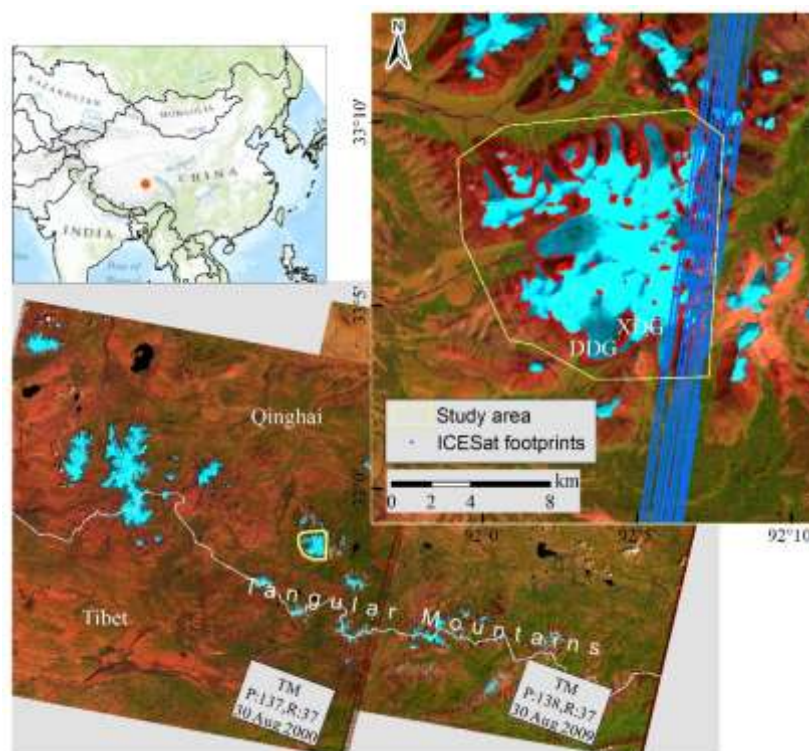


Fig. 4.1 Overview of the study region and glaciers the Tanggula Mountains, in the central QTP and the crossing ICESat tracks.

The red glacier outlines were retrieved from the background images which was acquired on August 30th, 2000. Color images are false-color composite of Landsat/TM images from bands 7 (red), 4 (green) and 2 (blue).

4.2.2. Datasets

There are about 30 Landsat TM/ETM images covering the study glaciers during 2000-2011 on the USGS Landsat archive. Despite of a considerable number of images acquired, the number of useable images is limited due to seasonal snow and cloud cover. A total of five multi-spectral Landsat TM images were selected in this study (Table 4.1). The selected

images were acquired around the end of ablation season (Late August or earlier September), and are cloud-free over the study glaciers. All the five Landsat images are orthorectified Level 1T standard products processed with systematic radiometric and geometric correction in Universal Transverse Mercator (UTM) map projection.

Table 4.1 List of Landsat images used in this study

Sensor	Scene date (day.month.year)	Spatial resolution (m)	Landsat path/row
Landsat5/TM	30.8.2000	30	137/37
Landsat5/TM	10.9.2004	30	137/37
Landsat5/TM	2.8.2007	30	137/37
Landsat5/TM	30.8.2009	30	138/37
Landsat5/TM	29.8.2011	30	137/37

Elevation data from ICESat are used to detect the inter-annual thickness change of glaciers. This study uses level-2 ICESat GLAS Data product-GLA14 of release 33 (Zwally et al., 2002) from the NSIDC. There are 14 repeated tracks (from March 2003 to November 2008) covering the study glaciers (Fig. 4.1). The GLA14 product comprises corrected surface elevations referenced to the TOPEX/Poseidon ellipsoid, geoid heights, saturation flags and other information. We extracted the latitude, longitude, elevation, and geoid data of the footprints by the GLAS Visualizer and NSIDC GLAS Altimetry elevation extractor Tool (NGAT).

The repeated tracks of ICESat did not overlap exactly, resulting in maximum distances of 2.4 km. Direct comparison of ICESat elevation measurements is hence unreasonable due to the rugged terrain. This study used the 90-m gridded SRTM DEM as a consistent topographic reference. The version 2 SRTM3 DEM (90m gridded) was suitable as it has no filling patches and no horizontal misalignment when registered to ICESat data (Kääb et al., 2012, Neckel et al., 2014). The dataset is available at the USGS at http://dds.cr.usgs.gov/srtm/version2_1/SRTM3/. The SRTM DEM is orthometric height with respect to WGS-84 ellipsoid and EGM 1996.

4.3. Methodology

4.3.1. Mapping glacier extent and the areal changes

A semi-automatic approach based on the NDSI is used to map the glacier area (clean ice with no debris cover) on a pixel-by-pixel basis. It consists of three decision rules,

$$\begin{cases} \text{NDSI} \geq 0.4, \text{NDSI} = (\rho_{\text{band}2} - \rho_{\text{band}5}) / (\rho_{\text{band}2} + \rho_{\text{band}5}) \\ \rho_{\text{band}2} \geq 0.1 \\ \rho_{\text{band}4} \geq 0.15 \end{cases} \quad (4-1)$$

where $\rho_{\text{band}2}$, $\rho_{\text{band}5}$ and $\rho_{\text{band}4}$ denote reflectance at band 2, band 5 and band 4 of TM images respectively (Riggs et al., 2006). A threshold of 0.4 for NDSI has been proven effective to segment the scenes into snow/ice and snow/ice-free areas (Hall et al., 1995a). The second and the third rule respectively assists the differentiation of snow/ice from densely vegetated areas and water bodies. Particularly, this study determined the third threshold empirically by comparing band reflectance over proglacial lakes with that over glaciers.

Post-processing is performed to correct misclassifications due to shadow and cloud contamination along glacier marginal, by superimposing the classified map on the false-color composite Landsat image. We exclude small individual glaciers, particularly those clearly outside the glacier area and with an area $< 0.02 \text{ km}^2$, as they might represent seasonal snow cover.

4.3.2. Determination of glacier elevation changes

1. Preprocessing of ICESat data

ICESat product provided ellipsoidal height measurements referred to TOPEX/POSEIDON Ellipsoid (i_{elev}), while SRTM DEM is orthometric height referred to WGS84 Ellipsoid and EGM96 Geoid. To make them comparable, the ICESat ellipsoidal height measurements are converted to the same reference of SRTM with the following formula:

$$I_{hgt} = I_{elev} - 0.7 - I_{geoid} \quad (4-2)$$

where I_{hgt} is orthometric height with the same reference of SRTM and I_{geoid} is the EGM96 geoid height referred to WGS 84 Ellipsoid at the location of the footprint (longitude and latitude) according to the model provided by NGA/NASA (<http://earth-info.nga.mil/GandG/wgs84/gravitymod/egm96/egm96.html>). The offset 0.7 m is a rough estimate of the vertical difference between WGS84 Ellipsoid and TOPEX/POSEIDON Ellipsoid. Bilinear interpolation is used to extract the SRTM surface elevation at the location of each ICESat measurement. The elevation difference (dh) between ICESat estimate and SRTM DEM ($I_{hgt} - I_{srtm}$) represents the elevation change at the sampled footprint.

2. Classification of ICESat footprints

We adopt the Landsat TM image acquired at August 30th, 2000 to classify ICESat footprints into glaciers, off-glacier and water-body. Landsat data is selected from the year 2000 as this year is close to the acquisition date of SRTM which is considered as a consistent topographic reference for analyzing elevation changes. A 10-km buffer of the outline is used to limit the off-glacier footprints close to glaciers (Fig.1). Footprints over water-bodies including subglacial lakes are identified manually by superimposing them over the Landsat image and were excluded in the off-glacier analysis. The off-glacier trend is examined to check the reliability of ICESat trends over the glacier area.

3. Filtering of ICESat data

As ICESat measurements can be affected by thick cloud cover and atmospheric disturbances, large dh values over the ice body may not represent real glacier changes. A threshold of 150 m is used to filter obvious errors of dh and to keep most real glacier changes, similar to previous studies (Gardner et al., 2013; Kääb et al., 2012). In addition, there may exist large systemic errors in one laser period. For example, the mean dh for one ground track (one laser period), mostly ranges from -0.5~-2.8m with standard deviation (*sd*)

ranging from 1.5-4.8; however, the average dh measured in laser period 3H (March 28th, 2007) reaches 34.4 m with *sd* 47.78. The large systemic bias indicate certain problems of measurements in this track. Therefore the measurements in this laser period are all excluded in the analysis.

4. Correction of ICESat sampling

The distance between repeated tracks results in difference in sampling distribution of ICESat measurements over the glaciers. The varied elevation sampling probably induces a bias, both for the average dh value of individual laser periods and for the dh trends, as the variation of glacier thickness, off-glacier snow thickness, and perhaps also terrain-related ICESat elevation errors, on average correlate to elevation (Kääb et al., 2012). We mitigate such biases by adjusting the original dh means of each laser period to the estimated dh at the same altitude (mean SRTM elevation of all footprints of the same season). The adjustment is based on the assumption that there is a linear relationship between melting rates and elevation (Koji et al., 2000). Such linear relationship is estimated based on dh and SRTM elevation for each laser period. Robust fitting method is preferred to regular linear fitting as it is less sensitive to noises presented in the data. The robust method operates using an iterative re-weighted least squares approach in which points that are farthest from the first regression model are excluded in the next iteration until the regression coefficients converge. The MATLAB cftool toolbox (with Robust option “on” in Fit options) is used to do the fitting of linear relationship between dh and elevation.

The following equation shows how to correct the elevation differences dh at certain elevation H to a modeled elevation difference at the mean elevation level:

$$dh_{cor} = dh + (H_{mean} - H) \cdot Grad_{dh} \quad (4-3)$$

where dh_{cor} is the corrected elevation difference at the footprint, dh is the mean elevation different in the ground track containing the footprint, H_{mean} is the mean SRTM elevation in the track and H is the SRTM elevation at the footprint. $Grad_{dh}$ denotes the gradient of

elevation difference, that is, the slope coefficient of the linear regression between dh and elevation.

5. Trend fitting of elevation differences

The inter-annual thickness changes of glaciers was determined by fitting the trend of mean over-glacier dh (corrected with (3)) in the same season. As there are only three laser periods in winter (February/March) and two in summer (June/July), only data acquired in autumn (October/November) in six laser periods were used to study the trends. We derived inter-annual dh trend through a linear regression of the mean values of dh with the acquisition date. The dh trend represents the mean trends of elevation changes over the glacier during 2003-2008. The dh values derived by linear extrapolation of the trend back to the SRTM acquisition date of February 2000 reflect the elevation offsets between ICESat and SRTM, which are probably caused by penetration of SRTM into snow/ice (Kääb et al., 2012). The bias reflect a coarse estimation of SRTM penetration and therefore need to be in a reasonable range for justified trends. Statistically, trend fittings are evaluated with goodness of fit R^2 and p value (for test of the significance of trend). The standard error (se) of dh in each laser period is computed as the standard deviation of dh divided by square root of the number of footprints.

4.3.3. Estimation of glacier mass balances

Glacier volume changes and mass balances are estimated with two methods. One is based on the volume-scaling model, which refers to a generalized logistical relationship between glacier areas and volumes (Bahr, 1997b) and has been applied in various studies. A volume-scaling model has been empirically developed for glaciers over Tian Shan in the northern QTP based on field measurements of areas and snow/ice depth of glaciers (Liu et al., 2003). With a scenario of density for ice/snow, we use this empirical relationship to estimate the mass budgets, as shown in (4-4)

$$M = V \cdot \rho = 0.04 \cdot S^{1.35} \cdot \rho \quad (4-4)$$

where M (kg), V (m^3) and S (m^2) denote the mass, volume and area of a glacier respectively; ρ (kg/m^3) is the average density of ice/snow. The other method is to combine the areal data and the elevation change with the following equation:

$$\Delta B = S \cdot \Delta H \cdot \rho \quad (4-5)$$

where ΔB and ΔH respectively represent the cumulative mass balance (kg) and the average thickness change (m) compared to the reference year (in this study all are referred to year 2000, as we computed elevation change by referring to topographic reference of SRTM 2000); ρ and S are the density of ice/snow ($kg\ m^{-3}$) and area (m^2) respectively. By dividing the area, the mass balance can be expressed in millimeter water equivalent per year ($mm\ a^{-1}\ w.e.$), which represents the reduced or increased depth (in water depth) if the mass loss or gain is distributed over the whole glacier surface. Based on equation (4-5), the mass balance in $mm\ a^{-1}\ w.e.$ only depends on height change and the density of ice/snow. Without differentiating the accumulation zone from the ablation zone, we estimated the mass balances with a constant density-the average density of snow and ice, $750\ kg\ m^{-3}$, and calculated uncertainties with density varying in the range of $600\ kg\ m^{-3} \sim 900\ kg\ m^{-3}$.

4.4. Results and discussion

4.4.1. Areal changes

Visual inspection of the glacier outlines imposed on Landsat images clearly shows the retreat of glaciers along mountain valleys. Linear trend analysis of the glacier area reveals that the glacier experienced a steady shrinkage during the past ~12 years, as shown in Fig. 2. Overall, the glacier area reduced by 3.01% from $81.7\ km^2$ in 2000 to $79.2\ km^2$ in 2011, with a linear shrinking rate of $0.21\ km^2\ (0.26\%)\ a^{-1}$ ($R^2=0.87$, $p<0.05$).

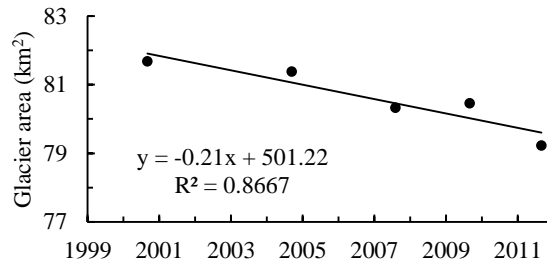


Fig. 4.2 Variation of glacier area in the DKMD region from 2000 to 2011.

4.4.2. Elevation changes

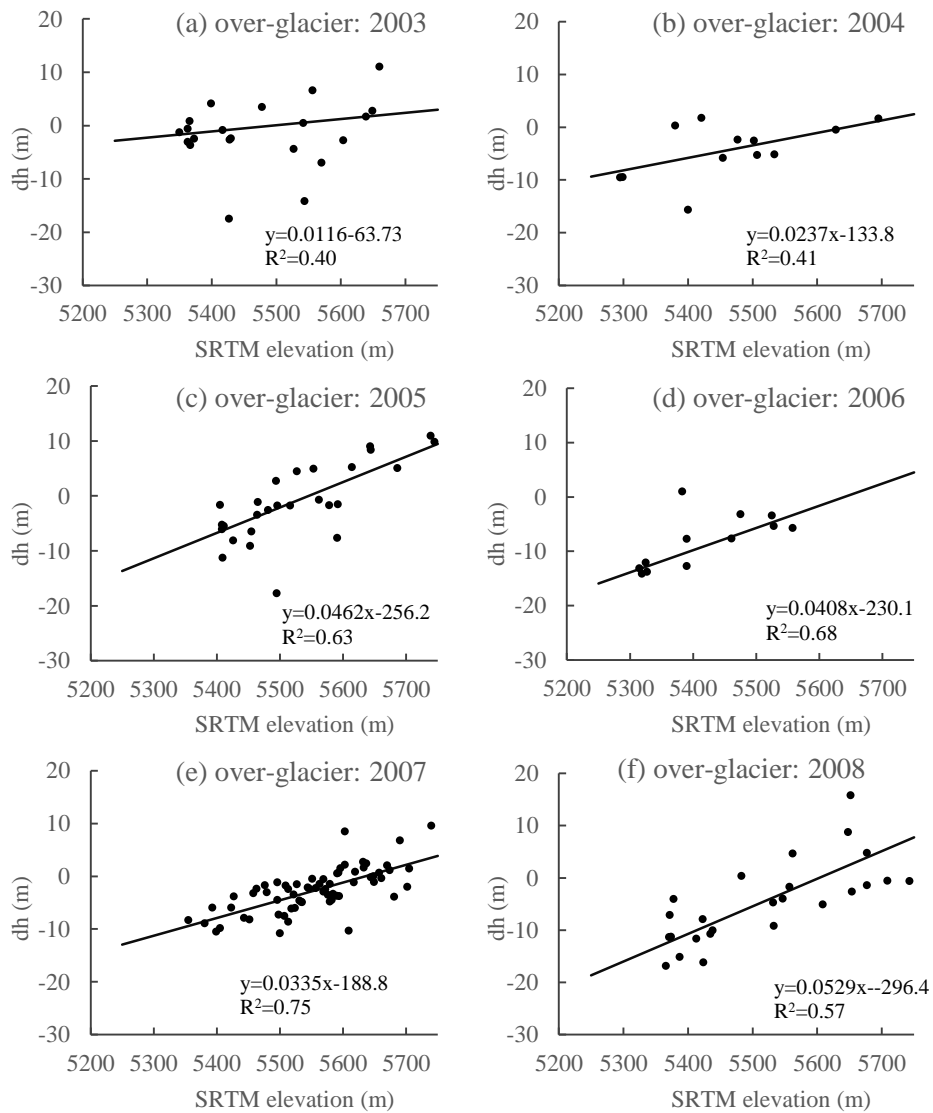
The number of valid footprints used is 166. Details of the footprints over and off-glacier are listed in Table 4.2. While the distribution of off-glacier footprints stabilizes at elevation around 5250 m, the mean elevations of over-glacier footprints vary between 5415-5552 m in different laser periods. Correction of elevation sampling is thus necessary in fitting elevation difference trend. Fig. 4.3 shows the fitted linear relationship between dh and SRTM elevation, and the slope coefficients are the estimated gradients of dh . The gradients of dh vary in the range of 0.012-0.053 $m\ m^{-1}$, with the largest value in 2008 and the smallest in 2003. All dh in autumn season shows an average gradient of 0.034 $m\ m^{-1}$. In contrast, the gradient over the off-glacier area is insignificant (-0.003 $m\ m^{-1}$).

The significant dh gradient along the altitude of glaciers demonstrates a tendency of more negative ablation at lower-elevation area and accumulation at high-elevation area. Assuming a zero elevation difference ($y=0$), the ELA where ablation balances accumulation, can be derived (the value of x for $y=0$). Over the study glacier, the estimated ELA is 5498.7, 5645.6, 5543.1, 5642.5, 5643.1 and 5602.0m from 2003 to 2008, showing a general rising trend of 16.6 $m\ a^{-1}$. The mean elevation during 2003 and 2008, as computed by solving the relationship in Fig. 4.3 for $y=0$, is 5610.1, 10 m higher than previous estimation based on field investigations (Koji et al., 2000, Pu et al., 2008). This confirms that our method of ELA estimation is reliable. The rising ELA tendency in recent years indicates negative mass balances of the glaciers.

Table 4.2 Distribution of footprints in autumn (October/November)

Laser periods	Over-glacier			Off-glacier		
	Num.of footprints	SRTM elevation (mean±se)	Elevation differences (mean±se)	Num. of footprints	SRTM elevation (mean±se)	Elevation differences (mean±se)
2A(11. 2. 2003)	21	5478±23	-1.53±1.37	133	5282±12	-0.91±0.35
3A (10. 20.2004)	12	5466±34	-4.41±1.51	158	5288±10	-1.32±0.25
3D(11.7. 2005)	28	5536±21	-0.99±1.31	125	5272±12	-1.91±0.24
3G (11.10. 2006)	12	5416±26	-8.18±1.44	140	5282±12	-1.05±0.24
3I(10.19. 2007)	67	5552±11	-3.11±0.71	103	5243±11	-1.82±0.29
2D(11.30.2008)	26	5528±26	-3.58±1.90	129	5276±12	-1.38±0.34

(se stands for standard error)



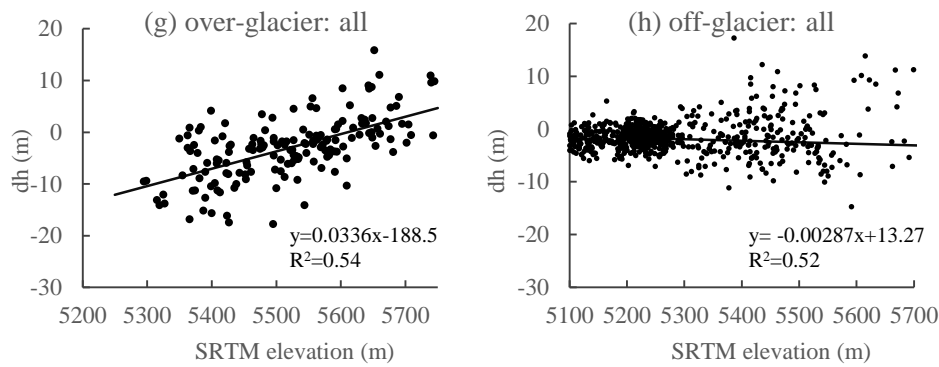


Fig. 4.3 Robust fit of linear relationship between elevation differences and SRTM for different laser periods (a)~(f), for all measurements (g), and (h) for off-glacier footprints.

As shown in Fig. 4.4, the dh trend is modified significantly after correction on the mean dh . For over-glacier areas, the original mean dh shows substantial inter-annual variation with a general decreasing trend (-0.38m a^{-1}) at a low significance level ($R^2 = 0.08$, $p = 0.59$). After correction of the elevation sampling to the same level (5520.4 m), the mean values reveal a significant trend of glacier thinning ($R^2 > 0.6$, $p < 0.01$) at a rate 0.56 m a^{-1} . The SRTM penetration estimated in the corrected trend is 0.6 m, reflecting slight penetration of C-band SRTM into snow/ice in this area, while the penetration estimated in the original trend is -1.16 m. For off-glacier area, dh trend changed slightly after elevation sampling correction, and both are statistically insignificant. The off-glacier dh trend may be attributed to ICESat inter-campaign biases or bedrock uplift (Siegfried et al., 2011, Kääb et al., 2012), and is too insignificant to correct glacier elevation trends.

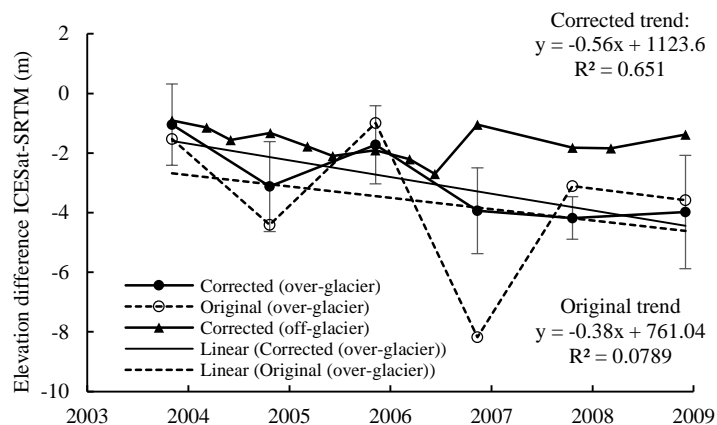


Fig. 4.4 The over-glacier elevation difference trends based on mean values before and after correction and the off-glacier elevation difference.

The se of dh varies in the range of 0.7 m to 1.9 m. The se in principle reflects the spatial variation of glacier thickness changes. However, uncertainties may increase with the large se due to potential uncertainties in both ICESat measurements and SRTM DEM. Over the off-glacier area, in contrast, the standard errors of mean dh is quite stable due to relatively even and adequate sampling.

4.4.3. Volumetric changes and mass balances

The estimated volume changes with volume-scaling model and with the ICESat-derived elevation change trends are shown in Fig. 5. The two estimates both show that the glacier has been in a negative balance since 2000, with a rate of volume loss $0.053 \text{ km}^3 \text{ a}^{-1}$ ($p < 0.05$) from volume-scaling model and $0.045 \text{ km}^3 \text{ a}^{-1}$ ($p < 0.05$) from ICESat height change. The two estimates agree well in depicting the variation and trends of glacier volume changes.

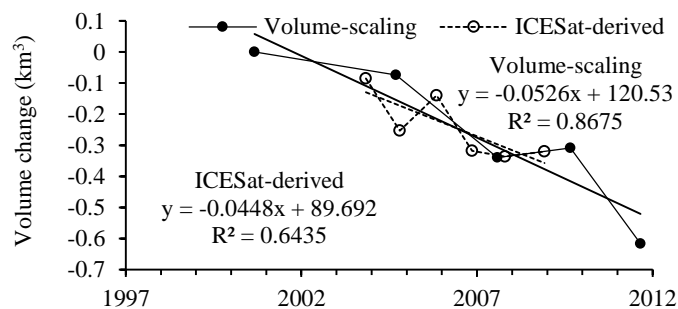


Fig. 4.5 Comparison of volume changes since 2000 derived from volume-scaling model with ICESat-based estimates.

The mass balances derived from the two methods, and comparison with in-situ cumulative mass balance of XDG are shown in Fig. 4.6. Considering the variation of density from 600 kg m^{-3} to 900 kg m^{-3} , the rate of mass loss by volume-scaling model is estimated to be $0.0394 \pm 0.0078 \text{ Gt a}^{-1}$, equivalent to $-487.2 \pm 96 \text{ mm a}^{-1}$. With the ICESat-derived height change model, a linear trend of $-0.0336 \pm 0.0067 \text{ Gt a}^{-1}$ is obtained, equivalent to $-421.2 \pm 83 \text{ mm a}^{-1}$ w.e.. The two estimates show consistent results within the uncertainty extent. The in-situ measurements were derived with the direct glaciological method. About

25 stakes and several snow pits have been set up between 5400 m and 5730 m on XDG to monitor the thickness change of the glacier (Koji et al., 2000). The in-situ data reveal a linear trend of glacier loss at 444.6 mm a^{-1} w.e. over 2003-2008 ($R^2=0.93$, $p<0.01$) (Fig. 4.6), equaling to an average thinning rate of -0.59 m a^{-1} under an average density of 750 kg m^{-3} . The elevation trend is close to our ICESat-derived elevation trend (-0.56 m a^{-1}). Compared to ICESat-derived mass balance, the volume-scaling estimate (-487.2 mm a^{-1} w.e.) deviates more from the in-situ measurements.

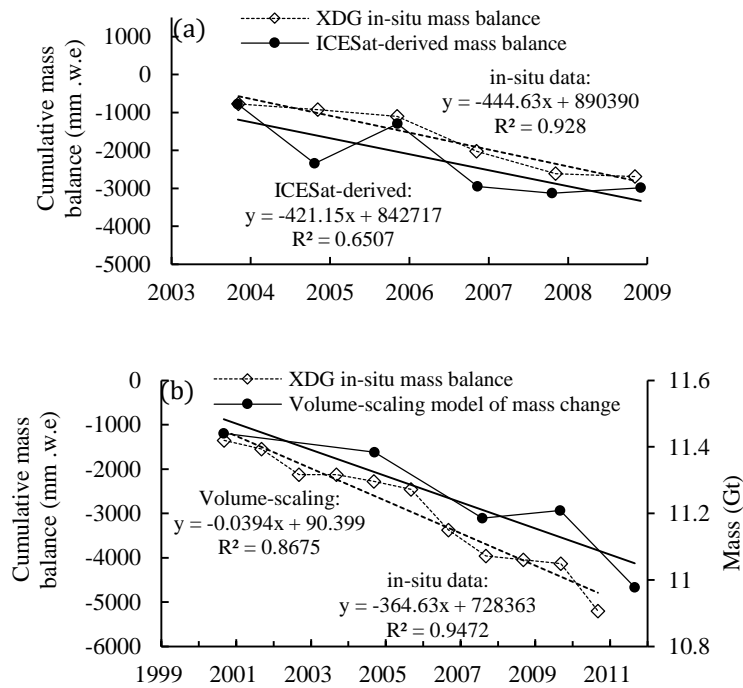


Fig. 4.6 Comparison of in-situ cumulative mass balance with mass balance based on ICESat data (a) and with volume-scaling model (b).

In (a), mass balance in mm .w.e is referred to mass change since year 2000; in (b), mass balance based on volume-scaling model is represented in mass change, while in-situ data is in water equivalence (w.e.).

4.4.4. Uncertainties, limitations and implications

The mapping uncertainty is assumed to be $\sim 3\%$, considering possible misclassification due to shadow, seasonal snow and elimination of small ice patches. This accuracy is similar to previous studies which reported a mapping uncertainty of 2-3% for clean-ice glacier (Paul et al., 2002b, Yao et al., 2012). The decreasing rate of area at -0.26 \% a^{-1} for 2000-2011

derived in this study is less than in other parts of QTP (Yao et al., 2007), but it is slightly faster than the average rate of $-0.20\% \text{ a}^{-1}$ for DKMD glaciers over the 1960s-2001s, which was based comparison of a topographic map (1960s) with satellite images (Landsat or ASTER) acquired around 2001 (Yao et al., 2012). Despite of differences on the study periods and employed data, the faster decreasing glacier area may indicate the aggregated recession state of glaciers in recent years. In the nearby region-Geladandong Moutains, about 90 m to northwest of this study area, accelerated glacier recession was observed in previous research (Ye et al., 2006). The acceleration may be linked with the significant warming trend over the QTP in the 21st century, which has been revealed in prior studies (Schneider et al., 2009, You et al., 2010). Detailed investigation on the glacier-climate relationship in this region requires long-term observations of glacier changes and climate dynamics.

There are studies reporting elevation changes of two glaciers in the area: DDG and XDG, by comparing old DEM constructed from historic topographic maps (1969) with new contemporary elevation measurements such as SRTM DEM (Li et al., 2010b) and GPS (Shangguan et al., 2008). The estimated elevation change rates varied from -0.20 m a^{-1} to -1.1 m a^{-1} , depending on the specific study glacier, the study period and used data. The former study estimated a lowering rate of -0.67 m a^{-1} for the DDG over 1969-2000, which is similar to our estimates. The latter study indicated the accelerated glacier thinning over XDG (from 1969 to 2007) by combining GPS, in-situ data and DEM. It is hard to assess the result, however, without error estimates considering differences in data datum, spatial and temporal sampling. It is therefore important to examine data consistency and differences in investigating glacier changes. In this study the ICESat-based elevation change trend is consistent with areal changes derived from Landsat images, as well as with the mass balances derived from in-situ measurements.

The volume-scaling model seems to be a good bridge between areal observations and mass balance of glaciers. One main uncertainty lies in the density assumptions, as it is hard to

determine the average density for volume-scaling model (a measurement of the average density of glacier) since it can vary with time and regions. The density assumption has less effect on the elevation-based estimates, as the changes mostly occur below the mean ELA. ICESat data have been applied in investigating mountain glacier changes over the QTP, mainly focusing on large-scale regions (Kääb et al., 2012, Gardner et al., 2013, Neckel et al., 2014). A major concern about applying ICESat in small regions is about data representativeness, specifically, whether the spatial sampling of elevation measurements over the glacierized region is even or biased. In fact, ICESat footprints sample a small proportion of the glacier area and elevation distribution of sampled area varies in different laser periods. The method we developed for correction of such biased sampling may suffer from uncertainty of inaccurate estimation of the gradient if there are statistically insufficient samples (<10) in one laser period or the range of altitude sampled by ICESat is too narrow to determine the gradient. It is also important to note that with such correction we only attempted to derive an average elevation changing trends around the sampled area. The derived elevation changes generally agree with regional glacier areal changes and mass balances of XDG. In addition, the accuracy of ICESat elevation over mountain regions, especially errors associated with slope, saturation and surface roughness is hard to evaluate without enough crossover footprints. Nevertheless, the insignificant variation outside the glacier region, demonstrated the relatively stability of ICESat data over mountain glaciers. Other possible interpretation of the elevation differences over the glaciers, such as contributions from bedrock uplift and post glacier response is unclear and not discussed in this study.

4.5. Conclusions

The areal data derived from five Landsat scenes have shown that the glacier area reduced steadily at a linear rate of 0.21 km^2 ($0.26\% \text{ a}^{-1}$). The ICESat data reveal a decreasing rate of 0.56 m a^{-1} over the glacier area, after correction of the biased sampling of measurements by estimating the gradients in different laser periods. The estimated mass balance (-

$421.2 \pm 83 \text{ mm a}^{-1} \text{ w.e}$) agrees well with in-situ measurements over XDG ($-444.6 \text{ mm a}^{-1} \text{ w.e.}$), as well as with the estimates from volume-scaling models ($-487.2 \pm 96 \text{ mm a}^{-1}$). This section confirms the applicability of ICESat data over mountain glaciers with careful processing of noises and sampling bias. The results demonstrate that using consistent data (areal, elevation, or in-situ data) it is feasible to derive consistent glacier change trends, and the observations from satellite data with different missions may be comparable and combined to achieve a consensus estimates.

The rate of area shrinkage in this study is less than the rate of glacier recession over the past decades in many other part of the QTP, but slightly higher than previous investigations using data of 1969-2001. The rapid rise of temperature over the QTP in recent years may be responsible for the negative mass balances, whereas the detailed glacier-climate relationship requires future research on long-term glacier and climate change.

Chapter 5

Recent glacier changes in the southeastern QTP and the climate forcing

5.1. Introduction

In the SE QTP, where the warm and humid moisture from the Indian Summer Monsoon (ISM) and the East Asian Summer Monsoon (EASM) significantly influences local climates, there is a large number of monsoonal temperate glaciers presented (Shen, 2004, Yao et al., 2010). In-situ mass balance measurements indicated that these glaciers were melting faster than the continental or sub-continental glaciers in recent decades (Shen, 2004, Yang et al., 2008, Yao et al., 2012). Among the numerous glaciers over the region, only a very limited number of glaciers has been examined with field investigations, due to the accessibility and logistical difficulties of the field work. As a result of the practical concerns, in-situ investigations favor small-scale and more accessible glaciers.

Recent multi-mission satellite observations enable comprehensive examination of mountain glacier changes. A conventional way to investigate changes of glacier length, area or snow line and equilibrium line altitudes is to use multi-date optical imagery in combination with DEM data (Berthier et al., 2006; Gardelle et al., 2013). However, high-quality optical satellite images are difficult to obtain for the SE QTP region, due to high-frequent cloud cover during both the monsoon season (mid-May to mid- September) and heavy seasonal snowfalls in cold seasons (November to March). Recently, new geodetic measurements, such as satellite laser altimetry observations from the ICESat and satellite gravimetry from the GRACE, show the potential of monitoring glacier changes in the remote high-relief regions with low sensitivity to weather conditions. Several recent studies applied the ICESat observations to investigate the glacier states in the Hindu Kush-Karakoram-Himalaya region and inner Tibet, and revealed contrasting patterns of glacier changes among sub-regions (Kääb et al., 2012, Gardner et al., 2013, Neckel et al., 2014).

On the other hand, an indirect estimation of regional glacier mass balances can be made by gravity-change detection, which utilizes satellite gravimetry to estimate mass budget within basins or manually defined regions. The estimated mass budget reflects terrestrial water storage (TWS) changes due to glacier variations and other mass redistribution over the earth surface. Prior studies have revealed obvious mass losses in High Mountain Asia (HMA) based on the GRACE data, and speculated that it may be caused by rapid glacier melting during the past decade (Matsuo & Heki, 2010, Jacob et al., 2012, Gardner et al., 2013, Yi & Sun, 2014).

Although previous research provided an overall estimate of glacier mass balances in HMA with the GRACE gravimetry and ICESat altimetry measurements, the potential spatial heterogeneity of glacier changes on fine spatial scales and the relationship with climate change have not yet been addressed. The difficulties lie in the lack of reliable glacier inventory and the accessibility of the relevant climate data. In addition, the spatio-temporal relationships between glacier variations and GRACE-observed mass budgets are still in debate, due to the inconsistent spatial and temporal resolution between GRACE-observed and ICESat-based glacier mass balances, and the complexity in interpretation of GRACE signals. This section analyzes fine-scale glacier changes within the QTP with ICESat data and compared the results with the net mass losses derived from the GRACE gravimetry during 2003 – 2009. Furthermore, the study analyzed the relationships among key climatic variables (precipitation and temperature) and glacier mass balances on seasonal and annual time scales to discuss the sensitivity of glacier changes to climate change.

5.2. Study area

The SE QTP is a broad mountainous area linking the inner plateau with surrounding highlands (Fig. 5.1). As a consequence of collisions of the Indian and Eurasian continental plates that was initiated 40 million years ago, this area has a complex geological structure and tectonics (Molnar & Tapponnier, 1978). The SE QTP constitutes a series of grand mountain ranges including the central and eastern Nyainqentanglha ranges and mountains

in the east end of the Himalayas and west end of the Hengduan Mountains (Fig. 5.1). The high-relief terrain is characterized by standing peaks alternating with deep canyons, and the elevation ranges from hundreds of meters to more than 7000 m above sea level (a.s.l.). The mountain ranges generally ascend from the east and south bordering of the plateau to form the especially high altitude inner plateau in the northeast. Over these mountain ranges, maritime or temperate glaciers are densely presented and provide important water supply for two major rivers in Asia: the Yarlung Tsangpo and the Salween. The main Nyainqentanglha Mountains ridges is a water divide of the two drainage basins (Fig. 5.1). Most of the glacierized region in this area drains into the Yarlung Tsangpo directly or through tributaries.

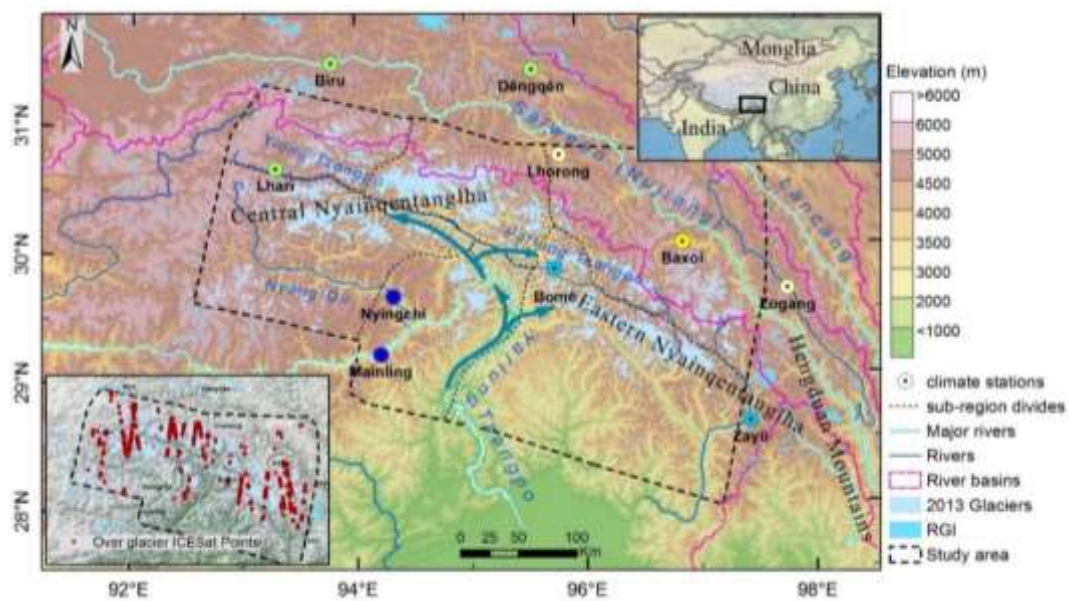


Fig. 5.1 Overview of the SE QTP, location of the climate stations (circles) and ICESat data coverage. Different color fill in circles represent different local climate characteristics according to Table 5.1. The colour-coded elevation is based on 90 m SRTM data. Glacier outlines within the study region are based on new glacier inventory compiled from 2013 Landsat 8 images. Blue lines with direction indicate the path of moisture transportation of the Indian Summer Monsoon.

The SE QTP region is affected by continental climate of central Asia and the Asian summer monsoon systems, and the latter bring the majority of annual precipitation to the area. In wet (warm) seasons (May. ~ Oct.), eastern winds dominate and the summer monsoon brings ample rainfall; in dry (cold) seasons (Nov. ~ Apr.), western winds prevail and there

is little precipitation (Su & Shi, 2002). The monsoons bring moisture to the inner plateau, following the path of the great canyons including the north-south extending Yarlung Tsangpo canyon and east-west extending of the Parlung and Yiong Tsangpo (Fig. 5.1).

Table 5.1 Annual mean temperature and precipitation totals at the 10 stations around the study area. Values are based on the period of 1992-2013.

Name	Elevation (m)	Temperature(°C)	Precipitation (mm)	group_code
Dengqen	3873.0	3.7	649	1
Biru	3940.0	3.8	601	1
Lhari	4488.8	-0.3	734	1
Lhorong	3640.0	6.0	417	2
Zogang	3780.0	4.7	451	2
Baxoi	3260.0	10.9	262	3
Zayu	2327.6	12.1	789	4
Bome	2736.0	9.0	890	4
Mainling	2950.0	8.8	709	5
Nyingchi	2991.8	9.1	691	5

Assumption on the climate conditions over the glacierized region and the regional differences can be made by analyzing data from the 10 meteorological stations as shown in Fig. 5.1. Data at these stations demonstrate strong seasonality in temperature and precipitation (Fig. 5.2). About 60%-90% of the annual precipitation concentrates in the warm season. According to seasonal precipitation patterns and the level of annual mean temperature, the regional climate can be grouped into five types (Table 5.1, Fig. 5.1). These groups depict distinctive climate features in the southeastern sides (divided by the Yiong Tsangpo and the Parlung Tsangpo) compared to those in the northwestern sides. In the northwestern sides, regional climate shows typical continental and alpine features, with annual precipitation totals increasing with rising altitudes and an inverse gradient of temperature. In contrast, the annual precipitation totals at the four stations in the southeast (Mainling, Nyingchi, Bome, and Zayu) are exceptionally high, despite of low elevations (below 3000 m), indicating relatively maritime climate due to the strong influences of the ISM. In particular, maximum annual precipitation (over 750 mm) are observed in the southern side of eastern Nyainqentanglha ranges (Bome and Zayu), and the annual precipitation cycle shows a unique two-peak pattern (Fig. 5.2). In contrast, in the northern

side of the mountain, minimum annual precipitation (262 mm) is observed (Baxoi). According to the vertical increase in precipitation and decrease in temperature (based on the six stations with elevation above 3000 m) and, the annual mean temperature and precipitation at an elevation of 5000m is estimated to be -5.6 °C and 990 mm respectively.

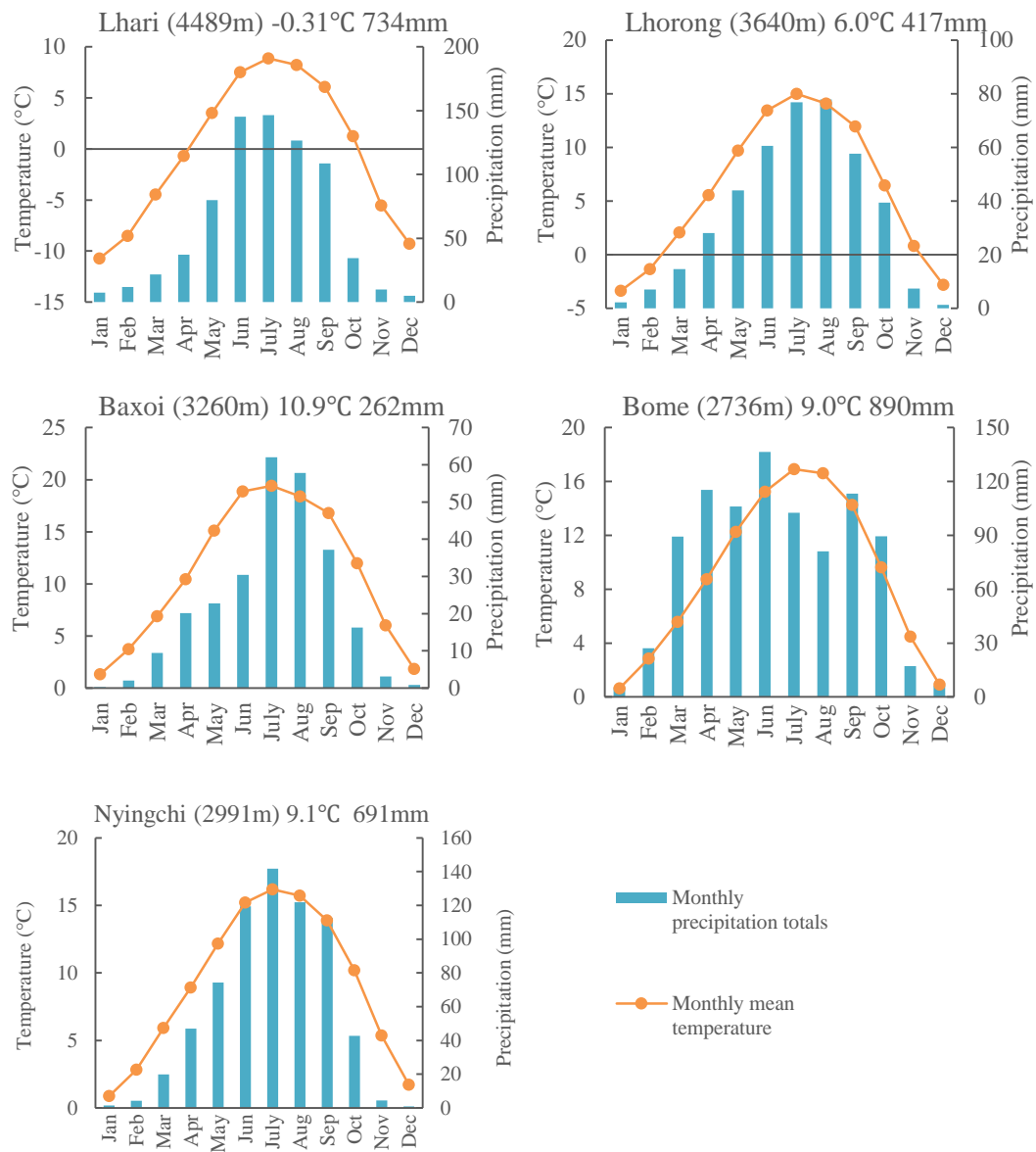


Fig. 5.2 Climate diagrams showing five typical climate characteristics at five weather stations. The statistics is based on the period of 1992-2013.

The glacier ELAs in this region were estimated to be 4600-4900 m a.s.l., increasing from south to north (Yao et al., 2012, Shi et al., 2010, Ageta & Kadota, 1992). The debris-covered glaciers are developed along the flat bottoms of valleys among the high mountain

ranges. Within the summer-precipitation climate, glaciers in the SE QTP are characterized by simultaneously maximum accumulation and ablation in the summer season. These glaciers can be highly sensitive to warming climate which can not only accelerate thinning at the ablation area but also reduce superimposed ice by suppressing snow fall at the high accumulation area (Fujita & Ageta, 2000, Fujita, 2008, Bolch et al., 2010b).

5.3. Data and methods

5.3.1. ICESat data and glacier thickness changes

As introduced in chapter 4, this study uses level-2 ICESat data. The June laser periods (2C, 3C, 3F) and Laser periods in 2009 (2E and 2F) are excluded from the analysis as they only exist in a small part of ICESat's ground tracks and have very few measurements on the glaciers. Conversion of the ICESat ellipsoid height to orthometric height, extraction of SRTM values at the footprint, and filtering of elevation difference (dh) between ICESat and SRTM DEM are performed according to section 4.3.2 in Chapter 4. The new generated glacier inventory is used to classify ICESat footprints into over-glacier and off-glacier points. Trends of elevation changes are estimated through robust regression of all dh values in autumn seasons (October/November), winter (March/April) seasons and the combined multi-season data during 2003-2008. Trends over the debris-covered parts and clean-ice parts are separately estimated.

To explore trends of elevation changes over different glacierized region, the study region is divided into six sub-regions according to the climatic similarity and glacier characteristics (chapter 3, Fig. 5.1). For each sub-region, trends are separately estimated for the accumulation areas and ablation areas according to ELA estimates in chapter 3 and Table 3.2. A more detailed elevation changes are analyzed based on the spatial cluster of ICESat measurements within nearly non-overlapping circular areas of 20 km×20 km. To derive a sound statistical analysis, trends are only calculated for the circular areas with sufficient ICESat sampling (at least five laser periods spanning more than 4 years and with

at least 10 points in each period). The glacier mass balances are estimated based on the areal data from the new glacier inventory and the ICESat-derived elevation changes with the equation (4-5).

For the whole SE QTP, the glacier thickness changes within each year can be estimated by subtracting the mean elevation difference (dh) of winter season from that of autumn season ($dh_{autumn} - dh_{winter}$). The estimated annual thickness changes reflect annual net mass balances of glaciers which can be closely associated with climate conditions in the year.

The dh values derived by linear extrapolation of the trends back to the SRTM acquisition date of February 2000 reflect the elevation offsets between ICESat and SRTM. The offsets are probably caused by penetration of SRTM into snow/ice (Kääb et al., 2012), and thus reflect a coarse estimation of SRTM penetration. The offset should to be in a reasonable range for a justified trend. Quantitatively, the errors of surface elevation trends were computed are given by:

$$e_{trend} = \sqrt{\sigma_{trend}^2 + trend_{off-gla}^2 + e_{bias}} \quad (5-1)$$

where e_{trend} is the error from the robust fitting and $trend_{off-gla}$ is the off-glacier dh trends which were calculated in the same way as the on-glacier trend. Following Gardner et al., 2013 and Neckel et al., 2014, this study included an inter-campaign bias of 0.06 m a^{-1} (e_{bias}). For the error computation of mass balances, an error of $\pm 60 \text{ kg m}^{-3}$ in ice density was added. The significance of elevation trends were indicated by the p value in the robust trend fitting. All trends with $p < 0.05$ were assumed to be significant at the 5% level.

5.3.2. GRACE data and regional mass variations

The latest Release-05 gridded GRACE data were provided by Center for Space Research (CSR) at the University of Texas (<http://grace.jpl.nasa.gov/data/>). Compared to earlier products, this release is much less noisy which shows a ~40% reduction in uncertainty compared with previous release (Long et al., 2013). Spatial smoothing was also applied to reduce stripping noises in large degrees (Xavier et al., 2010, Bettadpur, 2012). This

GRACE product has been corrected for glacial isostatic adjustment (the solid Earth's response to last deglaciation) based on the model from Geruo et al., 2013. Monthly GRACE-observed mass anomaly time series are used over the SETP between 2003 and 2011. The missing GRACE data in two months (06/2003 and 01/2011) were filled by linear interpolation based on values of the last and next months (Ramillien et al., 2006). The gridded data is provided in WGS 84 geographic coordinate at a spatial resolution of one degree. The mass budget (mm a^{-1}) at each pixel, representing total gain/lost mass (equivalent to water) averaged in the grid, was estimated with a linear fitting of the monthly time-series mass anomaly.

5.3.3. Climate data and climate change analysis

To investigate the relationship between local climatic variations and glacier changes, long-term changes in temperature and precipitation were analyzed using climate information recorded at the ten meteorological stations (Fig. 5.1 Fig. 5.1 Overview of the SE QTP, location of the climate stations (circles) and ICESat data coverage.). Some stations only have records since 1992, thus the studying period focus on 1992-2013. Monthly temperature data derived from the China Meteorological Data Sharing Service System (CMDSSS) are aggregated into annual average (November of previous year-October, hydrological year), dry season average (also cold season: November of previous year - April), and wet season average (also warm season: May-October). Precipitation data were summed instead of averaged over the same time periods.

The mean temperature (precipitation) changes for the study region is calculated by averaging temperature (precipitation) anomalies measured at the ten stations. For each year, the anomaly at each station is calculated by subtraction of the multi-year mean value (1992-2013) from the climatic variable. The anomaly represents comparable measurements of climate change among different stations where the level of temperature and precipitation varies. For each station, the rate of temperate changes are estimated by linear regression of temperature values with the year. The changes of precipitation totals during 2003-2013 for

each station are evaluated by referring to precipitation totals during 1992-2002, using the equation:

$$P_{prcp} = \frac{Prcp_2 - Prcp_1}{Prcp_1} \quad (5-2)$$

where $Prcp_2$ (mm) and $Prcp_1$ (mm) respectively represent the average annual precipitation totals during 2003-2013 and that during 1992-2002. The relative precipitation changes P_{prcp} (%) reflects the percentage of precipitation changes during the latest 11-year period compared to that in the previous 11-year period, and positive (negative) values denote increasing (decreasing) precipitation totals.

5.4. Results

5.4.1. Glacier surface elevation changes over 2003-2008

Surface elevation changes and mass balances of the study glaciers are analyzed at three spatial scales: all glacierized region, sub-region trends and trends in 20km × 20 km circles. The overall trends on the glaciers were calculated based on autumn data, winter data and the combined multi-season data (Table 5.2). Trends on the clean ice area, debris-covered parts were also separately estimated, and are all statistically significant (Table 5.2, Fig. 5.3).

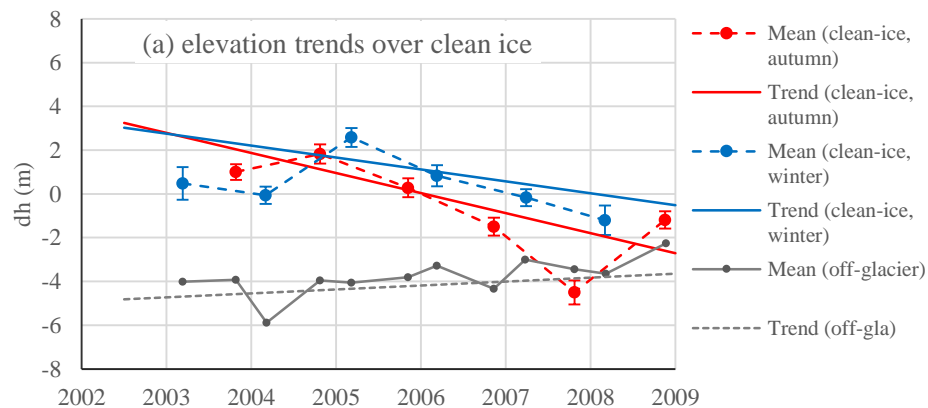
Both the autumn- and winter-based trends reveal more serious surface lowering over the debris-covered ice ($-1.13 \pm 0.32 \text{ m a}^{-1}$, autumn data) than that over the clean-ice areas ($-0.92 \pm 0.17 \text{ m a}^{-1}$, autumn data), which may be attributable to the relatively low altitude of debris-covered tongues. Over the debris-covered parts, autumn trend and winter trend were similar, while over the clean-ice areas, the autumn trend was significantly more negative than the winter trend, indicating more serious mass loss of clean ice in autumn seasons (Fig. 5.3). However, the detected seasonal differences over the clean-ice areas may be influenced by seasonal snow cover. For example, one ICESat laser period crossed the glacier surface just after a heavy snow fall, the measured elevation would be higher than that measured

after or before the snow fall. Although ICESat operated in similar dates of the winter season, the time of snow fall could vary year from year. On the other hand, the large standard errors (se) in estimated winter trends indicate relatively large uncertainties due to smaller number of measurements than that in autumn season (Table 5.2). To reduce uncertainties associated with winter data, the following analyses are based on results of the autumn season observations.

Table 5.2 Glacier elevation changes in SE QTP and mass balances for the clean ice area, debris-covered parts and the whole glacier areas.

Statistically significant trends are illustrated as bold numbers.

	On-glacier	On clean-ice	On debris	off-glacier area
Area (km ²)	6576.2	6044.5	531.7	
Number of ICESat footprints (Multi-season)	6543	6213	330	55893
Number of ICESat footprints (Autumn)	3781	3603	178	32143
Number of ICESat footprints (Winter)	2762	2610	152	23750
Elevation difference trends (m a ⁻¹)				
Multi-season	-0.75±0.20	-0.78±0.20	-1.19±0.30	0.18±0.11
Autumn data	-0.84±0.17	-0.92±0.17	-1.13±0.32	0.14±0.09
Winter data	-0.59±0.25	-0.55±0.25	-1.22±0.47	0.23±0.14
Mass balance (m w.e.a ⁻¹)				
Autumn data	-0.72±0.20	-0.78±0.20	-0.96±0.34	
Mass balance (Gt a ⁻¹)				
Autumn data	-4.71±1.30	-4.71±1.22	-0.51±0.18	



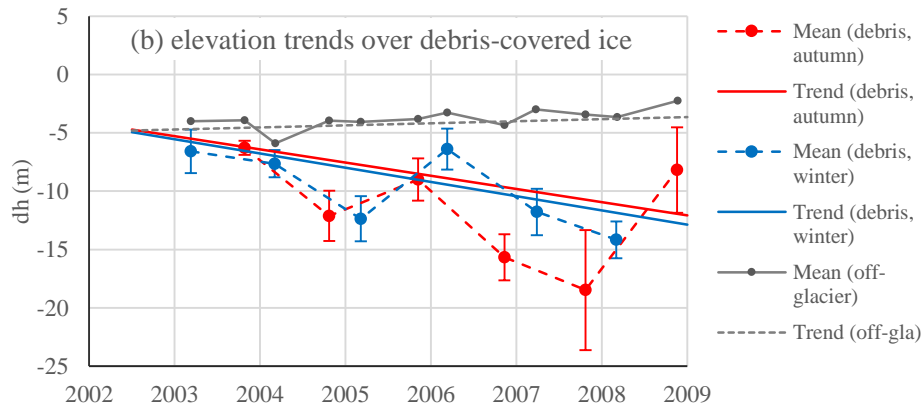


Fig. 5.3 Mean elevation difference between ICESat and SRTM (dh) for each laser period and the trends over the clean-ice parts (a) and debris-covered parts (b). Autumn (winter) trends are estimated through robust fitting of all dh values in the autumn (winter) season.

The thickness changes of glaciers show considerable differences among sub-regions of the SE QTP (Table 5.3, Fig. 5.4). All trends in the sub-regions are significant except that in the sub-region D due to a very small number of ICESat measurements (Table 5.3), therefore the following analysis focuses on the other five sub-regions. The highest mass loss is found in Sub-region F ($-1.05 \pm 0.36 \text{ m w.e.a}^{-1}$) and E ($-0.98 \pm 0.32 \text{ m w.e.a}^{-1}$) located in the eastern end of Nyainqentanglha ranges, and sub-region A ($-0.86 \pm 0.26 \text{ m w.e.a}^{-1}$) in the northwestern Nyainqentanglha ranges. In contrast, the central and southern Nyainqentanglha ranges (sub-region B and C) experienced slower mass loss ($-0.38 \pm 0.27 \text{ m w.e.a}^{-1}$ and $-0.46 \pm 0.22 \text{ m w.e.a}^{-1}$ respectively). Elevation trends calculated in a total of twenty cells well confirmed the spatial hereogeneity (Fig. 5.5). About three-quarters of the trends calculated in the circles are significant, and they reveal strong glacier thinning in the eastern and northwestern parts at rates over -1.0 m a^{-1} , and moderate thinning in the central parts ($-0.8 \sim -0.5 \text{ m a}^{-1}$). Insignificant trends are mostly in the range of $-0.4 \sim -0.3 \text{ m a}^{-1}$ with relatively large se and distributed in the margin of the study region (Fig. 5.5).

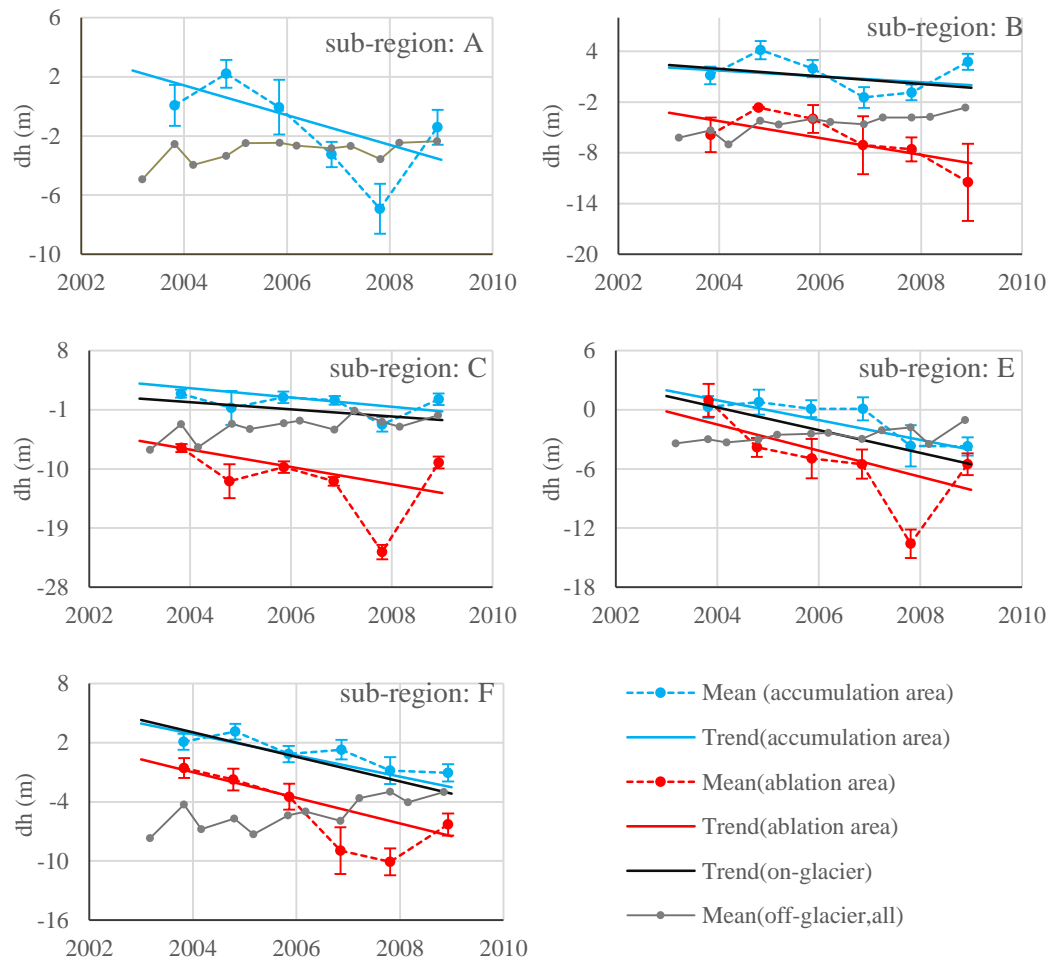


Fig. 5.4 Mean elevation difference (dh) and estimated trends for selected sub-regions of the SE QTP. For on-glacier areas, trends are shown separately for the accumulation and ablation areas as well as for the whole glacier area. For clarity only the mean dh of each laser period is shown. All trends are based on data in autumn seasons.

The dh trends over the accumulation and ablation areas were separately calculated for each sub-region except sub-region D (Table 5.3, Fig. 5.4). No data are available in the ablation area of sub-region A. The four sub-regions all showed consistent and strong surface lowering over the ablation areas, in particularly in sub-regions C, E, and F (about -1.3 m a^{-1}). Thinning trend over the ablation areas of sub-region B (-1.0 m a^{-1}), with a less significance level (90%), was slightly slower than that of other sub-regions. Compared to the low-lying ablation areas, thinning over the accumulation areas were less serious and showed relatively high spatial variability. Glaciers in the eastern sub-regions (E and F) and sub-region A experienced comparable rate of thinning (larger than 1.0 m a^{-1}) over the accumulation areas, whereas thinning over the accumulation areas in sub-region B and C

is not as fast as that of their ablation counterparts. In particular, low rate of surface lowering ($-0.35 \pm 0.19 \text{ m a}^{-1}$) is observed over the accumulation areas of sub-region B, despite that the trend is not statistically significant. Overall, glacier thinning over sub-region B and C was less serious than that over sub-region E and F, particularly at the high altitude accumulation area.

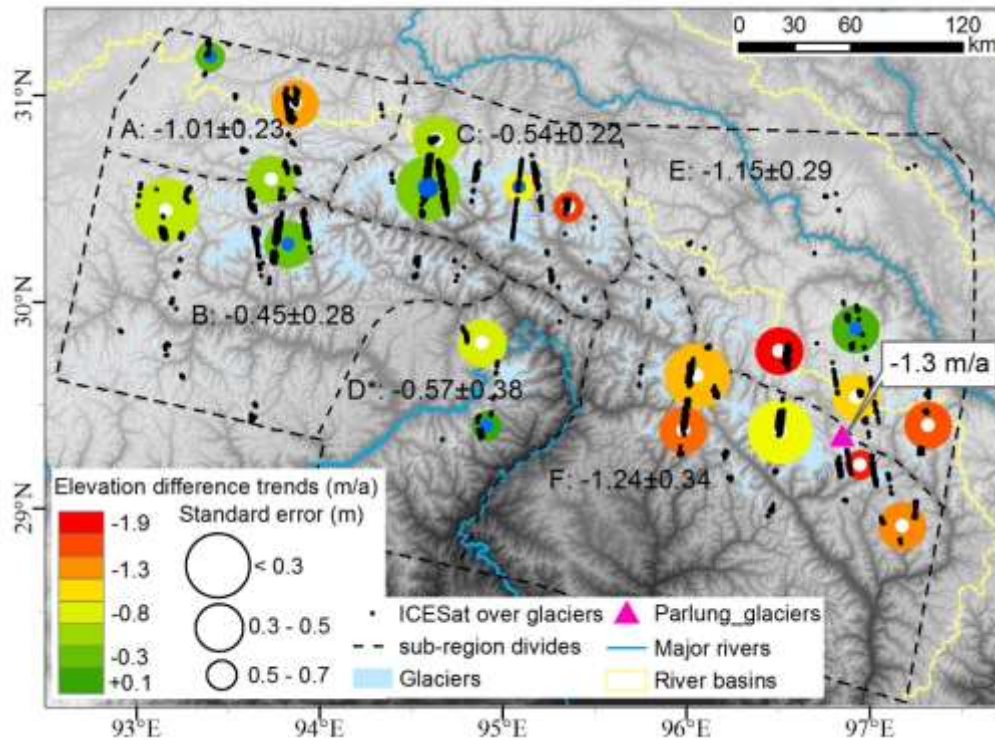


Fig. 5.5 Trends of elevation differences between ICESat and SRTM, for each sub-region and individual cells in the SE QTP, in comparison to in situ mass balance measurements of the Parlung glaciers ($-1.1 \text{ m w.e.a}^{-1}$ equivalent to -1.3 m a^{-1}).

Data are shown on dots (white centers) with trends calculated on circular geographic cells of $20 \text{ km} \times 20 \text{ km}$. Only cells with sufficient ICESat data coverage (at least total 40 footprints spanning four years) are shown. All trends are based on autumn acquisitions. Insignificant trends are indicated with blue centers. The mean trends for each subregion are given in m a^{-1} . Trend in sub-regions are all significant except sub-region D (marked with *) due to too few measurements.

In summary, considerable mass loss is observed for glaciers in the SE QTP during the year 2003-2008, particularly in the southeastern parts and over the ablation areas. The linear thinning rate derived from overall fitting of all autumn data is $-0.84 \pm 0.17 \text{ m a}^{-1}$, consistent with the area-weighted mean thinning rate ($-0.80 \pm 0.28 \text{ m a}^{-1}$). As the latter estimate have large uncertainty in the sub-region D, the former estimate based on all data is assumed to

be more accurate in this study. With a total area of 6566 km² based on 2013 glacier inventory and an average ice density of 850 kg m⁻³, this study estimated a total mass loss of 4.71±1.30 Gt a⁻¹ for the SE QTP glaciers during 2003-2008. All lost mass were drained to the Indian Ocean through streaming to the Yarlung Tsangpo and the Salween River, contributing to sea level rise of 0.012±0.005 mm a⁻¹.

Table 5.3 Statistics of glacier area, the number of ICESat measurements, and trends of glacier elevation changes and mass balances over 2003-2008 for selected sub-regions.

All trends are based on autumn acquisitions. Statistically significant trends are shown as bold numbers.

Sub-region	ICESat Number	Area (km ²)	dh trend (m a ⁻¹)				mass balance (m w.e. a ⁻¹)	mass balance (gt a ⁻¹)
			accumulation area	ablation area	on-glacier	off-glacier		
A	450	333	-1.01±0.23	-	-1.01±0.23^a	0.02±0.05	-0.86±0.26	-0.29±0.09
B	722	1459	-0.35±0.19	-1.00±0.42	-0.45±0.28	0.21±0.14	-0.38±0.27	-0.56±0.39
C	1090	1907	-0.71±0.26	-1.33±0.34	-0.54±0.22	-0.15±0.11	-0.46±0.22	-0.87±0.41
E	403	752	-1.01±0.29	-1.32±0.39	-1.15±0.29	0.20±0.13	-0.98±0.32	-0.74±0.24
F	1016	1740	-1.08±0.26	-1.30±0.33	-1.24±0.34	0.26±0.15	-1.05±0.36	-1.84±0.63
D ^b	100	383	-	-	-0.57±0.38	-0.07±0.14	-0.48±0.35	-0.19±0.14

a Data only available in the accumulation areas.

b trends over the accumulation\ablation area not determined due to too few measurements.

5.4.2. Climate change over the SE QTP during 1992-2013

The temperature anomaly averaged at the ten stations reveals striking warming trend over the SE QTP during 1992 and 2013 (Fig. 5.6a, b). The mean temperature in the warm season and cold season both increased at an unexpected high rate over 0.4 °C per decade, more than twice the rate of the global temperature change (0.2°C per decade) during 1976 and 2005 (Hansen et al., 2006). During the study period, the amount of precipitation showed marked inter-decadal variations, which is different from the stable and linear rising trend of temperature. It is obvious that the amount of precipitation totals dropped to a significantly low level after 2004 (Fig. 5.6c). Specifically, mean precipitation totals in warm season over 2003-2013 is 42 mm less than that over 1992-2002. The precipitation totals in the cold season showed large inter-annual variations and no obvious trend was observed (Fig. 5.6d).

The warming climate and low level of summer precipitation in the recent decade is probably responsible for widespread glacier thinning over the region.

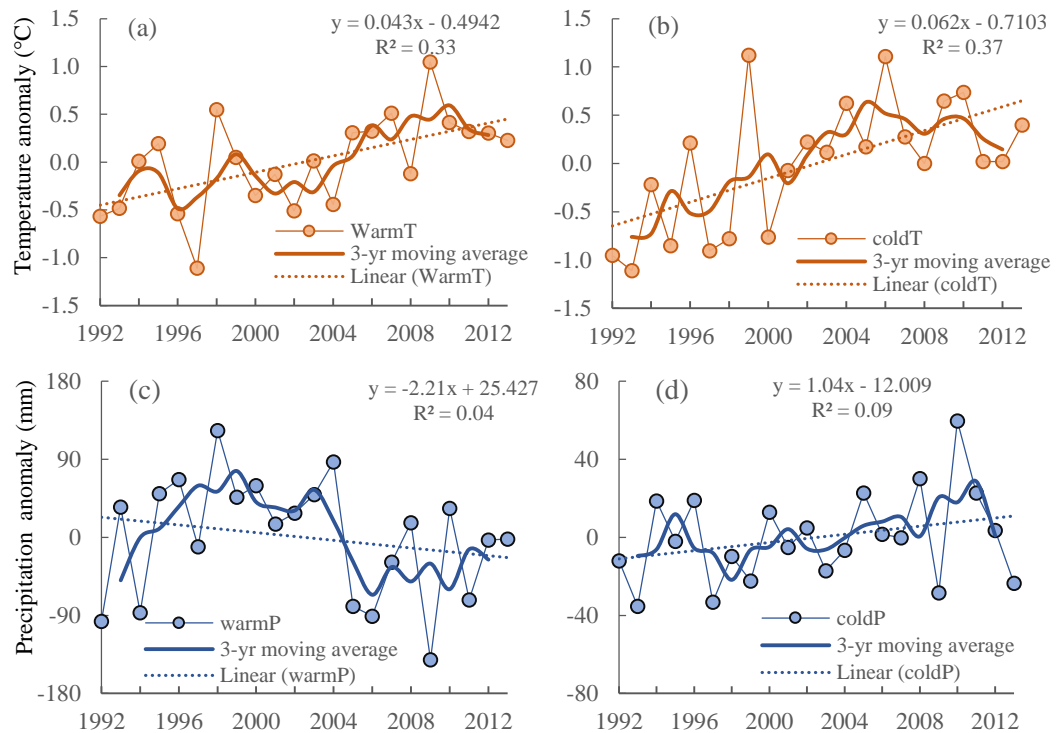


Fig. 5.6 Time-series and linear fitting of mean anomalies of climatic variables: (a) the mean summer temperature, (b) mean winter temperature, (c) mean summer precipitation, (d) mean winter precipitation.

A detailed examination of climatic variables at each station reveals spatial variability of climate change, particularly the variation of precipitation totals in warm seasons (Fig. 5.7). The mean summer temperature all exhibited fast increase over 1992-2013, at linear rates ranging from 0.36 ~ 0.53 °C per decade. Summer precipitation totals generally decreased over 2003-2013 and there are high heterogeneity among different stations (Fig. 5.7). Compared to the mean amount of summer precipitation during 1992-2002, the mean amount during 2003-2013 decreased by over 10% at stations in the southeast, including these stations around sub-region D, E and F; whereas an 10% increment was observed at Biru in the northwest and slight increase or decrease of precipitation in the middle parts (Lhari and Dengqen). Despite of limited number of stations, a general pattern from decreasing precipitation in the southeast transferring to increasing precipitation in the

northwest is obvious (Fig. 5.7).

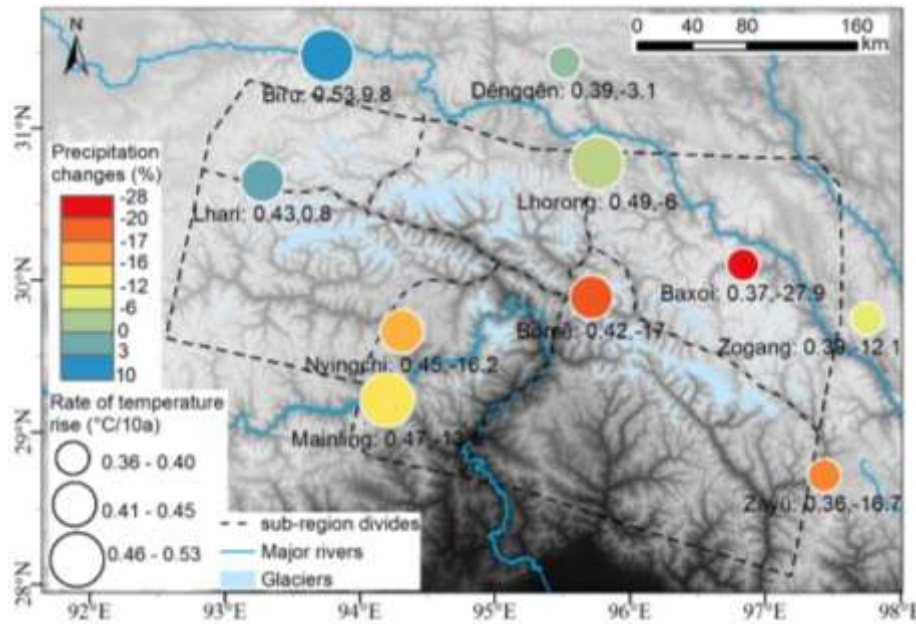


Fig. 5.7 Changes of temperature and precipitation in warm seasons over 1992-2013, measured at the ten stations.

Rate of temperature is a linear fitting of the time-series data, while the relative precipitation changes are given by comparing the mean values averaged over 2003-2013 and that over 1992-2002.

5.4.3. Analysis of climate forcing on the glacier mass balances

For the whole SE QTP, the mean annual thickness changes, which represent annual net mass balances, show significant correlation with variations of temperature and precipitation totals, with correlation coefficients reaching -0.96 and 0.80 respectively (Fig. 5.8). The most remarkable net mass loss in 2006 and 2007 (thinned over 2 m) is attributable to high level of temperature and low precipitation totals in the warm seasons, while in 2004 glaciers gained net mass due to below-normal temperature and above-normal precipitation. Overall, the variation of temperature is dominant on glacier mass balances compared to that of the precipitation. A linear fitting between glacier thickness changes and temperature anomaly (Fig. 5.9) reveals that an average increase of 1°C in warm season will lead to loss of 5.7 m ice averaged on the glacierized region.

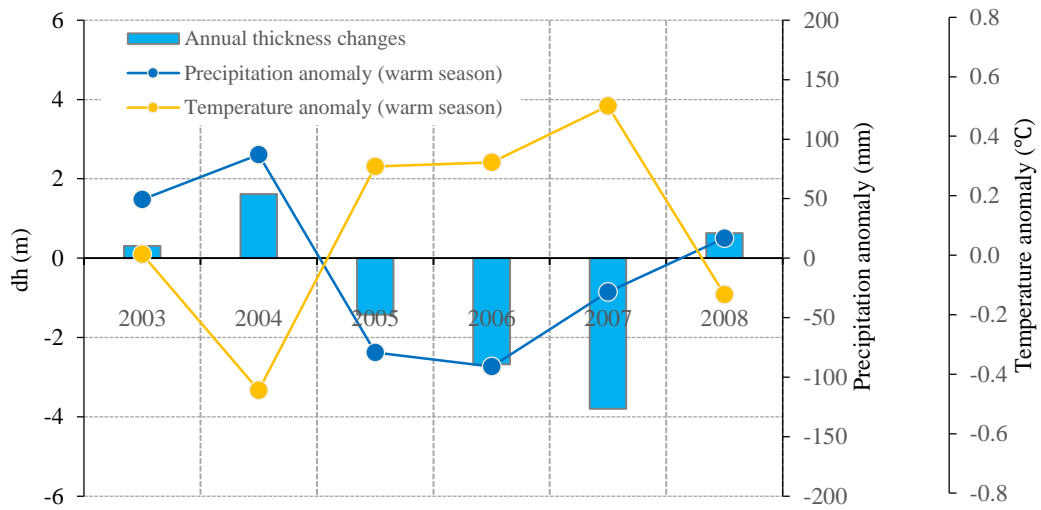


Fig. 5.8 Mean annual glacier thickness changes in the SE QTP in relation to mean summer temperature anomaly and summer precipitation anomaly.

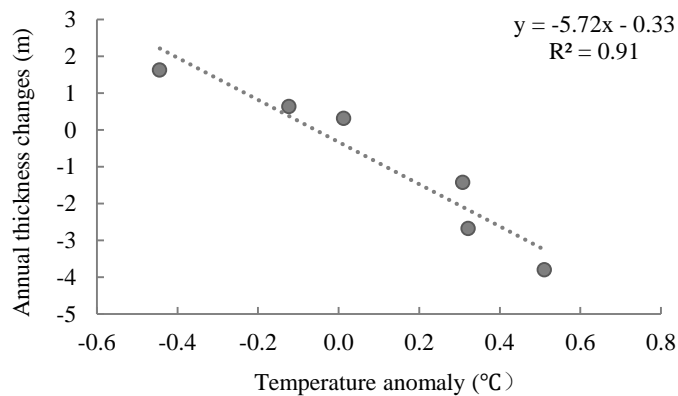


Fig. 5.9 Linear fitting of mean annual glacier thickness changes in the SE QTP with respect to summer temperature anomaly.

Although the drastic rising temperature probably induced the strong glacier thinning over the SE QTP, the precipitation changes may significantly contributed to varying thinning rates across different sub-regions and aggravated the thinning condition in some regions. In comparison with the sub-regions in the northwest (B and C), the three sub-regions in the southeast (E, F and D) experienced the most evident mass loss, particularly over the accumulation areas. This difference in thinning rates among the accumulation areas coincides well with the spatially heterogeneous pattern of precipitation changes, which showed remarkably reduced level of precipitation in the southeast in comparison with stable or raised level in the northwest during 2003-2013 (Fig. 5.7). As monsoon precipitation is directly related to accumulation over the upper altitudes, the remarkable

reduction probably explains the exceptionally strong surface lowering over the high-altitude accumulation areas in the three southeast sub-regions. Most dramatic decrease of precipitation (27.9%) is found at Baxoi where most negative glacier mass balance is observed (Fig. 5.5). These patterns indicate that precipitation changes contributed to the spatial heterogeneity of glacier thinning rates within the SE QTP.

Note that Fig. 5.9 reveals a significant inverse relationship between the variations of temperature and precipitation. High temperature were generally accompanied by low level of precipitation over 2003-2008. Such inverse relationship is obvious (correlation coefficient -0.80) during the recent decade (2003-2013) (Fig. 5.6). The characteristics of climate change in the SE QTP is especially unfavorable for the development of glaciers, which explained the marked mass loss in the past decade, and posed shades on the fate of glaciers under the scenario of global warming.

5.5. Discussion

5.5.1. ICESat-based glacier changes

Uncertainties about the ICESat-based elevation trends for mountain glaciers lie in two main aspects: 1) noise of the elevation differences between ICESat and SRTM and 2) robustness of the statistical analysis and representativeness of ICESat sampling. Over an extensive region, it is difficult to distinguish real elevation changes from noises without true validation data, given that the potential glacier variations (dh) can reach up to tens of meters. However, with statistically sufficient data, the reliability of ICESat data for determining mountain glacier changes is verified in recent studies (Kääb et al., 2012, Gardner et al., 2013, Neckel et al., 2014). Hence the minimum spatial scale of elevation trends that can be revealed by ICESat depends on the density of ICESat measurements over the glacierized region. Because of the relatively sparse sampling of ICESat data over the small-size glaciers over the SE QTP, analysis of elevation changes of individual glaciers seems not feasible. Nevertheless, analysis on regional and sub-regional scale is possible. In each sub-

region of the SE QTP (except sub-region D), the distribution of ICESat footprints is in good agreement with the glacier hypsometry (Fig. 5.10), and the number of measurements used for each trend is relatively sufficient (Table 5.3). Compared to adequately sampled ICESat measurements over the clean-ice parts, the number of measurements over the debris-covered ice is limited (Fig. 5.11), which makes detailed analysis on debris-covered ice in each sub-region unreliable.

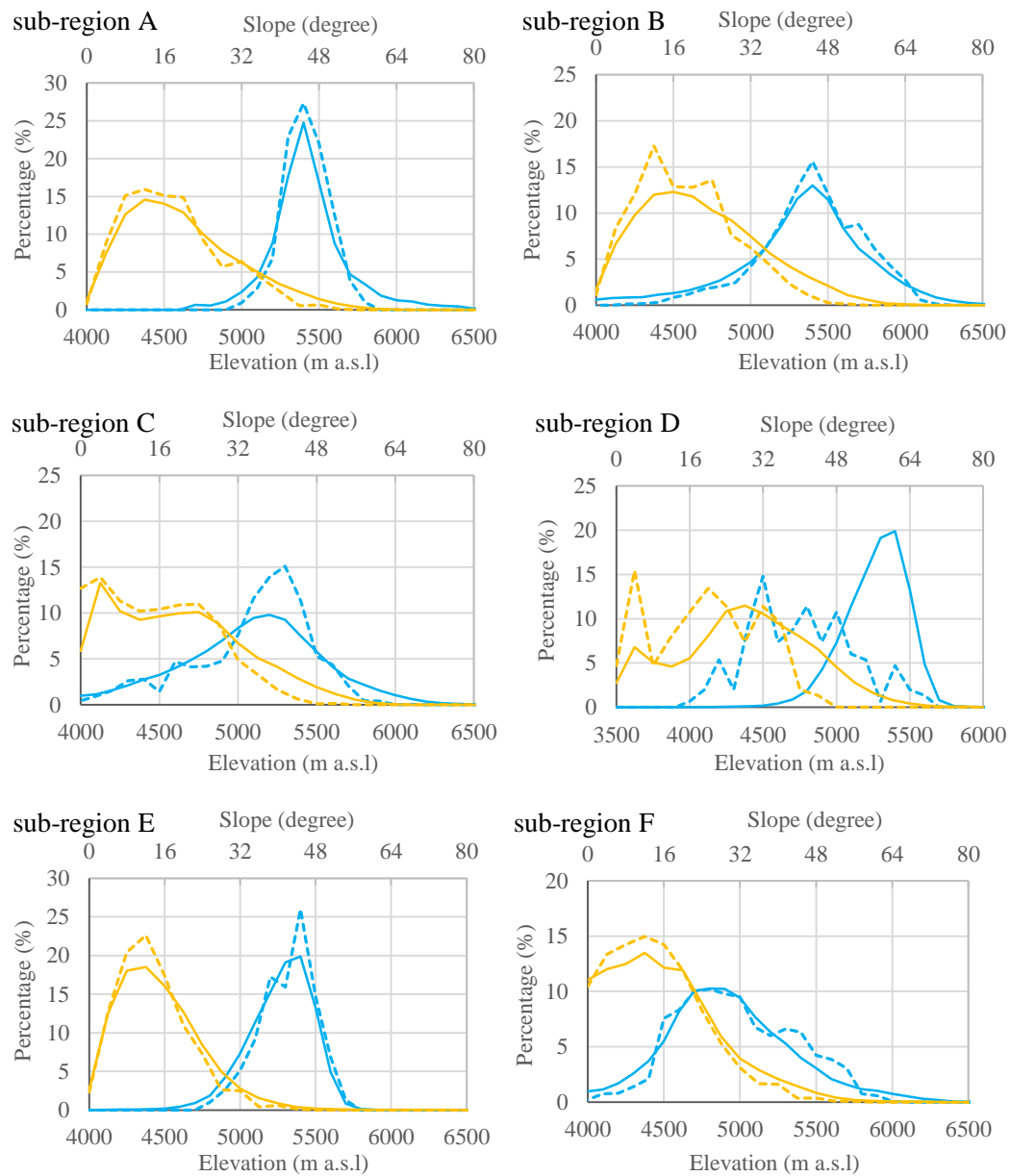


Fig. 5.10 ICESat footprint distribution in each sub-region (A, B, C, D, E and F). The elevation histograms (blue lines) and slope histograms (yellow lines) are compared between the ICESat footprints (dashed lines) and glacier masks (solid lines) in each sub-region.

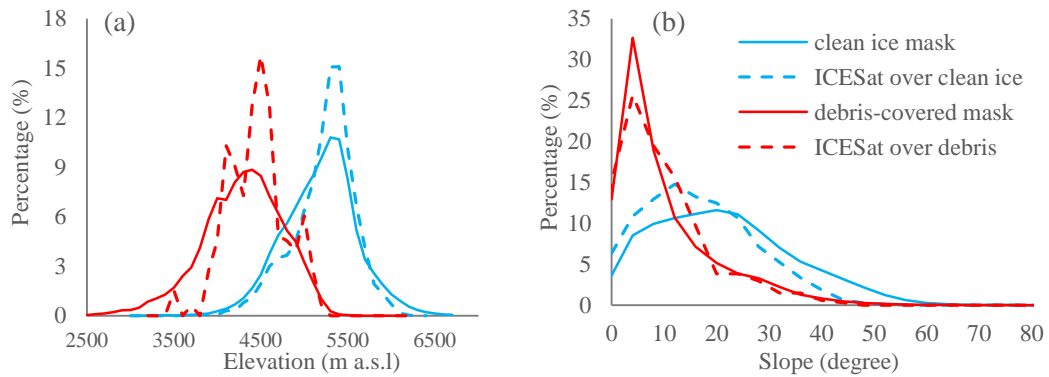


Fig. 5.11 ICESat footprint distribution over the clean ice and debris-covered in terms of elevation (a) and slope (b).

The glacier surface elevation changes estimated in this study ($-0.84 \pm 0.17 \text{ m a}^{-1}$) is close to the estimate in Neckel et al. (2014) ($-0.81 \pm 0.32 \text{ m a}^{-1}$), but are more negative than the result in Gardner et al. (2013). In the latter study, the use of problematic glacier inventory for classifying the on-glacier ICESat footprints can lead to inclusion of considerable non-glacier measurements, which may explain the less negative glacier mass balances. Compared to the former study which manually included on-glacier ICESat observations based on Landsat images, this study gave more details on the glacier changes based on a comprehensive glacier inventory. For example, this study found more strong surface lowering on the debris-covered ice ($-1.13 \pm 0.32 \text{ m a}^{-1}$) which are absent in previous studies due to no information on debris-covered glaciers. Furthermore, the spatial variability of glacier changes within the SE QTP is revealed, with separate estimates in different parts (accumulation/ablation area) of different sub-regions. In addition, with update on the total glacierized area in the SE QTP, a considerably less negative total glacier mass balances ($-4.71 \pm 1.30 \text{ Gt a}^{-1}$) with reduced error is derived, compared to that based on RGI which overestimated glacier area ($-8.3 \pm 4.73 \text{ Gt a}^{-1}$ in Neckel et al. (2014)). The fine-scale glacier changes are consistent with in-situ mass balances observed over the Parlung glaciers ($-1.1 \text{ m w.e.a}^{-1}$, 2005–2010, Yao et al 2012) (Fig. 5.5). Note that the glacier mass balances in the SE QTP is the most negative compared to glaciers changes in other QTP regions (Kääb et al., 2012, Gardner et al., 2013, Gardelle et al., 2013, Neckel et al., 2014).

5.5.2. GRACE observations

The spatial pattern of mass change trends measured by GRACE in the SE QTP and the surroundings between 2003 and 2009 is shown in Fig. 5.12. The map reveals remarkable mass loss over the SE QTP and the surrounding regions, with mass budgets below -10 mm a^{-1} . In particular, the center of mass loss is concentrated around glaciers in the southeastern part of the SE QTP ($29^\circ - 30^\circ \text{ N}$, $95^\circ - 98^\circ \text{ E}$), which corresponds to sub-region F where strongest thinning is observed. This spatial pattern indicates that the GRACE TWS decreases over 2003-2009 were likely linked to glacier mass losses in the SE QTP. There are 20 pixels covering the study region in the gridded GRACE TWS image (Fig. 5.12) and they reveal mass change rates in the range of $-20.3 \sim -11.7 \text{ mm a}^{-1}$, with a mean value of -17.1 mm a^{-1} .

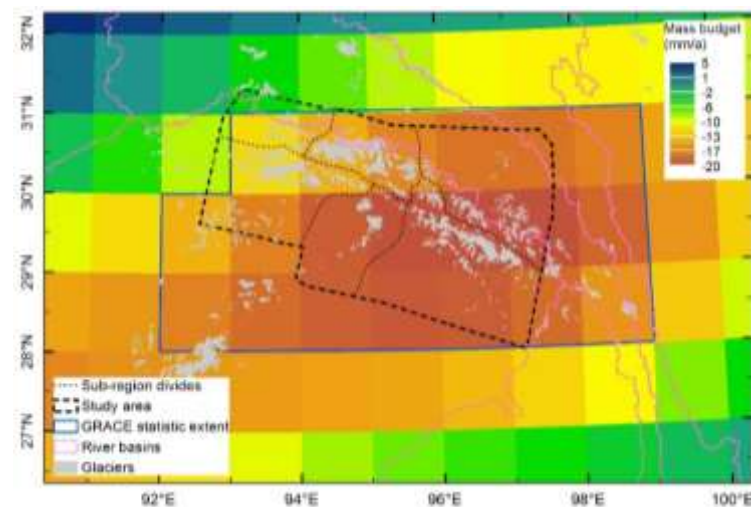


Fig. 5.12 Spatial pattern of mass budgets between 2003 and 2009 in the SE QTP derived from the GRACE gravimetry observations.

In terms of temporal variations, the monthly mass anomaly from GRACE also agrees well with changes of over-glacier thickness for the period of 2003-2008 (Fig. 5.13). The remarkable glacier surface lowering in 2006 and 2007 is well shown in the regional mass loss in GRACE observations. This, together with the agreed spatial pattern, supports that there is an independent mass loss signal in the SE QTP in GRACE's observations (Song et al., 2015), and it is likely associated with glacier mass loss in the region. Regarding the

quantitative estimates, the discrepancy between ICESat-based glacier mass changes ($-4.70 \pm 1.67 \text{ Gt a}^{-1}$) and the amount of regional mass loss estimated from GRACE data ($-3.68 \pm 0.94 \text{ Gt a}^{-1}$) may result from uncertainties of both measurements, particularly GRACE-based estimates which are affected by other mass redistributions such as geological uplifts, glacial isostatic adjustment, ongoing surface erosion and groundwater recharges (Li et al., 2008, Jacob et al., 2012), and data processing problems including signal leakage and smoothing. To derive reliable glacier mass balance estimates from GRACE data, special processing techniques of GRACE signal is probably required to reduce these influences.

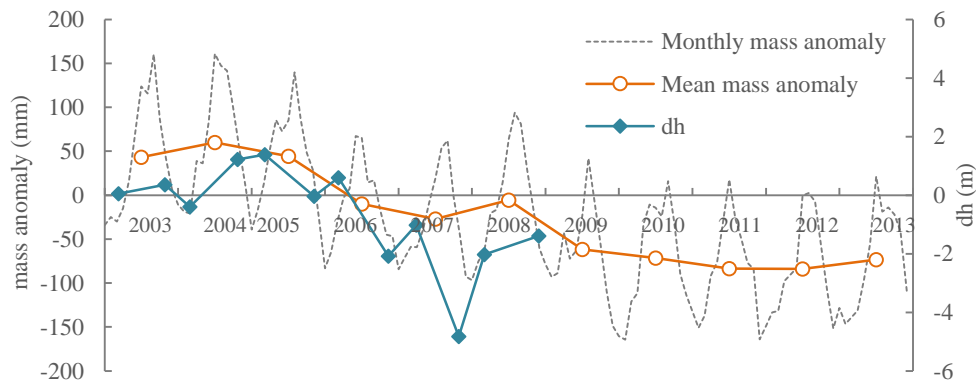


Fig. 5.13 Comparison of over-glacier thickness changes (mean dh) with the regional mass anomaly from GRACE observations.

The yellow line with unfilled dots shows the changes of annual monthly anomaly in each year.

5.6. Conclusions

Glacier mass balances and the relationship with climate in the SE QTP is analyzed in the past decade, based on ICESat elevation measurements, GRACE data and meteorological records at weather stations. The ICESat data reveal remarkable glacier thinning in the region over 2003-2009, with overall mass loss at about $4.71 \pm 1.30 \text{ Gt a}^{-1}$ ($0.012 \pm 0.005 \text{ mm}$ sea level rise). Slightly rapid thinning has been found over the debris-covered ice ($-1.13 \pm 0.32 \text{ m a}^{-1}$) than that of the clean-ice parts ($-0.92 \pm 0.17 \text{ m a}^{-1}$), probably due to the low-lying of debris-covered tongues. Spatial variability in thinning rates, ranging from -1.3

m a^{-1} to -0.3 m a^{-1} was found over different sub-regions and the accumulation/ablation areas. Generally, the southeastern part of the region (eastern end of the Nyainqentanglha ranges) showed strongest signal of glacier mass loss, particularly over the accumulation areas. This spatial variability of mass loss, and the inter-annual changes of mean glacier elevations, were well represented in GRACE-derived regional mass budgets and time series of monthly mass anomalies. Although GRACE-based estimate is within the uncertainty range of ICESat-based result, the discrepancy indicate uncertainties of GRACE-based mass changes. For GRACE observations, the coarse spatial resolution, signal leakage and reduction, and more importantly, interpretation of other geophysical contributors such as river or groundwater discharge, makes it challenging for a direct convert from regional mass anomaly to glacier mass balances.

Analysis on the local temperature and precipitation changes reveals dramatic rise of temperature accompanied by considerable decrease in precipitation in the past decade (2003-2013), which probably explained the strong glacier mass loss signal in the SE QTP, particularly during 2005-2007. Meteorological observations at ten stations showed obvious differences in precipitation changes in warm seasons, and this may be mainly responsible for the spatial variability of glacier thinning rates in this region. Specifically, the most remarkable decrease of precipitation in the southeastern Nyainqentanglha ranges could have significantly aggravated the status of glacier thinning. Overall, mean temperature in warm season showed most significant impact on the net annual glacier mass balance, and an average increase of 1°C in warm season will lead to thinning of 5.7 m ice in the glacierized region. Under the scenario of warming trend, numerous small glaciers in the region might vanish, and the severe glacier mass loss will have significant impact on the environment in many aspects.

Chapter 6

Glacier-climate interactions in the DKMD region, central QTP

6.1. Introduction

In the context of climate change in recent decades, many studies reported high spatial variability of glacier changes (Kääb et al., 2012, Gardner et al., 2013, Neckel et al., 2014). The spatial variability of glacier changes was believed to be associated with the differences in precipitation variations over the monsoon dominated southeast and westerlies dominated northwest (Yao et al., 2012). However, over the mid-latitude central QTP where three major atmospheric circulation systems intersect (westerlies, the Indian summer monsoon (ISM) and the East Asian Summer Monsoon (EASM)) (Tian et al., 2007), the controlling factors (temperature, precipitation and the seasonality) of recent glacier changes and the driving atmospheric circulations remains unclear. There are a large number of glaciers presented over the Tanggula Mountains in the mid-latitude central QTP, providing important water sources for the upstream of the Yangtze River, the longest river of China.

Investigations of the glacier-climate interaction over the plateau have been limited by inadequate observations on glacier changes. In-situ mass balance records are directly measured at stakes installed over the glacier surface (Koji *et al.*, 2000), but they are limited to a few small, low-lying and accessible glaciers and may not represent the regional variability of glacier changes. At present, increasing satellite observations allow examination of various glacier parameters (length, area, elevation and velocity) and their changes over large areas and extended time periods. Remote sensing based estimates are indirect, and mostly require some sort of ground control or validations; they however offer the practical approach of obtaining a statistically representative sampling of glacier changes (Bamber and Rivera, 2007; Racoviteanu *et al.*, 2008). In particular, images acquired from

Landsat satellite series, which has the longest observation records of the earth surfaces (from mid-1970s to present) at a medium-high resolution (30 m- 80 m), provides valuable information about the temporal evolution of glaciers.

Climate systems over the mid-latitude central QTP can be rather complex because of the potential intersection of monsoon systems and westerlies. Recent studies found that the arctic amplification can impact on the mid-latitude weather patterns and extremes (Francis & Vavrus, 2012, Screen & Simmonds, 2013) and mid-latitude westerlies may drive climate variation and glacier variability in the monsoon affected areas of High Asia (Mölg et al., 2013). On large spatial scales, climate variations over the QTP may also be tele-connected with hemispheric or global atmospheric circulations including El Niño Southern Oscillation (ENSO) and North Atlantic Oscillation (NAO) (Wang et al., 2003). ENSO have been suggested to influence climate over the southern QTP through the link of ISM (Xu et al., 2010, Xu et al., 2011), while NAO is generally believed to be associated with climate over the northern parts of QTP through modulation of westerlies (Wang et al., 2003, Zhao et al., 2012). Whether such teleconnections exist over the mid-latitude central QTP and how they affect local climate and glacier variability in the area is not well known.

With a focus on glacier changes in the DKMD region of the central QTP, this section presents the evolution of the glaciers based on time-series Landsat images. The control of the annual and seasonal climate conditions on the glacier changes will be analyzed by exploring time series of various local and large-scale climatic variables. In particular, we will discuss the possible inner links between local climate variations and large-scale atmospheric circulations including westerlies, the Indian summer monsoon and ENSO events.

6.2. Study area

The glaciers are located in the DKMD region of the Tanggula Mountains, and are

considered as typical mid-latitude sub-continental glaciers (Koji et al., 2000). The ice body consists of 32 valley or cirque glaciers, including DDG and XDG, with a total area about 118.0 km² with minimum elevation above 5000 m a.s.l. according to glacier inventory from GLIMS database (Fig. 6.1). Glaciers in this region are of semi-continental type with annual mass balance mostly dominated by accumulation and ablation in summer season (Koji et al., 2000). The glaciers lie in a climate zone which is close to the boundary between the monsoon-dominated south and the continental westerly dominated north (Chen et al., 2010). The semi-arid continental climate is characterized by a long cold season from October to April and a short warm season from May to September, and over 90% of the annual precipitation falls in the warm season as snow at high altitudes (Zhang *et al.*, 1997). According to meteorological observations at 5600 m on the XDG during 1992-1993, the annual mean air temperature and annual precipitation are -9.8 °C and 302 mm, respectively (Pu *et al.*, 2008).

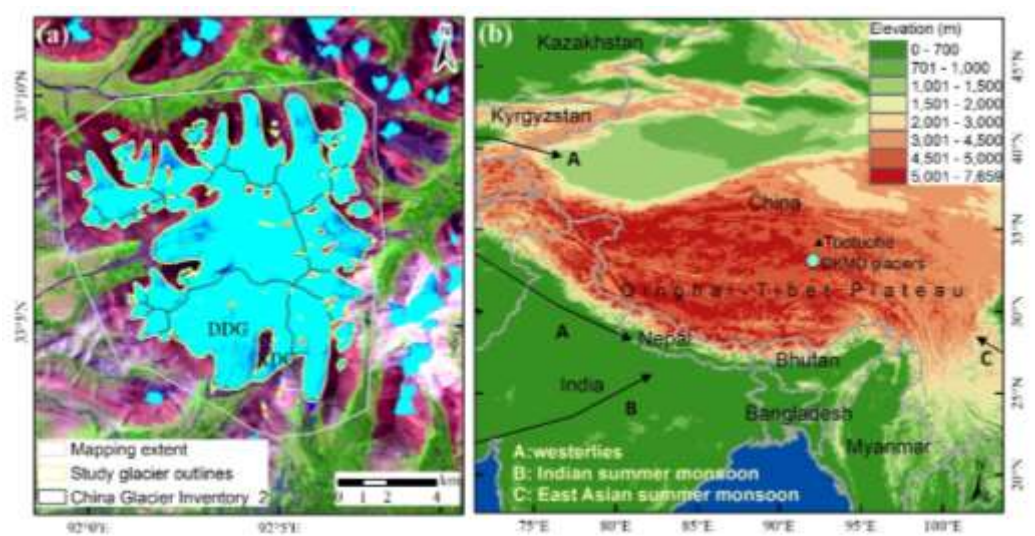


Fig. 6.1 The glaciers in the DKMD region in central Qinghai-Tibet Plateau and the influence of atmospheric circulations.

The left image shows outlines superimposed on false-colour composite of Landsat TM satellite images, bands 5 (red), 4 (green) and 2 (blue), acquired on August 30th, 2000. The right map shows the location of the glacier and Tuotuohe weather station and dominant atmospheric circulations: westerlies, Indian summer monsoon and East Asian summer monsoon.

6.3. Datasets and methods

6.3.1. Landsat images over 1976-2013

A total of 21 Landsat images sampling 18 years from 1976 to 2013 are used in the glacier mapping (Table 6.1). All images, except three acquired in 2001, 2003 and 2010 (marked in Table 6.1), are cloud-free over the glaciers. For glacier mapping over the partly cloud-covered areas, reference images (marked in Table 6.1) are used. As there are few suitable images in the 1970s and early 1980s, we also used two images (1976 and 1986) whose acquisition dates do not strictly meet the requirement but are of high-quality in other aspects (cloud free and with minimal seasonal snow cover compared to other images acquired in the same year).

Table 6.1 List of Landsat images used in this study. Images marked with • are partly cloud covered and those marked with * were used for reference

Sensor	Acquisition date (YYYY/MM/DD)	path/row	Used Bands
Landsat2/MSS	1976/11/11	148/37	4,5,6,7
Landsat5/TM	1986/07/30	138/37	2,4,5
Landsat5/TM	1988/07/28	137/37	2,4,5
Landsat5/TM	1989/09/17	137/37	2,4,5
Landsat5/TM	1990/08/19	137/37	2,4,5
Landsat5/TM	1991/09/14	138/37	2,4,5
Landsat5/TM	1992/08/31	138/37	2,4,5
Landsat5/TM	1994/08/21	138/37	2,4,5
Landsat5/TM	1995/08/17	137/37	2,4,5
Landsat5/TM	2000/08/30	137/37	2,4,5
Landsat5/TM	2001/07/23•	138/37	2,4,5
Landsat7/ETM+	2001/10/12*	137/37	2,4,5
Landsat5/TM	2003/08/07•	137/37	2,4,5
Landsat5/TM	2003/10/17*	138/37	2,4,5
Landsat5/TM	2004/09/10	137/37	2,4,5
Landsat5/TM	2007/08/02	137/37	2,4,5
Landsat5/TM	2009/08/30	138/37	2,4,5
Landsat5/TM	2010/09/02•	138/37	2,4,5
Landsat5/TM	2010/10/20*	138/37	2,4,5
Landsat5/TM	2011/08/29	137/37	2,4,5
Landsat8/OLI	2013/08/02	137/37	3,5,6

Two methods are employed to derive glacier outlines from Landsat MSS and TM data respectively. For Landsat TM images, the well-established semi-automated band ratio approach is employed to retrieve glacier area. An empirical threshold of 0.4 is applied to segment the NDSI images into glacier area and non-glacier area. To retrieve glacier area from the MSS image that has no short-wave band, we used the ISODATA unsupervised classification method that iteratively clusters pixels class using minimum distance techniques (Memarsadeghi *et al.*, 2007). In this process, the scene is firstly clipped around the glacier region, and then is classified into four classes based on all the four bands with up to four iterations. Post-classification processing is important to maintain high quality results (Paul *et al.*, 2015), and we manually correct glacier outlines due to influence of cloud cover by referring to cloud-free reference images, and check and correct misclassifications due to shadow and other disturbances. By calculating a buffer of 15 m around the glacier outlines, we roughly estimate the mapping accuracy in the range of 2.9% to 3.2%, which matched well with the uncertainty ~3% reported in previous studies (e.g. Paul *et al.*, 2002; Pieczonka and Bolch, 2015).

6.3.2. Local climatic variables and reanalysis data

To investigate the relationship between local climatic variations and glacier changes, long-term changes in temperature and precipitation are analyzed using the CN05 grid Dataset (Wu & Gao, 2013), which has been validated as accurate (You *et al.*, 2014, Shen & Xiong, 2015) and widely applied to analyze long-term climate change in China (e.g. Zhou *et al.*, 2015, Ren *et al.*, 2015). This gridded dataset, with a resolution of 0.5×0.5 degree, was constructed by interpolating climatic records of 2416 meteorological stations in China with the ‘anomaly approach’ (New *et al.*, 2000). We extracted monthly temperature and precipitation estimates over 1976-2013 from the grid where the study glaciers are located. Such estimates of precipitation (temperature) shows similar intra-annual and inter-annual pattern to that recorded at the closest meteorological station Tuotuohe (Fig. S1 and Fig. S2). According to hydrological year setting, monthly temperature data are aggregated into annual average (October to September), cold season average (winter season: October to

April), and warm season average (summer season: May to September). Precipitation data are summed over the same time periods. The strength of westerlies and the changes are evaluated with the PC-based NAO index. Summer season IMI and EASMI index are used to assess the strength of summer monsoon IM and EASM respectively. SOI index is used to evaluate the occurrence and strength of ENSO or La Nina events. This study also evaluated large-scale SLP anomalies over the NH and NP with the NAM and NPI respectively. Detailed descriptions about these indices were introduced in Chapter 2.

Linear regression analysis is performed to estimate trends of glacier area, local temperature and precipitation changes. The significance of the trends is evaluated by p value and R square of the trend fitting. Spearman's correlation coefficients are calculated to examine the relationship between glacier area and climate variables. We examine possible relationships between local climatic variables (temperature and precipitation) and atmospheric circulation indices by calculating their correlation coefficients based on detrended time series data. The detrending is conducted by subtracting the trends estimated with the linear fitting method from the original climatic data and indices (difference detrending method). The detrending processing is to mitigate spurious correlations due to potential common trends presented in the original time-series data.

6.4. Results

6.4.1. Glacier area changes over 1976-2013

There is considerable variability in glacier area, with average area of $85.0 \pm 5.6 \text{ km}^2$ ($n=18$, one standard deviation) from 1976 to 2013. The total glacier area decreased by 12.5% from 88.4 km^2 in 1976 to 77.7 km^2 in 2013, with a linear shrinking rate of $0.42 \text{ km}^2 \text{ a}^{-1}$ (equivalent to percentage decrease of $0.49\% \text{ a}^{-1}$, in relation to the multi-year average area) ($R^2=0.53$, $p<0.01$) (Fig. 6.2). Glacier shrinkage is particularly obvious since the early 1990s and has accelerated since early 2000s. In contrast to a total loss of 1.4 km^2 (1.6%) in glacier area from 1976 to 1990, the glacier area dropped by 3.4 km^2 (4%) over 1990-2001 and by 5.8

km² over 2001-2013. The rate of area reduction increased from 0.33 km² a⁻¹ ($R^2=0.56$, $p<0.01$) over 1988-2004 to 0.39 km² a⁻¹ ($R^2=0.76$, $p<0.01$) over 2000-2013. Note that in 1986 the glacier area expanded to the maximum of 102.7 km², nearly a quarter more than the multi-year mean glacier area.

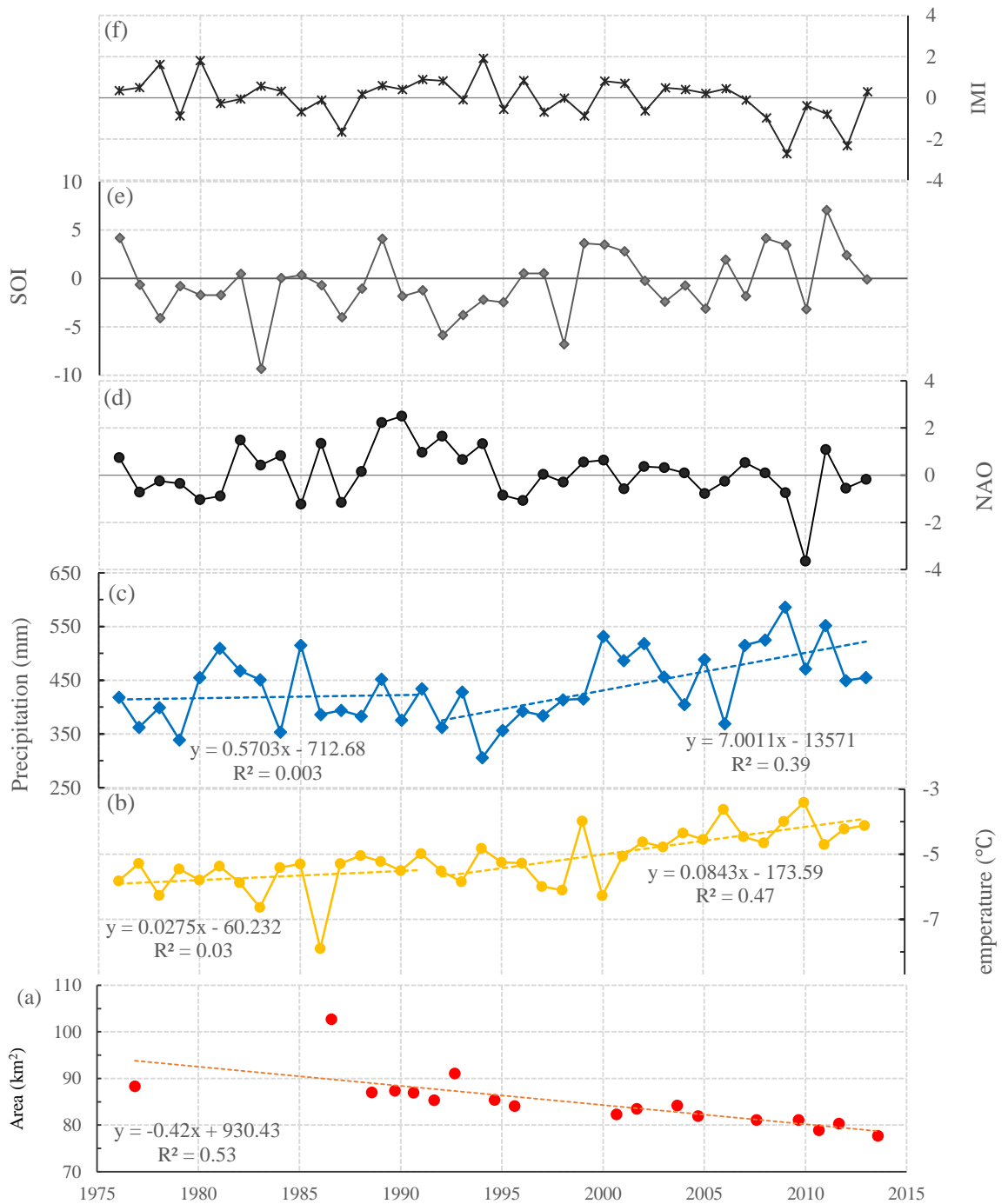


Fig. 6.2 Inter-annual variability in glacier area (a) in relation to temperature (b), precipitation (c), winter Southern Oscillation Index (SOI) (e), North Atlantic Oscillation (NAO) (d), and Indian Monsoon Index (IMI) (f) over 1976-2013.

6.4.2. Long-term variation of temperature and precipitation

The annual temperature increased at a linear rate of 0.53°C per decade over 1976–2013 ($R^2=0.44$, $p<0.01$) (Fig. 6.2), much higher than global warming trend of 0.15°C – 0.20° per decade that began in the late 1970s (Hansen *et al.*, 2010). The annual precipitation totals increased at a linear rate about 26 mm per decade. A detailed analysis of the time-series temperature and precipitation data reveal that significant increasing trend of temperature and precipitation began in the early 1990s, by comparing the almost flat trends for the period of 1976–1991 with the remarkable increasing trends for the period 1991–2013 (Fig. 6.2). Summer precipitation totals followed a similar variation to that of annual precipitation. Precipitation in winter fluctuated around an average level of 42.5 mm, except in year 1986 and 2000 when extremely high amounts of precipitation were observed.

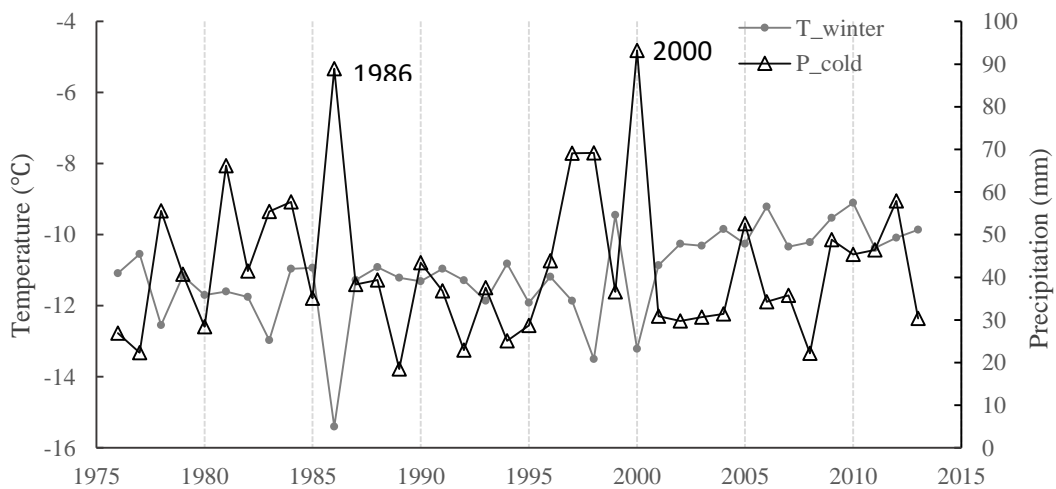


Fig. 6.3 Time-series variation in winter mean temperature (T_{winter}) and winter total precipitation totals (P_{winter}) between 1976 and 2013.

The time-series winter temperature and precipitation data in Fig. 6.3 reveal two extreme climate events in 1986 and 2000 respectively. In these two years, winter precipitation reached high extremes and correspondingly the winter temperature dropped to the lowest. In 1986 the winter temperature dropped to -15.4°C , about 8°C lower than the multi-year average; and the amount of precipitation peaked at 88.9 mm, more than twice the long-term average. The abnormally cold winter in 1986 has been documented as large-scale snow

storm events in the central QTP (Tang *et al.*, 1998).

6.4.3. Relationship between glacier variation and climate variables

Table 6.2 shows the Spearman correlation coefficients between glacier area and climate variables. Given the extreme local climate conditions in 1986 and 2000, the statistics are divided into two groups: group I based on all 18 samples and group II based on the 16 normal cases excluding year 1986 and 2000. In the two groups, the annual mean temperature shows the most significant relationship with glacier area with correlation coefficients being over 0.85 ($p < 0.01$). The winter temperature seems to be more dominant than the summer temperature, although their impacts are comparable in normal years. Note that in normal years the precipitation totals produced negative correlations with the glacier area (group II). The linear relationship between the glacier area and the annual temperature is shown in Fig. 6.4, which indicates an increase of 1°C in annual temperature can contribute to loss of 5.1 km² in glacier area at a high confidence level ($R^2 = 0.73$, $p < 0.01$).

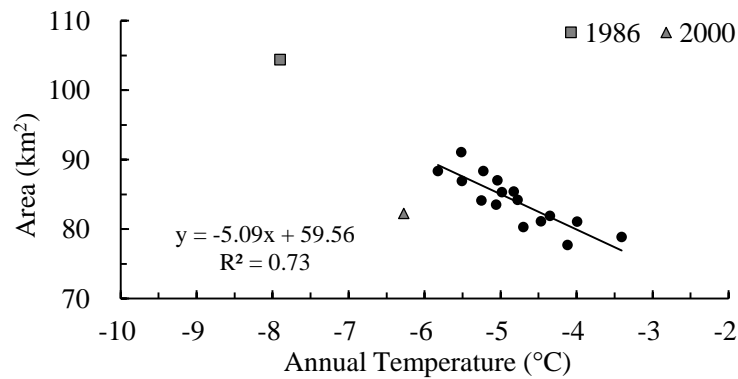


Fig. 6.4 The relationship between glacier area and annual temperature in the DKMD region. The linear regression is based on normal cases (dots) and the two abnormal years 1986 (square) and 2000 (triangle) are not included.

Table 6.2 Correlation between glacier area and climate variables.

Group I is statistics based on all area samples and group II is based on those excluding two extreme climate years. Result in bold are significant at the 0.01 level and those in italics at 0.05.

Climate parameter and season	Group I: Glacier area (n=18)		Group II: Glacier area (excluding 1986 and 2000, n=16)	
	Correlation coefficient	p-value	Correlation coefficient	p-value
Temperature				
Annual	-0.86	0.00	-0.86	0.00
Summer	-0.61	0.01	-0.71	0.00
Winter	-0.80	0.00	-0.76	0.00
Precipitation				
Annual	<i>-0.49</i>	0.04	<i>-0.58</i>	0.02
Summer	-0.60	0.01	<i>-0.54</i>	0.03
Winter	0.30	0.22	<i>-0.53</i>	0.03
NAO				
Annual	<i>0.50</i>	0.04	0.63	0.01
Summer	0.30	0.22	0.46	0.07
Winter	0.37	0.13	0.77	0.00
SOI				
Annual	-0.36	0.14	-0.43	0.10
Summer	-0.27	0.28	-0.35	0.18
Winter	-0.16	0.52	-0.17	0.52
NAM	-0.24	0.33	-0.70	0.00
NPI	<i>-0.50</i>	0.04	-0.09	0.74
IMI	0.19	0.45	<i>0.52</i>	0.04
EASMI	0.26	0.30	0.17	0.53

The inter-annual variation of glacier thickness changes in recent years was closely connected with variation of annual temperature, as shown in Fig. 6.5. The glaciers thinned correspondingly as the annual temperature increased in 2004 and 2006. The considerable thinning in 2006 was probably caused by significant increase of annual temperature (0.9°C) coupled with decrease of summer precipitation (101mm) than the previous year.

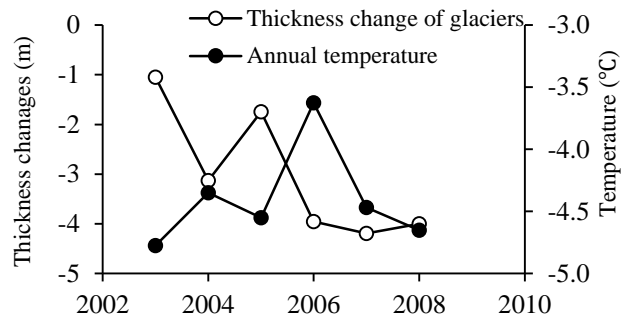


Fig. 6.5 The relationship between average thickness changes and the annual temperature (a) and winter precipitation (b) between 2003 and 2008

6.4.4. Correlations between climate variables

Further analysis reveals interesting relationships between the climate variables over 1976-2013 (Table 6.3). First, there are positive relationships ($p < 0.05$) between the annual temperature and the summer precipitation, which reveals a coupled warming and wetting trend of the local climate. Second, the variation of local climate variables show close association with different large-scale atmospheric circulations, the most significant being NAO and SOI (Table 6.3). The summer temperature produces significantly negative relationship with annual NAO, and the winter temperature is negatively connected with winter NAO and SOI. The variation of (annual) summer precipitation totals is inversely related to summer NAO. Note that the summer precipitation totals show no significant relation with IMI and EASMI. Fig. 6.6 shows the three-year running average of NAO in relation to the summer temperature and precipitation, and SOI in relation to the winter temperature and precipitation. We can note out-of-phase relationship between the variation of NAO and local climate variables, particularly for the period of 1991-2013, with correlation coefficients reaching -0.80 ($p < 0.01$) for precipitation-NAO and -0.69 ($p < 0.01$) for temperature-NAO. The SOI-precipitation relationship shifted from significant out-of-phase ($R = 0.54$, $p < 0.05$) during the period of 1976-1990 to subtle in-phase after 1991.

NAO and SOI are also found to be related to other climate variables. Winter NAO is closely correlated with NAM ($p < 0.01$), and summer NAO shows significant positive relationship with IMI. The positive IMI-NAO relationship confirms that the intensity of Indian summer

monsoon is more impacted by oscillation at Atlantic sea rather than the Pacific Ocean in recent decades (Chang et al., 2001, Goswami et al., 2006). Relationships were also found between SOI and other climate variables. The status of SOI is closely linked with NPI, especially in winter seasons. The significant inverse EASMI-SOI relationship supports an enhanced link between intensity of summer monsoon from the Pacific Ocean and ENSO status which has been suggested in previous research (Li et al., 2010).

Table 6.3 Correlation matrix of relationships between climate variables after de-trending the original time series data.

The statistics is based on 36-year samples over 1976-2013 (excluding abnormal years of 1986 and 2000). Results in bold are significant at the 0.01 level and those in italics at 0.05.

	Temperature			Precipitation			NAO			SOI			NAM	NPI	ISM	EA SMI
	Ann.	Sum.	Win.	Ann.	Sum.	Win.	Ann.	Sum.	Win.	Ann.	Sum.	Win.				
Temp																
Ann.	1.00															
Sum.	0.48	1.00														
Win.	0.93	0.21	1.00													
Prcp.																
Ann.	-0.07	-0.17	-0.04	1.00												
Sum.	0.01	-0.21	0.06	0.97	1.00											
Win.	-0.19	0.13	-0.28	0.04	-0.14	1.00										
NAO																
Ann.	-0.24	<i>-0.34</i>	-0.15	-0.09	-0.06	-0.22	1.00									
Sum.	0.17	0.19	0.11	<i>-0.40</i>	<i>-0.38</i>	-0.14	0.23	1.00								
Win.	-0.32	-0.18	<i>-0.34</i>	-0.06	-0.02	-0.10	0.60	0.15	1.00							
SOI																
Ann.	<i>0.33</i>	-0.04	<i>0.33</i>	0.23	0.27	-0.10	-0.06	-0.01	-0.19	1.00						
Sum.	0.01	0.27	-0.09	0.12	0.10	0.23	-0.21	0.11	-0.17	0.45	1.00					
Win.	0.27	-0.21	<i>0.35</i>	0.25	0.28	-0.18	0.11	-0.07	-0.09	0.85	-0.03	1.00				
NAM	<i>0.36</i>	0.26	<i>0.34</i>	-0.02	-0.07	0.16	-0.66	-0.08	-0.95	0.20	0.23	0.06	1.00			
NPI	0.30	0.06	0.25	0.09	0.13	-0.21	<i>0.35</i>	0.06	0.16	0.46	-0.17	0.56	-0.23	1.00		
ISM	-0.17	0.02	-0.15	-0.20	-0.19	-0.27	0.18	<i>0.37</i>	-0.12	-0.24	0.05	-0.31	0.15	-0.18	1.00	
EAS MI	0.21	-0.10	0.24	-0.10	-0.10	0.18	0.18	0.09	0.14	0.05	-0.45	0.32	-0.15	0.31	-0.22	1.00

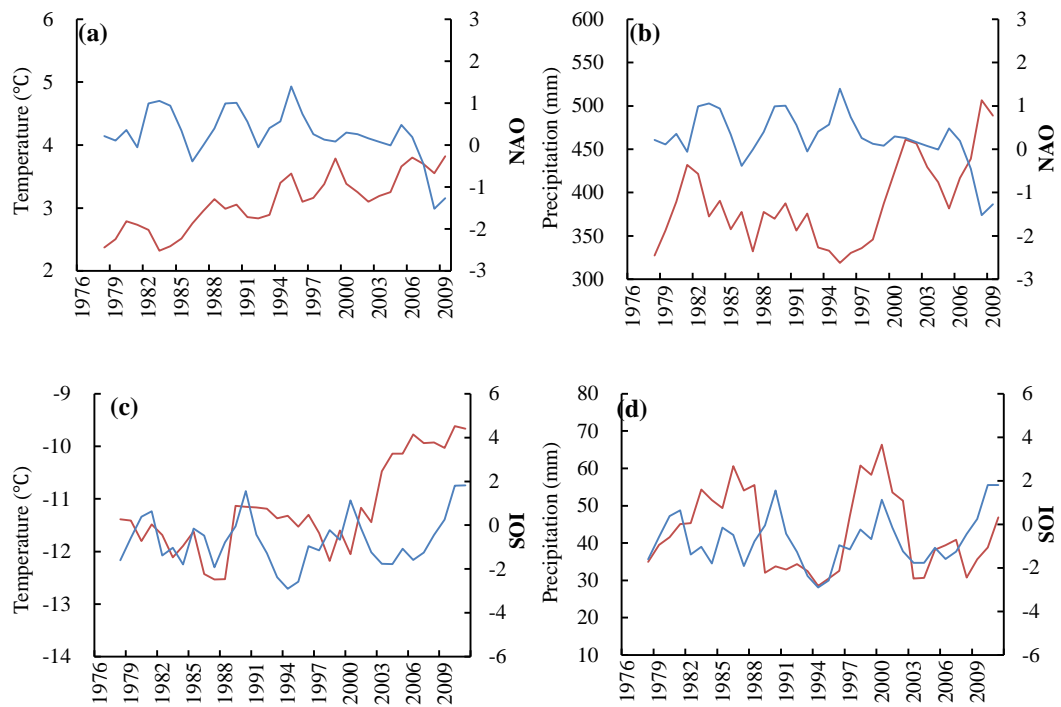


Fig. 6.6 Three-year moving averages of time-series climatic variables: (a) NAO and summer temperature; (b) NAO and summer precipitation; (c) SOI and winter temperature and (d) SOI and winter precipitation.

6.5. Discussion

6.5.1. The sensitivity of glacier variations to local climate change

The above glacier-climate analysis has demonstrated that the variation of local climate has direct influence on glacier changes in the DKMD region. The close area-temperature relationship indicates that the annual temperature impact strongly on the glacier mass budgets. The negative area-precipitation relationship is somehow unexpected, as normally precipitation contributes to glacier accumulation, e.g. by providing fresh snow. A possible explanation to the results is that the effect of temperature increasing on melting overpowered the contribution of precipitation and therefore dominates the inter-annual balance of glaciers. However, compared to the drastic recession of glaciers in the southern and southeastern QTP (Yao *et al.*, 2012), the high level of precipitation in this area may have slow down the rate of glacier mass loss in the recent decade. Nevertheless, the dependence on annual temperature means that glaciers over the DKMD region will keep

suffering from severe retreat if the warming trend continues.

The snow storm events in 1986 (specifically in the October –November of 1986 according to meteorological records at Tuotuohe) resulted in glacier expansion. The considerable supplement of fresh snow over the glacier surface not only directly contributed to ice accumulation, but also can lead to an increase in surface albedo which in turn decrease the absorption of solar radiation and slow down snow melting. The two-fold effect may result in positive mass balances and glacier advance in the followed one to three years. This provides a convincing explanation for the strikingly glacier expansion in 1986. However, the glacier area in 2000 did not reach the level of 1986. There are several possible explanations. First, winter precipitation totals in 2000 is not as high as that in 1986. Second, the high temperature in 2000 summer (0.8°C more than that in 1986) had accelerated the glacier melting. Finally, the glaciers experienced a rapid shrinkage between 1986 and 2000, which may have resulted in disappearance of small glaciers. It should be pointed out that some of peripheral snow cover may be included in the glacier mapping based on the Landsat imagery, despite the fact that we selected images acquired around the end of ablation season with minimal seasonal snow cover. This can be particularly true for 1986 and 2000 as the snow cover in winter season of these years might have sustained through the melting season.

6.5.2. Potential links among glacier variation, local climate and atmospheric circulations

Variability in atmospheric circulation patterns have major influences on mean SLP, anomalous air flow, all providing forcing to local temperature and precipitation patterns. The inverse relationship between summer precipitation and IMI, and the weak relationship between summer precipitation and EASMI, suggests that summer precipitation in the DKMD regions in mid-latitude central QTP is more dominated by westerlies rather than the two monsoon systems. Furthermore, the significant inverse relationship between NAO and local climate variables indicates the oscillation in North Atlantic Ocean are tele-

connected with climate variability over the study region. A possible mechanism of this teleconnection is that with intermediate or negative strength of NAO, the westerly jet stream and associated storm tracks would shift to a southward path (Raible et al., 2007), transporting warm and moist oceanic air masses from Atlantic or Mediterranean to the mid-latitude Asia and resulting in increased local temperature and precipitation (Aizen et al., 2001, Lioubimtseva et al., 2005, Chen et al., 2010). The increasing temperature will then cause more melting of ice and may result in negative mass budgets of glaciers, considering that glaciers in this region are sensitive to summer temperature. In contrast, the positive phase of NAO can shape enhanced westerlies flowing a northern track, bringing warm and moist air masses to the northwestern region of Europe and High Asia rather than the mid-latitudes of central Asia (Aizen et al., 2001, Hurrell & Van Loon, 1997), and will favor positive mass budget of glaciers in the DKMD area.

The positive relationships between SOI and temperature, and between glacier volume and NPI, suggests potential links between Pacific-sea related atmospheric circulation and local climate and glacier variations. Previous studies suggested that SOI impacted the QTP region through the link of ISM: the ISM tends to be weak during years with strong negative SOI (ENSO events), resulting in less than normal warm and moist ocean air masses transported to the plateau, weak latent heating of monsoon precipitation and consequently low temperature (Yin et al., 2000, Wang et al., 2003, Xu et al., 2010, Xu et al., 2011). However, this ENSO-ISM link is not justifiable over regions where the influences of ISM cannot reach. Furthermore, the ENSO-ISM relationship has weakened since late 1970s, which has been supported in the SOI-ISM correlation analysis in this study and observed in previous research (e.g. Kumar et al., 1999, Chang et al., 2001).

At present it is not clear how SOI impacted temperature over the central QTP. Nevertheless, positive SOI-temperature associations were widely found over the QTP (Yin et al., 2000, Wang et al., 2003), indicating the underlying teleconnection is running on large spatial scales. We suppose such mechanism can be related with equatorial zonal Walker

circulation and tropical meridional Hadley cell at western Pacific. When SOI is in intermediate or high positive phase (normal or La Niña events), the normal or enhanced Walker Circulation can strengthen the Hadley cell at western Pacific which transports heat and moisture from the tropical western Pacific heat source ('warm-pool') to the north mid-latitudes including central QTP (Quan et al., 2004). However, when SOI is in significantly negative phase (ENSO events), the Hadley cell at western Pacific can be weakened by anomalous descending air motion in the off-equatorial western Pacific due to weakening or reversed Walker Circulation (Wang, 2002), resulting in less than normal heat transported to the north mid-latitude continents. The Hadley cell over western Pacific and SOI is most prominent in winter season due to pronounced zonal temperature gradients; therefore the influence of SOI on temperature is more significant in winter season than in summer season.

Although none of the climatic indices in this study have been identified to be directly connected with the extremely cold and snowy winters of 1986 and 2000 (Tang et al., 1998), the super El Niño events that occurred in 1983 and 1998 may be somewhat relevant. Fig.6.6 shows that summer SOI is negatively correlated with winter temperature and precipitation after smoothing with the moving three-year average, which is consistent with prior studies observing that SOI can have certain influences on snow depth over the QTP with a one or two years' time lag (Shaman & Tziperman, 2005). The mechanism is however not certain. Our observations indicate that ENSO events can contribute to mass gain of glaciers in the DKMD regions by affecting winter snowfall in the next two or three years. Such effect of SOI has also been found in other mid-latitude glaciers, such as the Tasman glacier in New Zealand (Purdie et al., 2011).

The relationship between local climate variables and NAO, SOI, however, may have varied through time (Wang et al., 2003). This study shows that in recent decades the mid-latitude central QTP is dominated by continental westerlies and the variation of glaciers showed close relationship with NAO, particularly NAO in warm seasons. The ENSO events are favorable for accumulation of glaciers by high possibility of increasing winter precipitation

in the following years. However it is worth noting that the relationship between local climate change and NAO, SOI is not always linear, and fluctuations in these atmospheric circulations cannot full explain the glacier variability. There may be other climate forcing and further research is needed to investigate which and how regional atmospheric circulations affect climate variability and glacier variations in QTP.

6.6. Conclusions

By exploring the long-term observations from Landsat satellites, this study presents areal changes of glaciers in the DKMD region in the central QTP. The results show that the examined glaciers experienced remarkable shrinkage during the past 38 years, with the total area reduced by 12.5% from 88.4 km² in 1976 to 77.7 km² in 2013. Glacier shrinkage has been particularly distinct since the early 1990s and accelerated after the early 2000s.

The variation of mountain glaciers in the DKMD region is closely associated with climate change in the past several decades. Time-series temperature and precipitation data reveal drastic increase of the annual temperature, couple with rising level of summer precipitation, began in the early 1990s. Analysis of glacier area in relation to local climatic variables reveals the annual temperature exerts strongest impact on glacier changes. However, high precipitation can contribute to significant ice accumulation and slow down ice melting, resulting in positive mass balances and glacier advance in the followed one or two years. The snow storm events that occurred in 1986 and 2000 demonstrated such positive effect. The high level of precipitation in the past decade may have slowed down glacier mass loss in the central QTP, compared to the drastic recession in the southern and southeastern QTP.

Our analysis on glacier-climate relationship and correlations between climate variables indicates that the DKMD region is dominated by continental westerly air masses instead of Indian summer monsoon in the past two decades and glacier variation has close connection with the state of NAO and SOI. The weakening NAO favors the southward shift of

westerlies and storm tracks, resulting in increase of temperature and precipitation in the mid-latitude central QTP and negative glacier mass budget. Conversely when NAO are in strongly positive phase, the westerlies keep a northern track, resulting in decreasing temperature and precipitation over the region and a more likely positive glacier balance. Super ENSO events seem to be associated with the two snow storm events occurring in 1986 and 2000, which show significant contribution to glacier advance. It is worth noting that the relationships between glacier variation and NAO and SOI are not always linear. Further research is needed to investigate which and how regional atmospheric circulations affect climate variability and glacier changes in different regions of the QTP.

Chapter 7

Heterogeneity of glacier changes in the West Kunlun

Mountain region

1.1. Introduction

A number of studies have reported glacier thinning and retreat over the QTP (Liu et al., 2003, Yao et al., 2007, Kehrwald et al., 2008, Yang et al., 2008, Bolch et al., 2012). In contrast of the widely observed negative glacier mass balances, glacier advancements and positive mass balances were observed in the northwestern plateau including central Karakoram and western Kunlun mountain (WKM) region, which are often referred to the ‘Karakoram anomaly’ (Hewitt, 2005, Yao et al., 2012, Gardelle et al., 2012, Gardelle et al., 2013). These ‘anomalies’ were believed to be partly associated with increased precipitation over the high altitude region which are significantly affected by the mid-latitude westerlies (Immerzeel et al., 2010, Bolch et al., 2012, Yao et al., 2012). However, many studies found most of the sudden advance and mass gain of glacier over these regions were associated with surging (Quincey et al., 2011, Yasuda & Furuya, 2013, Li et al., 2013, Bhambri et al., 2013). It is believed that surging is likely attributable to internal instabilities including glacier morphology, subglacial conditions and glacier beds, rather than climate change (Clarke et al., 1984, Sharp, 1988, Quincey et al., 2011, Yasuda & Furuya, 2013). Surging is thus important for understanding the glaciological processes and internal dynamics of glaciers which may not be directly driven by climate change.

Previous studies focused on the variability of glacier changes on large spatial scales (the whole plateau or continental), while at the same time they suggest the necessity of more detailed examinations of individual glacier changes in the northwestern QTP including the WKM region, to improve understanding of regional glacier dynamics. Remote sensing techniques have demonstrated the potential in such applications by providing various

glacier information. The elevation data from ICESat, in particular, can provide multi-date elevation measurements on glacier surfaces, which enables examination of glacier surface elevation changes. Based on ICESat data, recent studies estimated overall glacier mass balances over several sub-regions of the QTP by assuming homogenous conditions within each sub-region (Neckel et al., 2014, Gardner et al., 2013); however, there are limited discussions on glacier changes in the WKM region at local scales. In particular, a complete inventory of surging glaciers and surging events is not yet available for the WKM region and the mechanisms of surging are still not clear. The WKM region has the largest concentration of contemporary large mountain glaciers according to the CGI (Huang, 1995, Shen, 2004). The absence of information on individual glacier changes leaves a gap in understanding the characteristics of local glacier dynamics, and can affect quantitative assessment of overall glacier mass balances. In addition, the glacier inventory in this region provided by the GLIMS database (Raup et al., 2007), RGI (Arendt et al., 2012) and CGI (Shi et al., 2010) show serious quality issues (Pfeffer et al., 2014) , and it is necessary to update the glacier inventory for further studies.

The main objective of this section is to (1) generate a complete and up-to-date glacier inventory for the WKM region and to provide information on the general glacier characteristics with the latest Landsat data; (2) analyze glacier changes in the WKM region over 2003-2008 by exploring the ICESat elevation measurements; (3) estimating terminus changes of glaciers in the past 15 years (1998/1999-2013) and identify possible surging glaciers by using Landsat and ICESat data; and (4) discuss the characteristic, implications of detected glacier dynamics and glacier surging in the WKM region.

1.2. Study area

The WKM region refers to the broad mountainous regions in the northwestern margin of the QTP, facing the Tarim basin to the north and Karakoram to the west (Fig. 7.1). The area consists of a number of mountain ranges extending generally from west to east with average elevation ranging from 5000 m above sea level (a.s.l.) to 7000 m a.s.l.. In particular, there

is a dense distribution of glaciers among the high mountains between Aksayqin and Keriya Pass, where the Kunlun Peak (Kunlun Goddess Mt, also the main peak of the WKM range, 7167 m a.s.l.) stands at the center of the glacierized mountain area (Fig. 7.1). This study focuses on Kunlun Peak area where most of the largest glaciers over the QTP are distributed with a total area over 3000 km² (Shen, 2004).

According to the morphology, glaciers developed in this region can be classified into valley glaciers, ice caps (flat topped glaciers), and cirque glaciers. Valley glaciers are typical glaciers and are widely distributed over the rugged northern slopes, and they generally consist of several tributaries; whereas ice caps have developed over the relatively low-relief southern slopes (Shen, 2004). There are fifteen groups of great glaciers with names, including the largest ice cap in the mid-latitude area: Guliya Ice Caps and the largest mountain glaciers over the WKM range: Duofeng glacier (Fig. 7.1). The end of glacier tongues generally reach to the foothills of mountains at about 4900-5300 m (Li & Shi, 1991), and have very limited debris cover (Scherler et al., 2011). Contemporary snowline of glaciers was estimated in the range of 5900-6100 m and mean ELA was around 5930 m based on field observations (Ageta et al., 1989, Li & Shi, 1991).

Glaciers over the WKM region are polar-type glaciers (quasi-polar or extra-continental type) which developed in an extremely arid and cold climate (Huang, 1995). According to short-term in-situ records, the mean annual temperature and mean summer season temperature at the ELA (5930 m) is about -14.0 °C and -1.7 °C respectively (Zhang et al., 1989). The annual precipitation around the mean ELA (5930 m) is about 250-350 mm, with most precipitation concentrated in warm seasons (May to September) (Zhang et al., 1989, Kang & Xie, 1989). Meltwater of glaciers in the northern slope flows to the north Tarim Basin through Yurungkax and Keriya, while glaciers in the southern slope drain into closed saline lakes including Aksai Chin, Gozha Co and Bangdag Co (Fig. 7.1).



Fig. 7.1 Overview of the study area in the Western Kunlun Mountains (WKM). Glacier outlines are based on the RGI. The names of 15 well-known groups of glaciers are shown in brown (Li et al., 2013).

1.3. Data and methods

1.3.1. Mapping glacier inventory

Six Landsat 8 scenes acquired in 2013 is selected to map the latest glacier inventory (Table 7.1). Inspection of available Landsat 8/OLI scenes show that images with minimal seasonal snow cover are partly cloud-covered, mainly around the margins of glaciers. Thus three images with lowest coverage of seasonal snow and acquired in August 2013 are selected as base images, and the cloud-free images acquired in July and September of 2013 are used as references for the cloud-covered parts in the base images (Table 7.1 and Fig. 7.2). Landsat images were all systematic radiometric and geometric corrected and projected in UTM zone 44N. The pre-processing of Landsat data include generating false color composites (RGB 754 for Landsat 8/OLI) for distinguishing clouds, ice and snow.

Table 7.1 List of Landsat scenes used in the WKM region

Purpose	Satellite/Sensor	Scene date (dd/mm/yyyy)	path/row
Mapping glaciers of 2013	Base images	Landsat8/OLI	10/08/2013 145/35
		Landsat8/OLI	10/08/2013 145/36
	References image	Landsat8/OLI	01/08/2013 146/35
		Landsat8/OLI	11/09/2013 145/35
		Landsat8/OLI	11/09/2013 145/36
		Landsat8/OLI	09/07/2013 145/36
Investigation of glacier terminus changes	Terminus in the end of 1990s	Landsat7/ETM	29/09/1999 145/36
		Landsat7/ETM	13/09/1999 145/35
		Landsat5/TM	04/10/1998 145/35
	Terminus of surging glaciers	Landsat7/ETM	02/09/2001 145/35
		Landsat7/ETM	05/09/2002 145/35
		Landsat7/ETM	30/08/2002 145/35
		Landsat7/ETM	22/04/2003 145/36
		Landsat7/ETM	22/07/2003 145/35
		Landsat7/ETM	11/11/2003 145/36
		Landsat7/ETM	19/04/2004 145/36
		Landsat7/ETM	08/07/2004 145/36
		Landsat7/ETM	10/09/2004 145/36
		Landsat7/ETM	28/05/2005 145/35
		Landsat7/ETM	10/10/2006 145/35
		Landsat5/TM	10/08/2007 145/35
		Landsat5/TM	15/08/2009 145/35
		Landsat5/TM	21/10/2010 145/35
		Landsat5/TM	05/08/2011 145/35

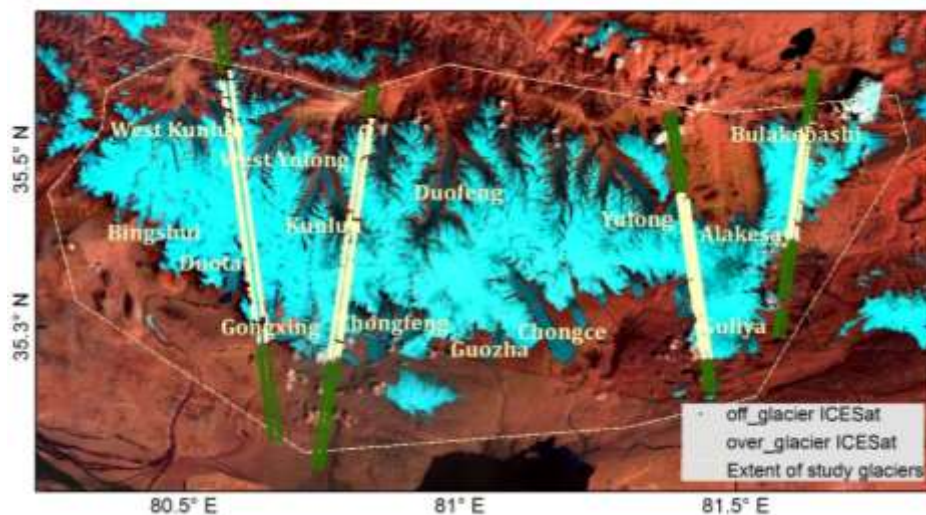


Fig. 7.2 Glaciers over the WKM on the false-color composite (RGB from Band 754) of Landsat 8/OLI images and the coverage of ICESat footprints.

Glaciers in this region have very limited debris cover (Scherler et al., 2011, Yasuda & Furuya, 2013); therefore glacier mapping only involves clean ice mapping. This study

applies the semi-automated NDSI approach to map snow /clean ice. The generation of glacier inventory is similar to that described in Chapter 3 and Chapter 4. In the post-processing stage, the derived glacier mask was smoothed with a 3×3 kernel-size median filter and modified with manual remove of erroneously classified features. The minimum size of glaciers to be included in the glacier inventory was set to 0.02 km². Generation of ice divides was firstly created by watershed analysis with the SRTM DEM, which is described in (Bolch et al., 2010), and then manually corrected by referring to the Landsat scenes. The glacier-specific parameters including topographic information (minimum, maximum, mean and median elevation, mean slope and mean aspect in degree and mean aspect sector) were calculated for each glacier.

1.3.2. Elevation trends from ICESat data

Processing of ICESat data is similar to that described in Chapter 5. In summary, all elevation differences between ICESat and SRTM DEM (dh) is filtered with a threshold of 150 m. The June laser periods (2C, 3C, 3F) and Laser periods in 2009 (2E and 2F) are excluded due to few measurements. The new glacier inventory is used as a mask to classify ICESat footprints into over-glacier and off-glacier points. As the region receives very low precipitation and mostly in summer seasons, all dh values obtained in autumn (October/November) and winter (March/April) seasons are used to estimate the inter-annual elevation trends with a robust linear fitting method. The elevation trends over individual glaciers are estimated with measurements within the glacier extent. To keep ICESat sampling over a relatively concentrated glacierized area, ICESat tracks without inter-annual repeats (some ground tracks only cover year 2003) are excluded in the analysis. The distribution of ICESat data is shown in Fig. 7.2. We group measurements over small glaciers with insufficient ICESat measurements to form one trend estimation. The spatial grouping is to guarantee that each trend is estimated with sufficient ICESat sampling (at least five laser periods spanning more than 4 years and with at least 6 points in each period). Accumulation and ablation areas are separated by the mean ELA and trends are separately estimated. Some glaciers have ICESat measurements over several separated accumulation

or ablation areas, and trends are separately calculated for the different parts if there are sufficient data. By multiplied by 0.85 (under a density assumption of 850 kg m^{-3}), elevation trends (m a^{-1}) are converted to mass balance (m w e.a^{-1}).

Detailed method for evaluating the uncertainties of ICESat data is introduced in section 5.4.1 of Chapter 5. Qualitatively, the uncertainty is assessed by the offset estimated by linear extrapolation of the trends back to the SRTM acquisition date. Quantitatively, the errors of surface elevation trends are computed according to (5-1). The significance of elevation trends is evaluated by the p value in the robust trend fitting.

1.3.3. Glacier terminus changes based on Landsat data

The length change of glaciers in the WKM region during the past 16 years (1998/1999 – 2013) is examined by comparing the position of terminus in the new glacier inventory and terminus position in the Landsat images acquired in 1998/1999 (Table 7.1). Glacier outlines in year 1999/98 are retrieved in a similar way to the generation of the glacier inventory. A coarse inspection of glacier outlines acquired in different year showed that most glaciers kept stable in the past 16 years. Thus this study further examines length changes of major glaciers which show obvious variations in terminus positions. For these glaciers, the center line along the glacier tongue is manually drawn by referring to the glacier outlines in the 2013 glacier inventory. The terminus position is then determined by intersecting the glacier outlines with the center line, and the linear distance between two terminus positions was measured as the length changes.

For glaciers showing profound changes in terminus position, this study employs more cloud-free Landsat scenes (Landsat 7/ETM or Landsat5/TM) to examine the length changes in different years since 1998/1999 (Table 7.1). As surging can occur at any time of the year, there is no limitation on the dates of acquired images. For Landsat 7/ETM images acquired after 2003, the stripes of gaps caused by failure of SLC are filled with a destripping procedure based on bilinear interpolation of neighboring pixels. This destripping process

can improve the visualization of images and has limited influence on the retrieved glacier terminus, because glaciers of interests are either with narrow stripes or free from the influence of stripes.

1.4. Results

1.4.1. Glacier distribution

The 2013 glacier inventory of the Kunlun Peak area includes 537 glaciers $> 0.02 \text{ km}^2$, covering a total area of 3137 km^2 . The distribution of glaciers by number and by area per size class and per mean aspect sector is shown in Fig. 7.3. In this region, 88% of all analyzed glaciers are smaller than 5 km^2 , but they share only 11.4% of the total area. On the other hand, the largest 7 glaciers with size over 100 km^2 cover more than 40% of the glacierized area (1254 km^2). This pattern is generally consistent with patterns of mountain glaciers in mid-latitudes (e.g. Andreassen et al., 2008, Bhambri et al., 2011, Frey et al., 2012), but the mean size of glaciers in this region (5.8 km^2) are exceptionally higher than that in Karakorum basins such as Shyok (1.4 km^2) (Bhambri et al., 2013) and western Himalayan basins (0.81 km^2) (Frey et al., 2012). The relatively large size results from a dense distribution of great glaciers in the WKM region. These glaciers, including Duofeng, Zhongfeng and Kunlun (size $> 200 \text{ km}^2$), generally consist of several tributaries from different basins, and have long tongues, diverse terrain which can span elevation ranges (the difference between the maximum and minimum elevation) as large as 1000 m.

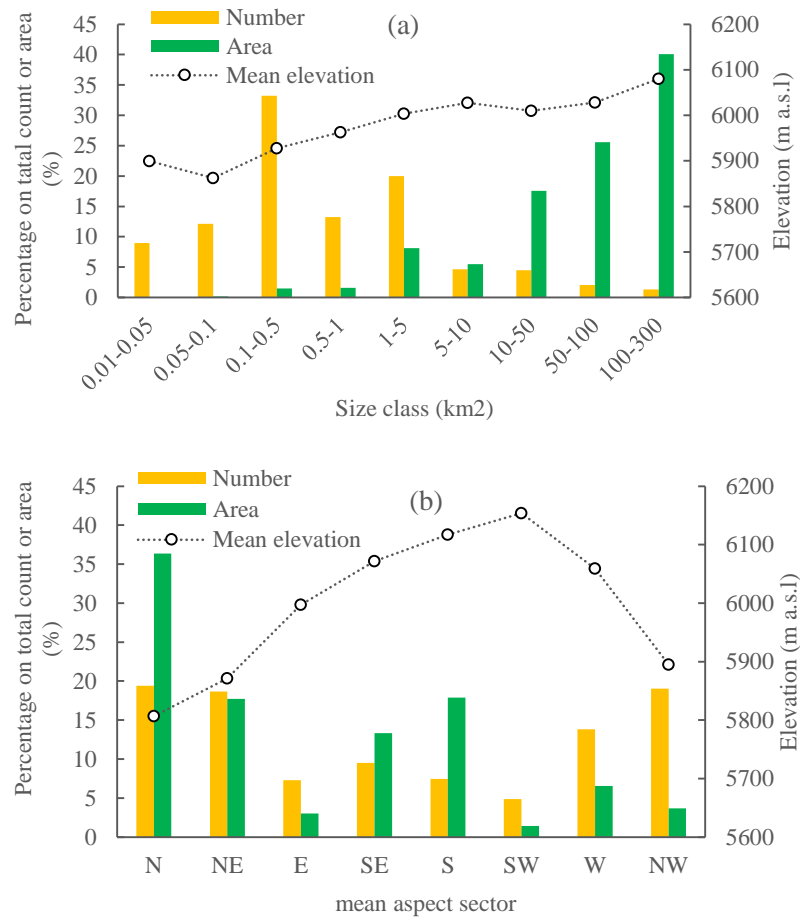


Fig. 7.3 Distribution of the number of glaciers (yellow), glacier area (green), and mean glacier elevations (circles), (a) per size class. (b) per aspect sector.

The distribution of mapped glaciers and the mean elevations are shown in Fig. 7.4. The mean glacier elevation ranges from 5524 m to 6371 m a.s.l., with an average elevation of 5950 m a.s.l.. Small-size glaciers (less than 5 km²) tend to have lower mean elevation than large-size glaciers (Fig. 7.3), as great glaciers are mainly distributed over the high mountain ranges. The mean elevations of glaciers in the southern sectors (S, SW, SE) are about 250 m higher than that in northern sectors (N, NE, NW) on average (6071m and 5857 m a.s.l., respectively). The overall high altitudes of glaciers resulted in high ELA. Based on SRTM DEM, the kinematic ELA of most glaciers is estimated to be within the range of 5930 ± 30 m. For Chongce ice caps, the estimated ELA (5900 m) agrees well with that derived from in-situ mass balance records (5930 m). Considering the uncertainties of ELA estimates and to be comparable with a recent study (Neckel et al., 2014), this study adopts a consistent ELA of 5930 m for separation of the accumulation and ablation area in the WKM region.

The high ELA reflects the extremely cold-dry climatic conditions of the WKM region in comparison with other QTP area (Yao et al., 2012). With this high ELA, most glaciers have a large AAR (the ratio between the accumulation area and the total glacier area) over 0.5.

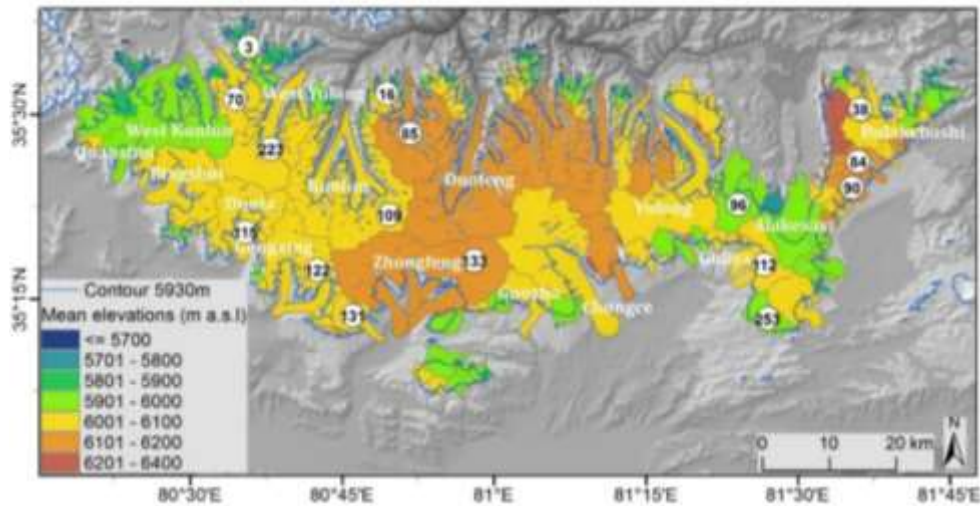


Fig. 7.4 Map of the inventoried glaciers and the mean glacier elevations. Solid blue lines shows the contour list of elevation at 5930 m which is the estimated mean ELA. Number in white circles denotes the local glacier ID with ICESat cover.

1.4.2. Glacier thickness changes

Thickness changes over 16 glaciers (a total area of 1234 km²) are estimated based on ICESat data. The local glacier ID of these glaciers is shown in Fig. 7.4. The time series of dh for ICESat laser periods over each sampled glacier are shown in Fig. S3 of Appendix. Except for the middle parts of the Zhongfeng Glacier, all over-glacier dh trends reveal penetration of SRTM C band into snow, firn and ice of several meters, which is generally consistent with previous studies (Kääb et al., 2012). The Zhongfeng glacier is special because the middle part collapsed due to glacier surging (discussed in the next section).

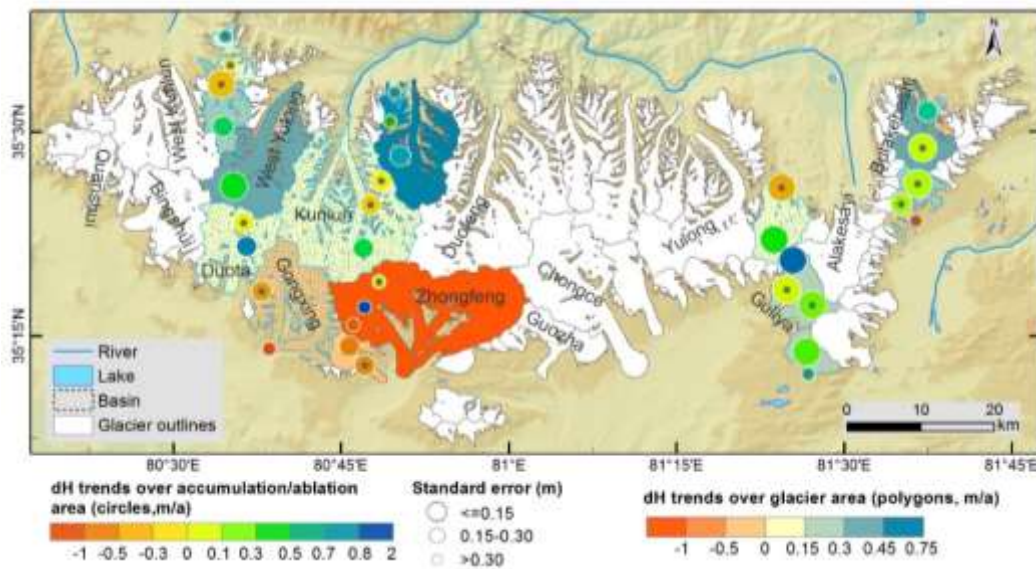


Fig. 7.5 Trends of elevation differences between ICESat and SRTM (dh) over 2003–2008 for different glaciers and glacier accumulation/ablation parts in the WKM area.

The mean trend for each glacier is showed in filled polygons (glacier outlines based on 2013 Landsat maps), with insignificant trends filled with blue dots. Trends for different parts of the glaciers (ablation area, different accumulation sections) are shown in colored data circles (right color bar), with dark grey centers indicating insignificant trends.

ICESat observations reveal that the study glaciers show heterogeneous surface elevation changes over 2003–2008, with mean trends ranging from -1.15 m a^{-1} (the Zhongfeng Glacier) to 0.7 m a^{-1} (local gla ID 85) (Fig. 7.5 and Table 7.2). Most of the glaciers (11) showed increasing trends of surface elevations (trends $> 0.1 \text{ m a}^{-1}$), while three glaciers were in balance (trends within $\pm 0.1 \text{ m a}^{-1}$) and the remaining two glaciers (the Zhongfeng Glacier and its adjacent glacier in the south) showed significant thinning trends. About half of the increasing trends are statistically significant. Generally, glaciers in the eastern part of the WKM region showed significant thickening trends, such as Guliya ice caps and the Bulakebashi, while elevation trends in the western part seem to be aspect-dependent: the northern sectors are dominated by positive balances while the southern sectors tend to be negatively balanced. The two significant thinning trends were observed over glaciers in the western part with mean aspect in the southern sectors (south and southeast). Overall, the mean elevation trends in the north and west sectors were higher than that in the south and southeast sectors (Fig. 7.6b). In addition, a plot of the elevation trends versus the average elevation sampled by ICESat shows that glaciers with high altitudes tend to have higher

Table 7.2 Trends of elevation differences (dh) for different parts of the glaciers based on multi-season ICESat measurements and general statistics about glaciers. The, N, S and C denotes the northern, southern and central parts respectively. Bold numbers indicate trends are significant at 95% significance level.

Local glacier ID	Glacier name	Number of on-glacier ICESat measurements	dh trend (m/a)				Glacier area (km ²)	Mean elevation (m a.s.l)	Mean slope (degree)	Mean aspect sector
			accumulation area	ablation area	on_glacier area	off_glacier area				
70		331	0.43±0.17	-0.12±0.12	0.24±0.15	0.006±0.06	47.1	6000	10.0	N
3		242	-0.06±0.54	0.70±0.42	0.14±0.36	0.006±0.06	19.9	5912	20.2	N
115	Duota	395	0.03±0.18	0.74±0.23	0.16±0.16	0.006±0.06	87.8	6016	8.6	S
223*	West Yulon	518	0.34±0.13	-	0.34±0.12	0.006±0.06	122.8	6020	8.2	NE
122	Gongxing	425	-0.18±0.16	-1.46±0.46	-0.04±0.23	0.006±0.06	118.3	6049	10.2	S
109	Kunlun	467	<u>0.02±0.27(N)</u> 0.42±0.22(S)	-0.12±0.24	0.13±0.18	-0.115±0.05	221.2	6070	13.0	N
131		181	-0.45±0.27	-0.29±0.25	-0.40±0.20	-0.115±0.05	26.3	6017	12.0	SE
16		250	0.28±0.34	0.64±0.42	0.45±0.28	-0.115±0.05	15.8	6007	21.9	NE
85*		230	0.70±0.24	-	0.70±0.24	-0.115±0.05	96.63	6152	14.4	N
133*	Zhongfeng	448	<u>2.03±1.05(C)</u> <u>0.04±0.32 (N)</u> -0.86±0.34 (S)	-	-1.15±0.41	-0.115±0.05	239.4	6103	9.4	S
96		547	0.31±0.12	-0.16±0.12	0.07±0.12	-0.003±0.05	59.9	5920	7.3	N
112	Guliya	604	<u>0.80±0.11(N)</u> <u>0.23±0.13(S)</u>	0.05±0.11	0.29±0.09	-0.003±0.05	58.1	6010	6.8	W
253	Guliya	319	0.26±0.06	0.45±0.35	0.28±0.07	-0.003±0.05	27.1	5991	5.7	SW
90		182	0.16±0.17	-0.49±0.34	-0.05±0.17	0.008±0.03	17.8	6107	14.1	SE
84*		247	0.14±0.11	-	0.14±0.11	0.008±0.03	20.5	6113	10.4	SE
38	Bulakebash	535	0.12±0.10	0.64±0.20	0.31±0.10	0.008±0.03	55.8	6093	11.2	NE

increasing trends than the low-lying glaciers (Fig. 7.6a). The analysis indicates that the spatial variability of glacier elevation changes in the WKM region may be partly explained by the altitude- and aspect- dependence.

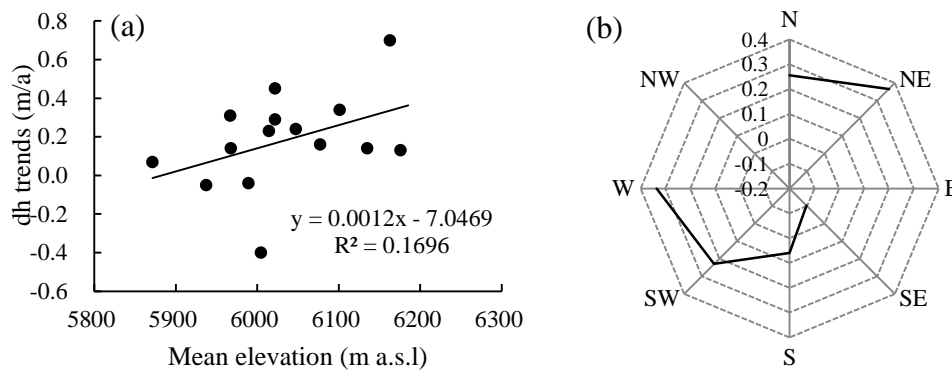


Fig. 7.6 Elevation trends of different glaciers in relation to mean elevation (a) and aspect (b)

Examination of elevation trends over the accumulation/ablation parts reveals varying mass budgets within different parts of the glaciers (Fig. 7.5 and Table 7.2). Thinning trends were observed over both the accumulation and ablation area of two glaciers in the southern sectors: the Gongxing Glacier and its adjacent glacier (ID 131). The second pattern is characterized by significant thickening over the high elevations and slight thinning or balanced state over the low-lying parts. Such pattern was observed over ID 70, ID 109 (the Kunlun Glacier), ID 96 and ID 112 which face the northern or western sector. A more positive balance state than the pattern two was observed over Glacier ID 253 (one composite of the Guliya Ice caps) which experienced thickening trends over both the accumulation and ablation area. An abnormal pattern is observed with more significant (less serious) mass gain (lost) over the ablation area than the accumulation area. As the ablation area is normally exposed to faster thinning than the accumulation area due to higher temperatures and less precipitation, such abnormal pattern indicates rapid ice flow from the upper glacier parts to the lower glacier parts. Half of the 12 glaciers with both measurements on the accumulation and ablation areas showed such converse tendency (Table 7.2), such as the ID 3, ID 115 (Duota) and ID 38 (Bulakebashi).

The elevation change trends over different parts of the accumulation area showed considerable differences, as shown over ID 109 and ID 112 (Fig. 7.7). The sampled accumulation area are divided into the northern and southern sections by the ablation area in the middle. For ID 112, the northern part of accumulation area showed faster increase of surface elevation ($0.80\pm 0.11 \text{ m a}^{-1}$) than the southern part ($0.23\pm 0.13 \text{ m a}^{-1}$); while for ID 109 the northern part kept relatively stable (only $0.02\pm 0.27 \text{ m a}^{-1}$) and the southern part showed significant mass gain ($0.42\pm 0.22 \text{ m a}^{-1}$). The common point is that the upstream part of accumulation area with high altitudes showed faster ice gain than the other downstream part, indicating a normal altitude-dependence of elevation changes within individual glaciers, which is probably associated with the glacier hypsometry and ice flow.

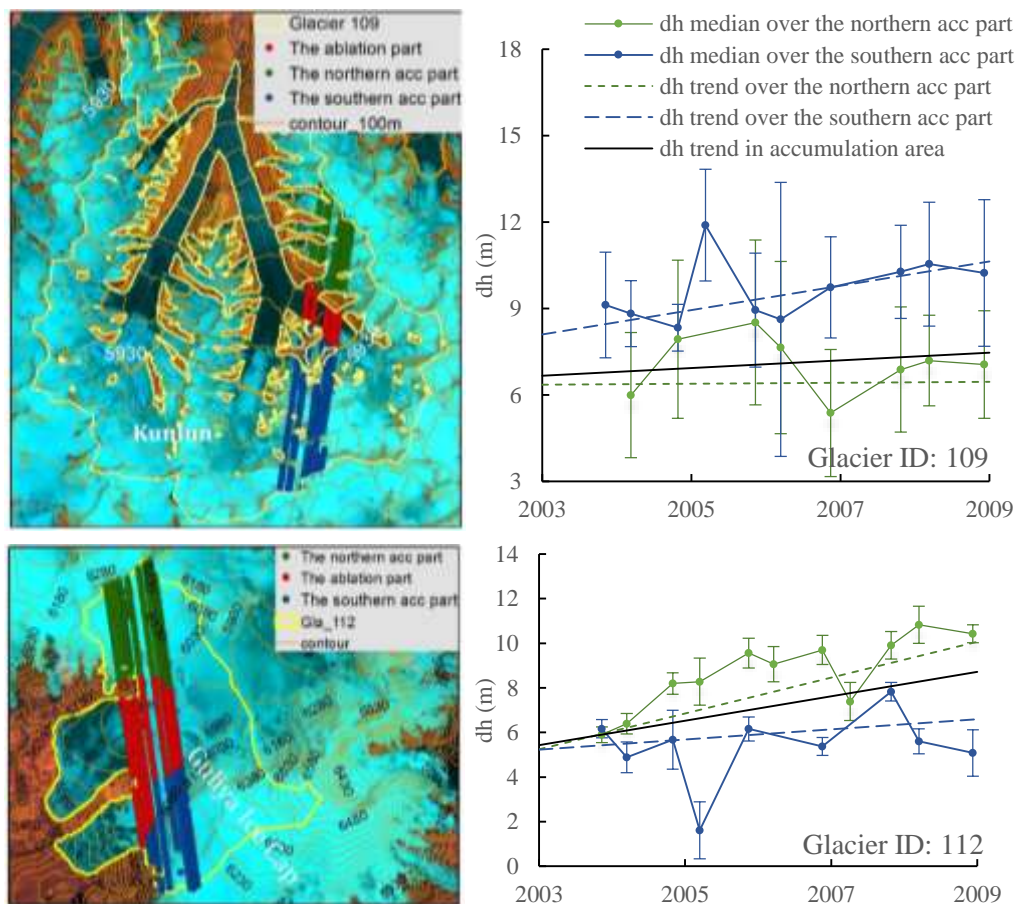


Fig. 7.7 Distribution of ICESat footprints within different parts of glaciers and the linear trends: the Kunlun glacier (Glacier ID 109, upper row) and the northern Guliya Ice caps (Glacier ID 112, lower row).

Based on all ICESat measurements, the surface elevation trend for all study glaciers is $0.20 \pm 0.04 \text{ m a}^{-1}$ (equivalent to mass balance of $0.17 \pm 0.08 \text{ m w.e.a}^{-1}$), over 2003-2008, with trend over the ablation areas ($0.22 \pm 0.08 \text{ m a}^{-1}$, $0.19 \pm 0.10 \text{ m w.e.a}^{-1}$) slightly faster than that over the accumulation areas ($0.19 \pm 0.05 \text{ m a}^{-1}$, $0.16 \pm 0.08 \text{ m w.e.a}^{-1}$). This confirms the general trends of downward ice flow and overall positive mass balances for the study glaciers, whereas the level of mass gain and loss varied across different glaciers and different parts, resulting in variability of overall mass balances.

1.4.3. Glacier surging and terminus changes

1. Glacier surging from ICESat observations

The widely detected rapid ice flow, as inferred from more significant ice gain over the ablation area than the accumulation area, may be linked with glacier surging reported in this region (Yasuda & Furuya, 2013, Li et al., 2013). In particular, surging is detected by ICESat data over the westernmost tributary of the Zhongfeng glacier. An abnormally high variation of elevations (up to -80 m) can be observed over the middle part of the accumulation area (Fig. 7.8). Along the latitude profile of ICESat measurements over the glacier, there is a 'V' shape drop of dh in each laser period (highlighted by rectangle area). A reasonable explanation is that dramatic lowering of the glacier surfaces occurred between the SRTM acquisition date (February 2000) and the first ICESat estimates (March, 2004). The drastic surface lowering (surface crevassing) is a typical feature of glacier surging, and is associated with rapid ice velocities from upstream to downstream area when glacier surging occurred (Yasuda & Furuya, 2013).

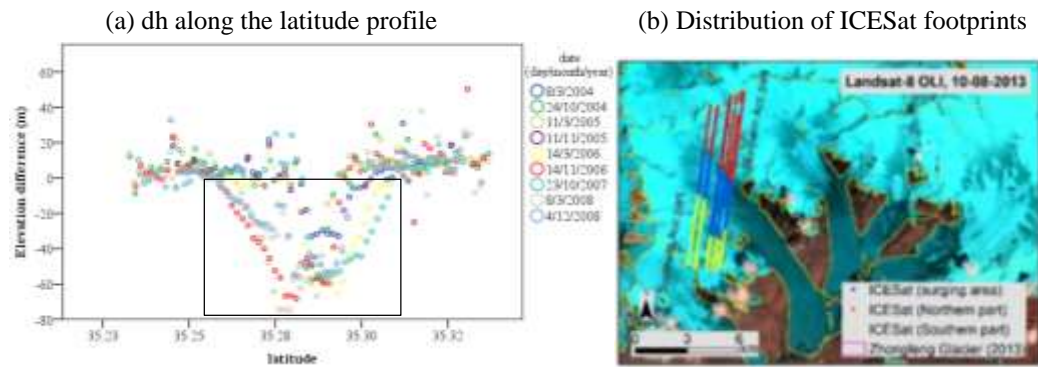


Fig. 7.8 Glacier surging detected by ICESat over the Zhongfeng Glacier. Drastic drop of dh (highlighted by the black rectangle) along the latitude profile of Zhongfeng Glacier in (a) corresponds to caves with the blue ICESat footprints in (b).

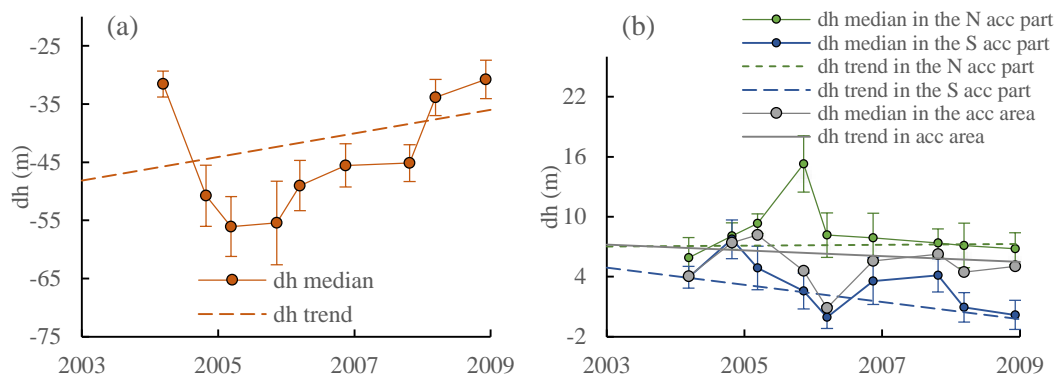


Fig. 7.9 Trends for different parts of the Zhongfeng Glacier in the caves in the accumulation area (a), and other accumulation regions (b).

Around the occurrence of glacier surging, ICESat measurements detected different elevation changes over different parts of a glacier. As shown in Fig. 7.9, fast increases of surface elevations over the cave-in areas show recover of ice mass after glacier surging, while significant surface lowering over the southern accumulation parts (0.86 m a^{-1}) indicate massive ice mass transport from this area to the downstream cave-in areas. The northern upstream areas also experienced ice loss despite of an overall balanced state in the study period. This demonstrated that surging can reshape the glacier hypsometry to a certain extent. Furthermore, it can be inferred that glacier surging could lead to significant mass loss as considerable amount of ice is transported from the upper accumulation area to the low-lying areas. A detailed investigation of the surging of the Zhongfeng glacier

(sustained periods, characteristic process and advancement of terminus), as well as the distribution of other potential surging glaciers and rates of surging in the WKM region, requires further studies with more observations, such as terminus changes, ice velocities and geodetic mass budget measurements.

2. Terminus changes

The frontal changes of a total number of 113 glaciers were examined based on Landsat images acquired during 1999/98-2013. These 113 glaciers cover a total area of 2932 km² which accounts for 93% of the whole study glaciers. Other glaciers were not investigated due to too small size or the difficulty of identifying main tongues. For large glaciers, the length changes along one or several main tongues were examined. Fig. 7.10 shows the approximate location of these frontals and the overall length changes over 1998/99-2013. The terminus of most glaciers kept stable during the past 16 years, without significant advancement or retreat. Among the 20 glaciers which showed obvious changes of terminus locations, 14 glaciers retreated more than 100 m and only 3 glaciers advanced more than 300 m (Fig. 7.10).

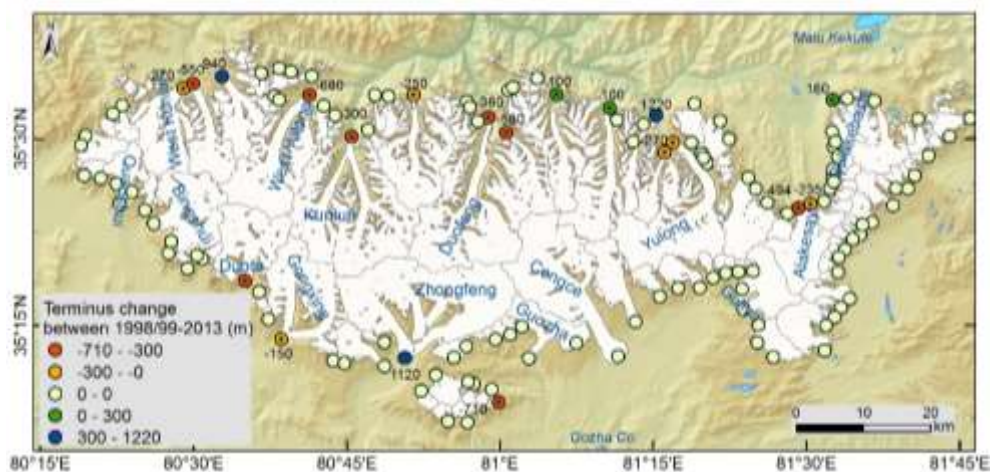


Fig. 7.10 Glacier terminus changes between 1998/1999 and 2013. Significant retreat or advancement is shown with black dots at approximate location of the examined frontals.

Detailed examination of the advancement reveals two types of surging. The first type is characterized by sudden advances at exceptionally high velocities, and the whole process

lasts one to three years. For example, the Glacier ID 70 advanced about 940 m during the past 16 years and most of the advancements occurred over 2009-2010 (about 500 m) and over 2010-2011 (about 300 m) (Fig. 7.11). Similarly, the Zhongfeng glacier advanced about 1000 m over 2003-2004 while kept relatively stable or slightly advanced in other years. In contrast, the advancement of glacier ID 64 is consistent and step-by-step since 1999, with a high velocity ranging from 90 to 150 m a⁻¹ (Fig. 7.11). Although the ice flow is consistent, the velocity apparently exceeded the normal velocities that shown in surrounding glaciers. Therefore it is a surging glacier which has been in a activate phase. This type of surging features a long active phase which may last several years to decades instead of a sudden advancement in a short period.

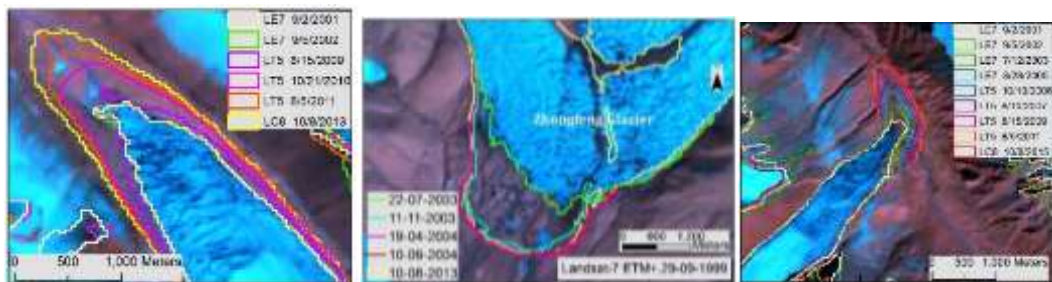


Fig. 7.11 Glacier surging during 1998/1999 and 2013 for three glaciers: glacier ID 70 (left), glacier ID 133 (middle) and glacier ID 64 (right).

The terminus changes of the Zhongfeng glacier, together with the elevation changes over the accumulation area detected by ICESat data, reveal interesting details about glacier surging. Landsat observations show that the advancements of glacier frontal mainly occurred during July 2003 and summer of 2005, with major advancements concentrating July-November 2003 (Fig. 7.11), at a rate about 3.6 km a⁻¹. From November 2003 to April 2004, the glacier terminus continued to advance about 100 m and then kept stable after April 2004. ICESat data show that after the ‘V’ shape drop of surface elevation in March 2004, this area significantly decreased by about 20 m on average during March-November 2004 when the terminus only slightly advanced. These observations suggest that rapid downward ice flow and surface crevassing can continue for several months after the cease of terminus advance. The elevation changes over the caves also suggest that the surface

crevassing started to gain ice accumulation from upstream regions after urging (Fig. 7.9).

1.5. Discussion

1.5.1. Glacier inventory data and accuracy

Glacier outlines provided in RGI v2, GLIMS (updated in Feb 2012) and CGI are compared with our new mapped glacier inventory. Glacier outlines in the published three data sets are similar in the WKM region, and they show quality issues such as location shift, shape distortion and error delineation of inner boundaries (Fig. 7.12).

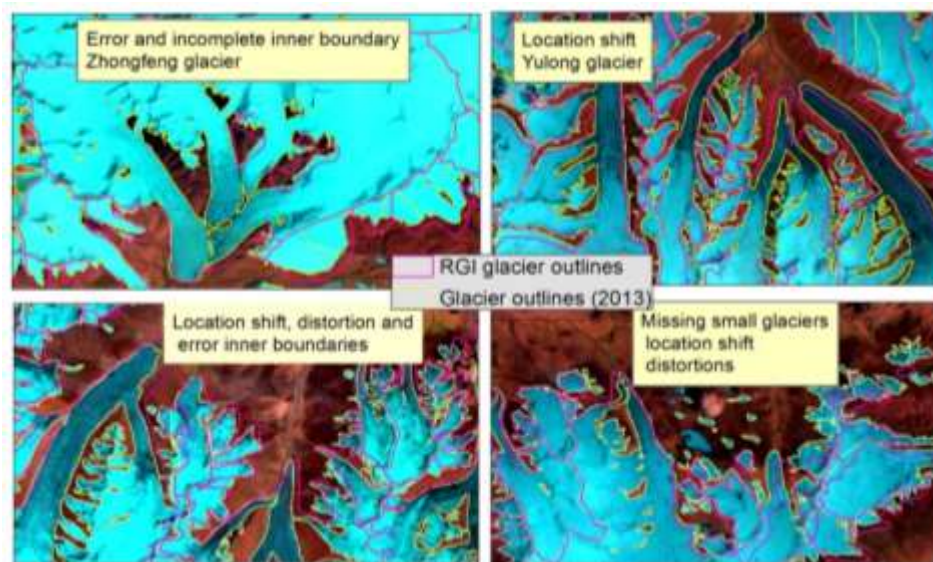


Fig. 7.12 Illustration of problems in previous glacier outlines (RGI is same with GLIMS and CGI). Outlines are superimposed on false color composite of Landsat 8/OLI images acquired in August, 2013.

The semi-automated clean ice mapping method is assumed to have an uncertainty about 3% (e.g. Paul et al., 2002, Andreassen et al., 2008). Major uncertainties lie in influences from cloud cover, shadowed areas and glacier divides in the accumulation areas. Outlines of the cloud-covered parts were referred to images with relatively inferior acquisition dates and this may introduce uncertainties due to seasonal snow cover. Only small regions may be affected by shadow due to the relatively high sun elevations (in the range of 52°-63°) of used images and low topographical relief. Furthermore, NDSI-based approach is effective

in removing some of the illumination effects present on glaciers and yielding satisfactory results in shaded ice (Racoviteanu et al., 2008). The number of glaciers depends on the threshold of minimum size on glaciers, and different interpretation of small size entities as snow patches or glaciers. Uncertainties in the SRTM elevation data may affect the separation of ice divides and have impact on the number of glaciers, but will not influence the total mapped glacierized area. The retrieved glacier topographical parameters may also be impacted by errors in SRTM.

1.5.2. Uncertainties and implications of glacier dynamics

In the WKM region, the distribution of ICESat footprints is in good agreement with the glacier hypsometry (shown in Fig.S4 in the appendix), and the number of measurements used for each trend is relatively sufficient (Table 7.2). It is worth noting that ICESat data only sampled a limited number of glaciers in the region, and data are only available over the accumulation or the ablation areas for some glaciers (Table 7.2). This may result in uncertainties of trends estimated for individual glaciers and analysis on the spatial patterns. In addition, trends derived from autumn data are similar to that based on multi-seasonal data (see Table S1 in the appendix), which justifies the use of multi-seasonal data for trend estimation in this region.

Previous studies reported slight increase of glacier area in the WKM region over 2001-2009 (Zhang et al., 2012, Li et al., 2013); and the glacier area increased in the eastern part and decreased in the western parts (Zhang et al., 2012). This agrees well with our study which revealed an overall positive trend for the WKM glaciers and more positive balances for glaciers in the eastern part than the western part. The observed mass gain and heterogeneous changes of glaciers in the WKM region seems to be a similar anomaly with the adjacent Pamir and the Karakoram Mountains (Hewitt, 2005, Kääb et al., 2012, Gardelle et al., 2013). A recent study estimated slightly positive trend ($0.04 \pm 0.29 \text{ m a}^{-1}$) in the ablation area of glaciers in the WKM region (Neckel et al., 2014). The estimated trend is less significant than our estimates ($0.22 \pm 0.08 \text{ m a}^{-1}$), which may be attributable to

different study extent. This study showed more details on the heterogeneity of glacier dynamics within the WKM region, as well as varying elevation trends over different parts of individual glaciers. The spatial variability of detected trends seems to be connected with local glacier parameters including altitude, aspect, hypsometry and ice flow. These factors can be significant in the WKM region because there are a collection of great glaciers which have complicated structure (many tributaries from different basins, long tongues, large elevation ranges) and diverse terrain.

Some surging glaciers in the WKM region were investigated with Landsat data (Li et al., 2013) and PALSAR glacier velocity observations (Yasuda & Furuya, 2013). The former study identified two surging glaciers in the south slope (the Zhongfeng glacier and the Chongce glacier surging during mid 1990s), while the latter determined four surging glaciers including the Zhongfeng glacier. The three surging glaciers we identified were confirmed in the two studies. However, Yasuda & Furuya (2013) associated the fast velocity of the West Kunlun glacier in winter 2008 with surging, while no significant terminus changes can be observed from Landsat images during the period. On the contrary, the West Kunlun glacier retreated during 1999-2013. Both this study and Yasuda & Furuya, 2013 suggest that there may be more surging type glaciers in the area. This study suggests that the potential surging glaciers can be characterized by faster accumulation over the low-lying ablation areas than the accumulation area. While most surging glaciers found in the Karakorum region are debris-covered, these observations indicate debris-free surging glaciers might be common in the WKM region, which has not been fully understood and studied at present.

1.6. Conclusions

Based on latest Landsat 8 imagery (2013), the updated glacier inventory of 537 glaciers (covering an area of 3137 km²) in the WKM region in northwestern QTP will fill gaps in world glacier inventory and support further studies about glacier changes. The dense

distribution of great glaciers in the WKM region and good ICESat coverage enabled a detailed examination of thickness changes of 16 groups of glaciers covering an area about 1234 km² (2013). The results reveal high local heterogeneity in both the overall glacier mass balances and dynamics on the accumulation and ablation parts within individual glaciers. The surface elevation trends for the study glaciers ranged from -0.4 ± 0.20 m a⁻¹ to 0.7 ± 0.24 m a⁻¹ (except the surging glacier), with an average mass gain at 0.20 ± 0.04 m a⁻¹ over 2003-2008. About half of examined glaciers showed faster mass gain over the ablation area than that over the accumulation areas, indicating the general trends of downward ice flow which are likely caused by rapid mass gain at high elevations or serious mass loss at the low-lying areas. In particular, ICESat data detected drastic lowering and different pattern of elevation trends over the accumulation area of the Zhongfeng glacier due to glacier surging.

Seasonal snow and cloud cover hampered the generation of multi-temporal glacier inventories for the entire region and only the terminus changes of a subset of 113 glaciers covering an area of about 2932 km² (2013) were studied for the periods of 1998/1999-2013. The terminus changes of individual glaciers further revealed a heterogeneous response of glacier frontals during the past 16 years, with most glaciers keeping stable, 14 glaciers retreating more than 100 m and only 3 glaciers advancing more than 300 m due to surging. The varying rates of glacier tongue retreat/advance, as well as the heterogeneous thickness changes of glaciers in the WKM region, reflect glacier dynamics that are probably associated with inner glacier parameters including altitude, aspect, glacier hypsometry, and ice flow. The heterogeneity is similar to Karakoram glaciers where increase of solid precipitation over the accumulation areas have been observed. However, the mechanisms for glacier surging and mass gain need to be further explored with more observations including terminus changes, ice velocities and geodetic mass budget measurements, in order to better understand the response of the WKM glaciers to climate change.

Chapter 8

Conclusions and outlook

Changes of the extensively glacierized regions over the QTP have attracted growing attention from both the scientific and public communities in recent decades. The highly variable geography, complex topography and heterogeneous climate conditions across this plateau pose challenges for remote sensing researchers in studying and understanding the glacier distribution, glacier changes and the driving force. To improve the accuracy and efficiency of large-scale glacier mapping, this study has developed a semi-automated scheme which integrates multi-mission and multi-temporal remote sensing observations including Landsat imagery, InSAR data and a DEM for extracting clean-ice glaciers and debris-covered glaciers separately. The method can mitigate the influences of frequent cloud activities and improve the mapping efficiency and quality of debris-covered glaciers. By carrying out fine-scale research into different types of glaciers (temperate, semi-continental and continental) over three most glacierized sub-regions of the QTP, this work has demonstrated contrasting behaviors of different type glaciers over these regions in recent decades. The research results contribute to a better understanding of the challenges in glacier mapping, of the complexity and uncertainties of glacier changes, and of the effects of the changing climate on glacier mass balances. In addition, the study has provided insights into integrating different remote sensing techniques for mapping and monitoring glaciers by considering pros and cons of the different techniques. The main contributions of the research presented in the thesis are:

- (1) A complete glacier inventory for the cloud-affected southeastern QTP is presented by integrating observations from Landsat satellites and InSAR techniques. The proposed semi-automated method can mitigate the effect of cloud cover and seasonal snow cover on clean-ice mapping and is effective in identification of debris-covered glacier tongues. The resulted glacier inventory reveals that there are considerable

overestimation of the total glacierized area (30% more) in previous glacier inventories due to the use of cloud-free images which contain large seasonal snow cover. The new glacier inventory allows new findings about the characteristics of glaciers in this region and is a baseline dataset for various studies related to the assessment of glacier changes and the impacts.

- (2) ICESat laser altimetry measurements are improved to derive glacier elevation changes over the DKMD region in the central QTP. Results from the ICESat data, volume-scaling model and in-situ data are generally consistent, showing that it is feasible to achieve consensus estimates with multi-source satellite observations. With the ICESat data, quantitative estimates of glacier elevation changes and mass balances are given over three glacierized regions. The results show contrasting patterns of glacier behavior in the past decade, from the strongest mass loss of temperate glaciers (-0.72 ± 0.20 m w.e.a⁻¹) in the SE QTP, to moderate mass loss of semi-continental glaciers (-0.42 ± 0.15 m w.e.a⁻¹) over the central plateau and to the most significant mass gain of continental glaciers (0.17 ± 0.08 m w.e.a⁻¹) over the WKM in the northwest.

- (3) The overall glacier mass loss (4.71 ± 1.30 Gt a⁻¹) over the SE QTP equals to contribution of 0.012 ± 0.005 mm sea level rise during 2003 and 2008. The ICESat data reveal remarkable variability in the glacier thinning rates among the sub-regions (ranging from -0.38 ± 0.27 m w.e.a⁻¹ to -1.05 ± 0.36 m w.e.a⁻¹), which is generally consistent with GRACE observations. More rapid thinning was found over the debris-covered ice (-0.96 ± 0.17 m a⁻¹) than over the clean-ice areas (-0.78 ± 0.20 m a⁻¹). The spatial variability of glacier changes is likely attributable to the different pattern of precipitation changes within the region. Glacier mass loss was closely associated with the dramatic rise of temperature accompanied by considerable decrease in precipitation in warm seasons in the past decade. Overall, the mean temperature in the warm seasons is the most significant factor controlling net annual glacier mass balances.

- (4) Glacier changes in the WKM region exhibited high heterogeneity (in the range of $-1.15 \sim +0.70 \text{ m a}^{-1}$) which is probably associated with individual glacier parameters including the altitude, aspect, hypsometry, and ice flow of a glacier, as well as glacier surging events which are not directly driven by climate change. The Landsat observations confirm the relatively stable terminuses of most glaciers in the WKM in the past 16 years and show three surging events characterized by varying pattern of advancement.
- (5) The glaciers in the mid-latitude central QTP showed direct and quick response to local temperature and precipitation variations, and the annual temperature exerts the strongest impact on the glacier changes. In contrary to traditional assumptions on the monsoon-dominated climate, the DKMD region is found to be dominated by continental westerly circulations instead of ISM in the recent two decades and the glacier variations showed close connection with NAO and SOI. The NAO is tele-connected with the climate in this region, probably through regulation on the direction of westerlies and storm tracks, while the super ENSO events seem to favor glacier accumulation with some tele-connection with abnormally high snow fall.

Remote sensing is a promising data source for mapping and monitoring glaciers. Further research is needed to enrich observations on glacier changes on more extended spatial and temporal scales. Meanwhile, it is also important to enhance and derive in situ mass balance measurements of mountain glaciers over the QTP to validate the remote sensing estimates. With the increasing observations from Landsat 8, new glacier inventories for the QTP can be generated, and the long-term areal or length changes of glaciers can be investigated. Furthermore, the extension of observations on glacier surface elevations can be expected from the new satellite altimetry missions such as the ICESat-2 and the CryoSat-2 mission. There are also promising geodetic measurements from the coming TanDEM-X WorldDEM1 - another global DEM, which will allow for comprehensive mass balance estimates between 2000 and 2012/2013 by combining with the global SRTM DEM and the

new glacier inventory. Such estimates with continuous spatial coverage are crucial for evaluating mass balances of surging glaciers which are commonly found in the northwestern plateau. The increasing observations are fundamental for understanding the heterogeneity of glacier changes and the glacier-climate interactions over the plateau. More research is also needed to address how the local and regional climate dynamics affect glacier mass balances. Such evaluation will contribute to better understanding of the glacier variations, to better projection and modeling of future glacier changes and to assess the impact on environment.

Appendix

Supplementary data for Chapter 6

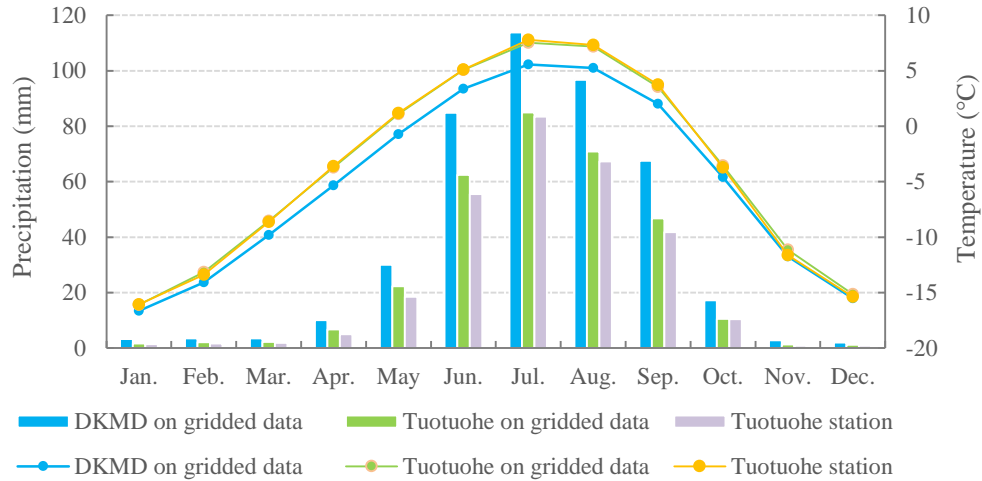


Fig. S1 Multi-year averaged (1976-2013) monthly temperature (lines) and precipitation (bars) over the DKMD and Tuotuohe based on CN05 gridded climate dataset, in comparison with records derived from the Tuotuohe meteorological station. For the Tuotuohe region, data from the CN05 dataset are highly consistent with that recorded at the meteorological station. The intra-annual variation of climatic variables over the DKMD region are similar to that of Tuotuohe region, with relatively higher level of precipitation totals and lower level of temperature due to the higher altitudes.

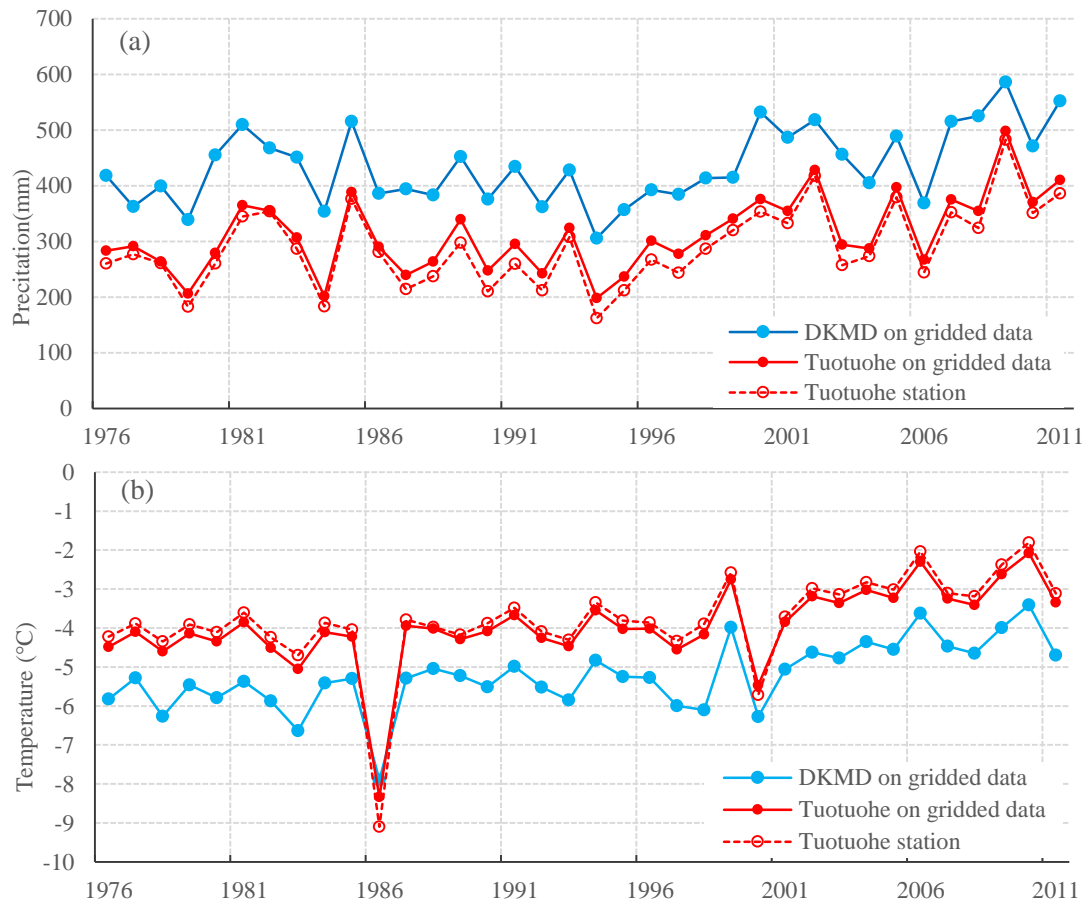
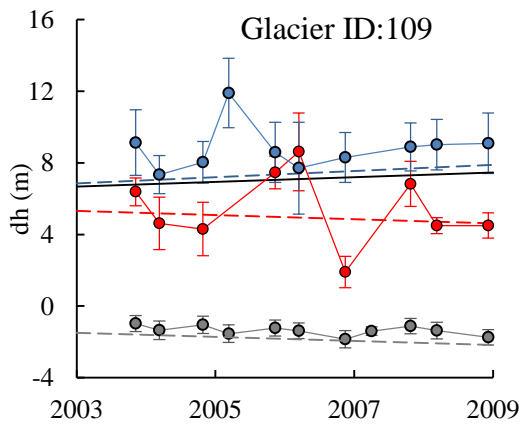
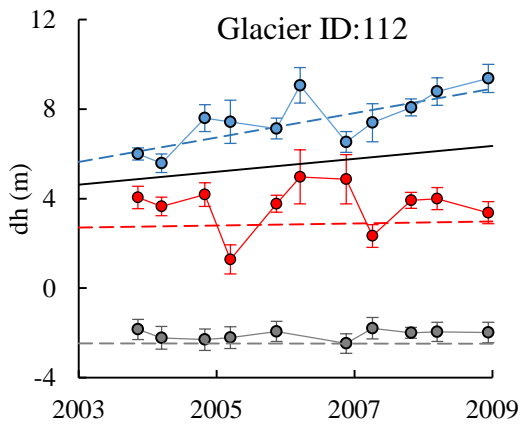
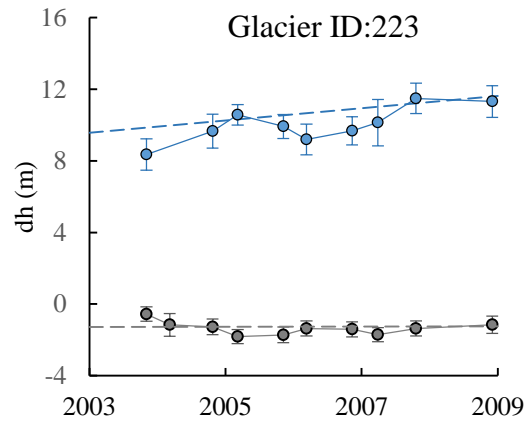
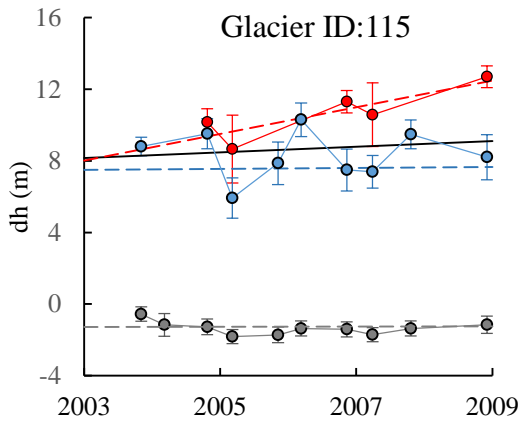
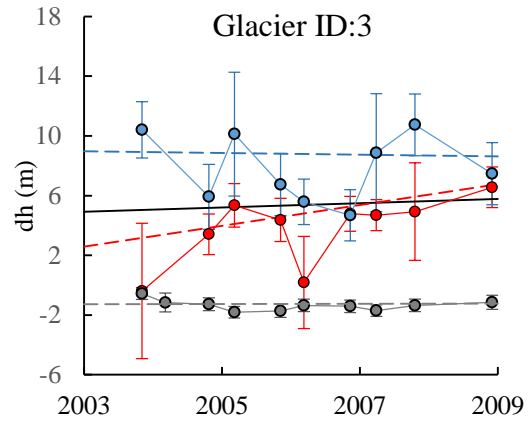
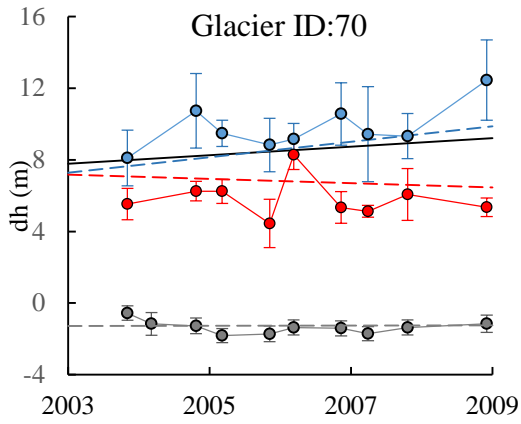
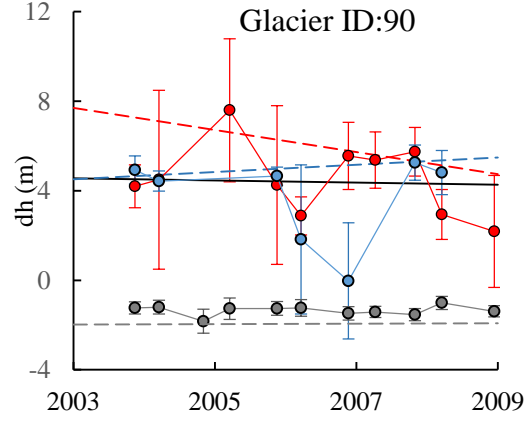
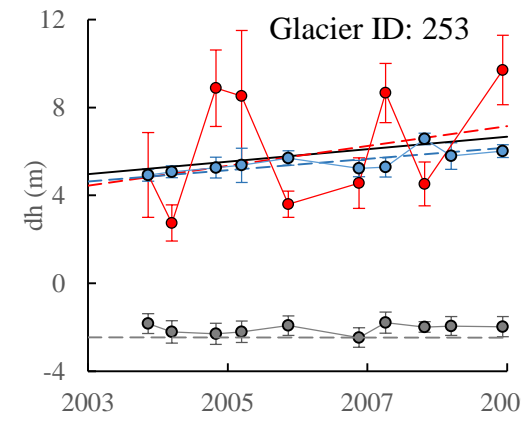
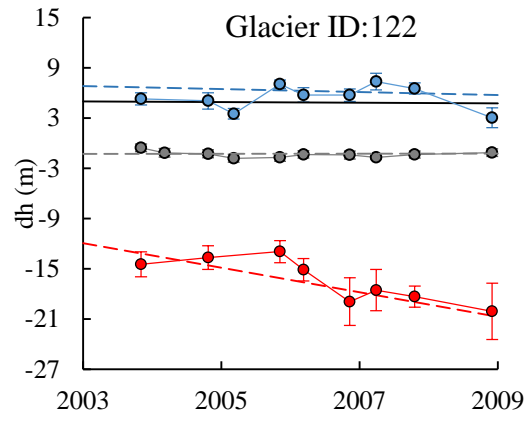
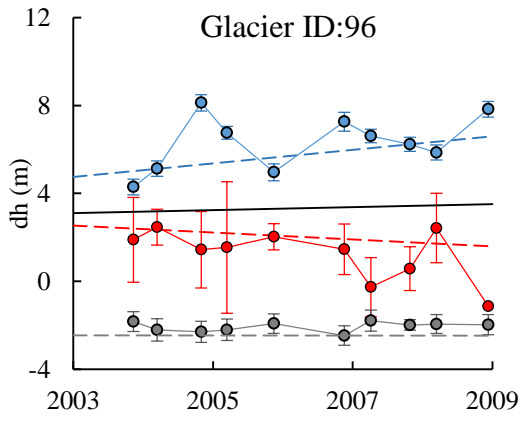
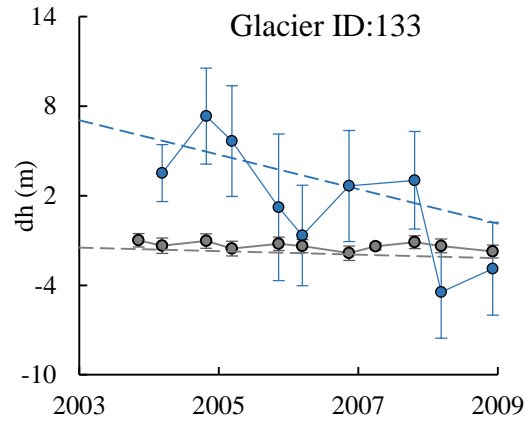
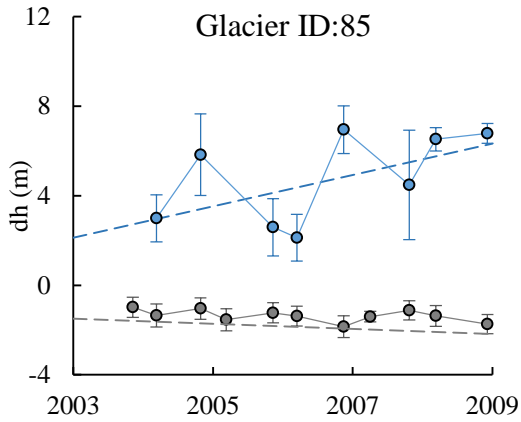
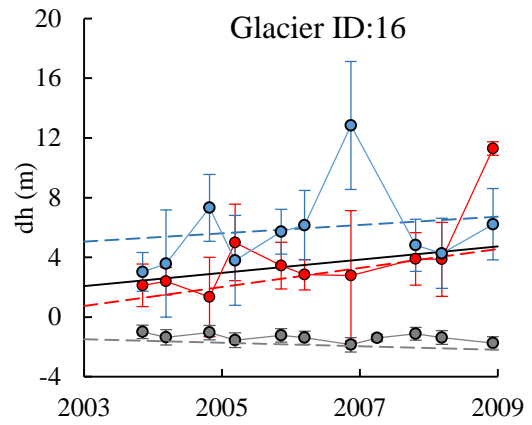
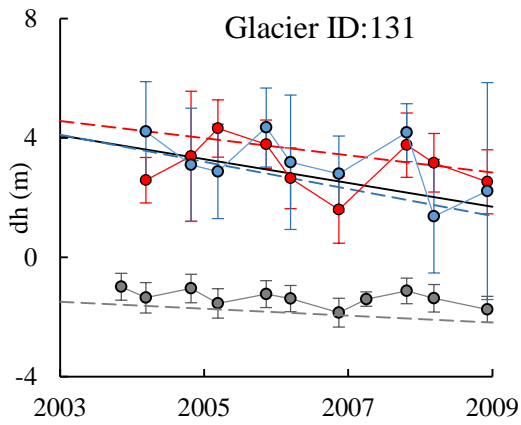


Fig. S2 Inter-annual variation of precipitation (a) and temperature (b) over 1976-2013 for the DKMD region (CN05 gridded dataset), Tuotuohe (CN05 gridded dataset) in comparison with records at the Tuotuohe meteorological station. The three time-series are highly consistent in depicting the inter-annual climate variations.

Supplementary data for Chapter 7





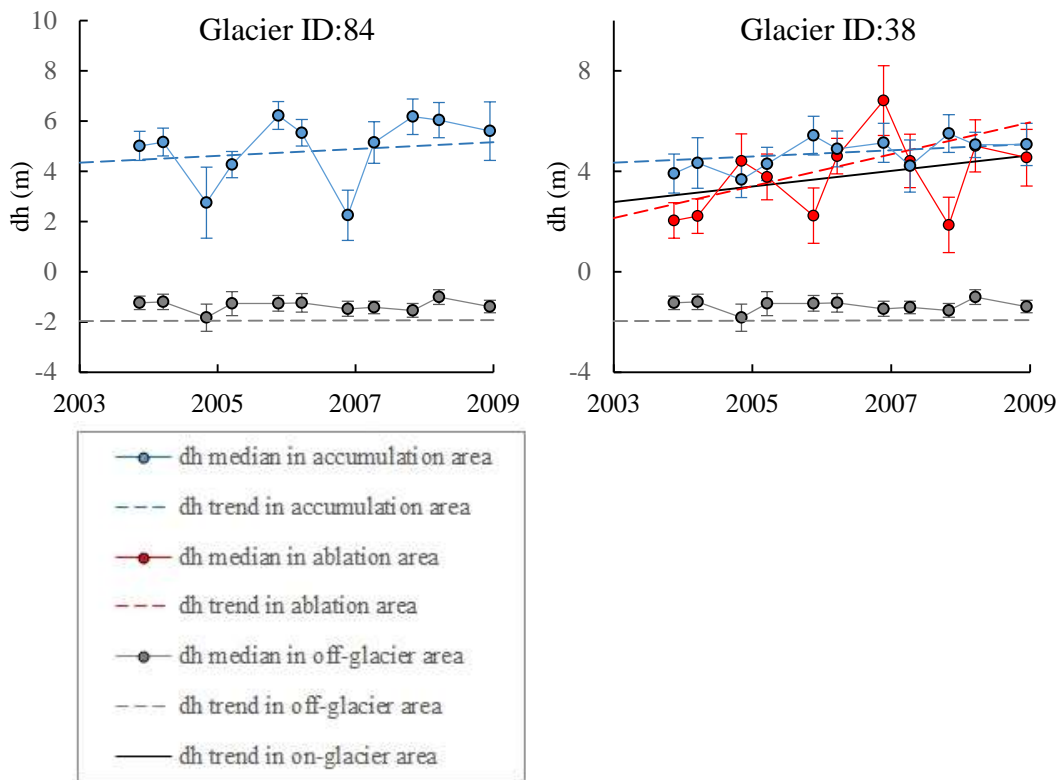


Fig. S3 Trends for individual glaciers based on autumn and winter ICESat acquisitions. Information on the sampled glaciers and local glacier ID is shown in Figure 7.4 and Table 7.2. Trends are fitted through all dh values on- and off-glacier areas. Trends for the accumulation and ablation areas are shown separately. For clarity only the dh median of each laser period is given.

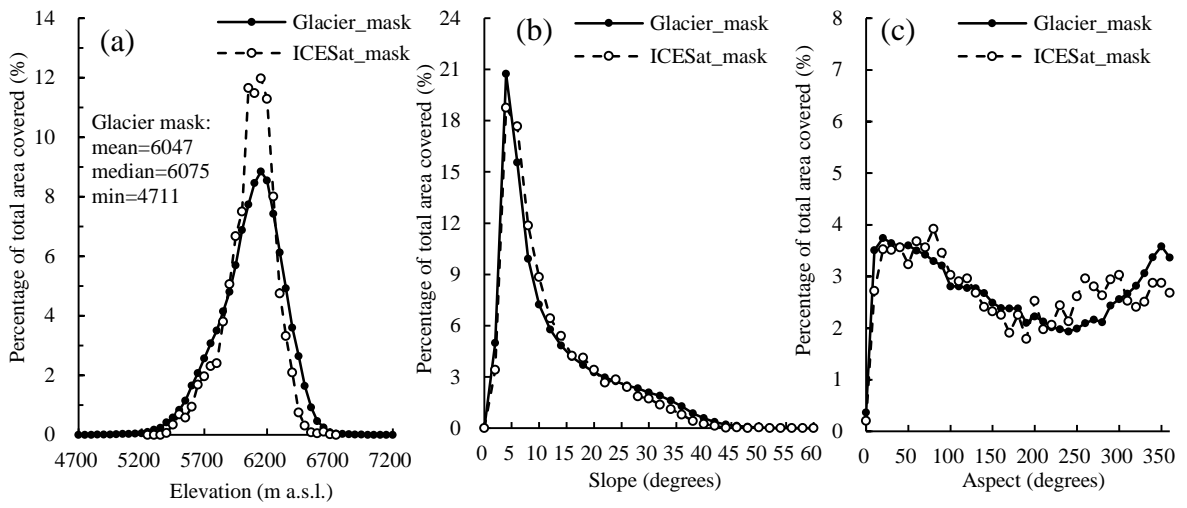


Fig. S4 Histograms of the study glaciers mask and ICESat footprints for elevation (a), slope (b) and aspect(c).

Table S1 Trends of elevation differences (dh) for different parts of the glaciers based on ICESat measurements of autumn seasons. The N, S and C denote the northern, southern and central parts respectively. Bold numbers indicate trends are significant at 95% significance level.

Local glacier ID	Glacier name	Number of ICESat footprints	Autumn dh trend (m/a)			
			accumulation area	ablation area	on_glacier area	off_glacier area
70		204	0.54±0.21	0.01±0.12	0.33±0.19	-0.001±0.07
3		162	0.00±0.56	0.84±0.43	0.16±0.38	-0.001±0.07
115	Duota	259	-0.03±0.17	0.59±0.24	0.09±0.15	-0.001±0.07
122	Gongxing	300	-0.30±0.18	-1.46±0.48	-0.04±0.24	-0.001±0.07
223	West Yulong	360	0.43±0.15	-	0.43±0.14	-0.001±0.07
109	Kunlun	302	-0.19±0.38 (N) 0.50±0.29 (S)	-0.04±0.33	0.15±0.25	-0.176±0.06
131		101	-0.44±0.41	-0.32±0.35	-0.34±0.30	-0.176±0.06
16		146	0.19±0.50	0.97±0.63	0.55±0.41	-0.176±0.06
85		144	0.44±0.36	-	0.44±0.36	-0.176±0.06
133	Zhongfeng	228	4.05±1.57 (C) -0.02±0.43 (N) -1.34±0.57(S)	-	-3.01±1.07	-0.176±0.06
96		316	0.29±0.17	-0.27±0.17	-0.01±0.16	-0.066±0.06
112	Guliya	370	0.78±0.14 (N) 0.16±0.17 (S)	0.00±0.14	0.27±0.12	-0.066±0.06
253	Guliya	212	0.26±0.07	0.32±0.40	0.28±0.08	-0.066±0.06
90		93	0.15±0.23	-0.23±0.50	-0.08±0.21	0.001±0.04
84		128	0.03±0.18	-	0.03±0.18	0.001±0.04
38	Bulakebashi	295	0.15±0.12	0.61±0.29	0.32±0.13	0.001±0.04

References

- Ageta, Y., Wenjing, Z., & NARAWO, M. (1989). Mass balance studies on Chongce Ice Cap in the west Kunlun Mountains. *Bulletin of glacier research*, 37-43
- Ageta, Y., & Kadota, T. (1992). Predictions of changes of glacier mass balance in the Nepal Himalaya and Tibetan Plateau: a case study of air temperature increase for three glaciers. *Annals of Glaciology*, 16, 89-94
- Aizen, E.M., Aizen, V.B., Melack, J.M., Nakamura, T., & Ohta, T. (2001). Precipitation and atmospheric circulation patterns at mid- latitudes of Asia. *International Journal of Climatology*, 21, 535-556
- Andreassen, L., Paul, F., Kääh, A., & Hausberg, J. (2008). Landsat-derived glacier inventory for Jotunheimen, Norway, and deduced glacier changes since the 1930s. *The Cryosphere*, 2, 131-145
- Arendt, A., Bolch, T., Cogley, J., Gardner, A., Hagen, J., Hock, R., et al. (2012). Randolph Glacier Inventory [v2. 0]: A Dataset of Global Glacier Outlines. Global Land Ice Measurements from Space, Boulder Colorado, USA. *Digital Media*
- Arendt, A.A., Echelmeyer, K.A., Harrison, W.D., Lingle, C.S., & Valentine, V.B. (2002). Rapid wastage of Alaska glaciers and their contribution to rising sea level. *Science*, 297, 382-386
- Atwood, D., Meyer, F., & Arendt, A. (2010). Using L-band SAR coherence to delineate glacier extent. *Canadian Journal of Remote Sensing*, 36, S186-S195
- Bahr, D.B. (1997a). Width and length scaling of glaciers. *Journal of Glaciology*, 43, 557-562
- Bahr, D.B., Pfeffer, W.T., Sassolas, C., & Meier, M.F. (1998). Response time of glaciers as a function of size and mass balance: 1. Theory. *Journal of Geophysical Research: Solid Earth (1978–2012)*, 103, 9777-9782
- Bahr, D.B. (1997b). Global distributions of glacier properties: A stochastic scaling paradigm. *Water Resources Research*, 33, 1669-1679
- Bajracharya, S.R., & Shrestha, B. (Eds.), (2011). *The status of glaciers in the Hindu Kush-Himalayan region*. (pp. 125). Kathmandu: International Centre for Integrated Mountain Development
- Bamber, J.L., & Rivera, A. (2007). A review of remote sensing methods for glacier mass balance determination. *Global and Planetary Change*, 59, 138-148
- Barry, R.G. (2006). The status of research on glaciers and global glacier recession: a review. *Progress in Physical Geography*, 30, 285-306
- Berthier, E., Arnaud, Y., Kumar, R., Ahmad, S., Wagon, P., & Chevallier, P. (2007). Remote sensing estimates of glacier mass balances in the Himachal Pradesh (Western Himalaya, India). *Remote Sensing of Environment*, 108, 327-338
- Bettadpur, S. (2012). Insights into the Earth system mass variability from CSR-RL05 GRACE gravity fields. *EGU General Assembly*, 22-27 April 2012, p6409

- Bhambri, R., Bolch, T., Kawishwar, P., Dobhal, D., Srivastava, D., & Pratap, B. (2013). Heterogeneity in glacier response in the upper Shyok valley, northeast Karakoram. *The Cryosphere*, 7(5), 1385-1398
- Bhambri, R., Bolch, T., Chaujar, R.K., & Kulshreshtha, S.C. (2011). Glacier changes in the Garhwal Himalaya, India, from 1968 to 2006 based on remote sensing. *Journal of Glaciology*, 57, 543-556
- Bolch, T., Yao, T., Kang, S., Buchroithner, M., Scherer, D., Maussion, F., et al. (2010a). A glacier inventory for the western Nyainqentanglha Range and the Nam Co Basin, Tibet, and glacier changes 1976–2009. *The Cryosphere*, 4, 419-433
- Bolch, T., Kulkarni, A., Käab, A., Huggel, C., Paul, F., Cogley, J., et al. (2012). The state and fate of Himalayan glaciers. *Science*, 336, 310-314
- Bolch, T., & Kamp, U. (2006). Glacier mapping in high mountains using DEMs, Landsat and ASTER data. *Grazer Schriften der Geographie und Raumforschung*, 41, 37-48
- Bolch, T., Menounos, B., & Wheate, R. (2010b). Landsat-based inventory of glaciers in western Canada, 1985–2005. *Remote Sensing of Environment*, 114, 127-137
- Bolch, T., Buchroithner, M.F., Kunert, A., & Kamp, U. (2007). Automated delineation of debris-covered glaciers based on ASTER data. in *GeoInformation in Europe, Proceedings 27th Annual Symposium European Association of Remote Sensing Laboratories (EARSeL)*, Mill press, Rotterdam, 403-410
- Burns, P., & Nolin, A. (2014). Using atmospherically-corrected Landsat imagery to measure glacier area change in the Cordillera Blanca, Peru from 1987 to 2010. *Remote Sensing of Environment*, 140, 165-178
- Chander, G., Markham, B.L., & Helder, D.L. (2009). Summary of current radiometric calibration coefficients for Landsat MSS, TM, ETM , and EO-1 ALI sensors. *Remote Sensing of Environment*, 113, 893-903
- Chang, C., Harr, P., & Ju, J. (2001). Possible roles of Atlantic circulations on the weakening Indian monsoon rainfall-ENSO relationship. *Journal of Climate*, 14, 2376-2380
- Chen, J., Tapley, B., & Wilson, C. (2006). Alaskan mountain glacial melting observed by satellite gravimetry. *Earth and Planetary Science Letters*, 248, 368-378
- Chen, F., Chen, J., Holmes, J., Boomer, I., Austin, P., Gates, J.B., et al. (2010). Moisture changes over the last millennium in arid central Asia: a review, synthesis and comparison with monsoon region. *Quaternary Science Reviews*, 29, 1055-1068
- Clark, M.K., House, M., Royden, L., Whipple, K., Burchfiel, B., Zhang, X., et al. (2005). Late Cenozoic uplift of southeastern Tibet. *Geology*, 33, 525-528
- Clarke, G.K., Collins, S.G., & Thompson, D.E. (1984). Flow, thermal structure, and subglacial conditions of a surge-type glacier. *Canadian Journal of Earth Sciences*, 21, 232-240
- Cogley, J.G. (2010). A more complete version of the World Glacier Inventory. *Annals of Glaciology*, 50, 32-38

- Davis, C.H., Li, Y., McConnell, J.R., Frey, M.M., & Hanna, E. (2005). Snowfall-driven growth in East Antarctic ice sheet mitigates recent sea-level rise. *Science*, *308*, 1898-1901
- Ding, Y., Liu, S., Li, J., & Shangguan, D. (2006). The retreat of glaciers in response to recent climate warming in western China. *Annals of Glaciology*, *43*, 97-105
- Duan, A., & Wu, G. (2005). Role of the Tibetan Plateau thermal forcing in the summer climate patterns over subtropical Asia. *Climate Dynamics*, *24*, 793-807
- Dyurgerov, M.B., & Meier, M.F. (2000). Twentieth century climate change: Evidence from small glaciers. *Proceedings of the National Academy of Sciences*, *97*, 1406-1411
- Ewert, H., Popov, S.V., Richter, A., Schwabe, J., Scheinert, M., & Dietrich, R. (2012). Precise analysis of ICESat altimetry data and assessment of the hydrostatic equilibrium for subglacial Lake Vostok, East Antarctica. *Geophysical Journal International*, *191*, 557-568
- Fielding, E., Isacks, B., Barazangi, M., & Duncan, C. (1994). How flat is Tibet? *Geology*, *22*, 163-167
- Francis, J.A., & Vavrus, S.J. (2012). Evidence linking Arctic amplification to extreme weather in mid- latitudes. *Geophysical Research Letters*, *39*, L06801
- Frauenfeld, O.W., Zhang, T., & Serreze, M.C. (2005). Climate change and variability using European Centre for Medium- Range Weather Forecasts reanalysis (ERA- 40) temperatures on the Tibetan Plateau. *Journal of Geophysical Research: Atmospheres (1984–2012)*, *110*
- Frey, H., & Paul, F. (2012). On the suitability of the SRTM DEM and ASTER GDEM for the compilation of topographic parameters in glacier inventories. *International Journal of Applied Earth Observation and Geoinformation*, *18*, 480-490
- Frey, H., Paul, F., & Strozzi, T. (2012). Compilation of a glacier inventory for the western Himalayas from satellite data: methods, challenges, and results. *Remote Sensing of Environment*, *124*, 832-843
- Fujita, K. (2008). Influence of precipitation seasonality on glacier mass balance and its sensitivity to climate change. *Annals of Glaciology*, *48*, 88-92
- Fujita, K., & Ageta, Y. (2000). Effect of summer accumulation on glacier mass balance on the Tibetan Plateau revealed by mass-balance model. *Journal of Glaciology*, *46*, 244-252
- Gardelle, J., Berthier, E., & Arnaud, Y. (2012). Slight mass gain of Karakoram glaciers in the early twenty-first century. *Nature geoscience*, *5*, 322-325
- Gardelle, J., Berthier, E., Arnaud, Y., & Käab, A. (2013). Region-wide glacier mass balances over the Pamir-Karakoram-Himalaya during 1999-2011. *The Cryosphere*, *7*, 1263-1286
- Gardner, A.S., Moholdt, G., Cogley, J.G., Wouters, B., Arendt, A.A., Wahr, J., et al. (2013). A reconciled estimate of glacier contributions to sea level rise: 2003 to 2009. *Science*, *340*, 852-857
- Geruo, A., Wahr, J., & Zhong, S. (2013). Computations of the viscoelastic response of a 3-D compressible Earth to surface loading: an application to Glacial Isostatic Adjustment in Antarctica and Canada. *Geophysical Journal International*, *192*, 557-572

- Goldstein, R.M., & Werner, C.L. (1998). Radar interferogram filtering for geophysical applications. *Geophysical Research Letters*, 25, 4035-4038
- Goswami, B.N., Madhusoodanan, M., Neema, C., & Sengupta, D. (2006). A physical mechanism for North Atlantic SST influence on the Indian summer monsoon. *Geophysical Research Letters*, 33, 356-360
- Grinsted, A. (2013). An estimate of global glacier volume. *The Cryosphere*, 7, 141-151
- Guo, W., Liu, S., Xu, J., Wu, L., Shangguan, D., Yao, X., et al. (2015). The second Chinese glacier inventory: data, methods and results. *Journal of Glaciology*, 61, 357-372
- Hall, D.K., Riggs, G.A., & Salomonson, V.V. (1995a). Development of methods for mapping global snow cover using moderate resolution imaging spectroradiometer data. *Remote Sensing of Environment*, 54, 127-140
- Hall, D.K., Foster, J.L., Chien, J.Y.L., & Riggs, G.A. (1995b). Determination of actual snow-covered area using Landsat TM and digital elevation model data in Glacier National Park, Montana. *Polar Record*, 31, 191
- Hansen, J., Ruedy, R., Sato, M., & Lo, K. (2010). Global surface temperature change. *Reviews of Geophysics*, 48, 7362-7388
- Hansen, J., Sato, M., Ruedy, R., Lo, K., Lea, D.W., & Medina-Elizade, M. (2006). Global temperature change. *Proceedings of the National Academy of Sciences of the United States of America*, 103, 14288-14293
- Helsen, M.M., van den Broeke, Michiel R, van de Wal, Roderik SW, van de Berg, Willem Jan, van Meijgaard, E., Davis, C.H., et al. (2008). Elevation changes in Antarctica mainly determined by accumulation variability. *Science*, 320, 1626-1629
- Hewitt, K. (2005). The Karakoram anomaly? Glacier expansion and the elevation effect, Karakoram Himalaya. *Mountain Research and Development*, 25, 332-340
- Huang, M. (1995). The climatic conditions of polar-type glaciers development in china. *Chinese Geographical Science*, 5, 97-103
- Hurrell, J.W., & Van Loon, H. (1997). Decadal variations in climate associated with the North Atlantic Oscillation. *Climatic Change*, 36, 301-326
- Huss, M. (2011). Present and future contribution of glacier storage change to runoff from macroscale drainage basins in Europe. *Water Resources Research*, 47, W07511
- Immerzeel, W.W., van Beek, L.P., & Bierkens, M.F. (2010). Climate change will affect the Asian water towers. *Science*, 328, 1382-1385
- Immerzeel, W.W., Droogers, P., De Jong, S., & Bierkens, M. (2009). Large-scale monitoring of snow cover and runoff simulation in Himalayan river basins using remote sensing. *Remote Sensing of Environment*, 113, 40-49
- Jacob, T., Wahr, J., Pfeffer, W.T., & Swenson, S. (2012). Recent contributions of glaciers and ice caps to sea level rise. *Nature*, 482, 514-518

- Jiang, M., Ding, X., Hanssen, R.F., Malhotra, R., & Chang, L. (2015). Fast Statistically Homogeneous Pixel Selection for Covariance Matrix Estimation for Multitemporal InSAR. *IEEE Transactions on Geoscience & Remote Sensing*, 53, 1213-1224
- Jiang, Z., Liu, S., Wang, X., Lin, J., & Long, S. (2011). Applying SAR interferometric coherence to outline debris-covered glacier. *Geoinformatics, 2011 19th International Conference on*, 1-4
- Jun, D. (2001). Change of Temperature in Tibetan Plateau From 1961 to 2000 [J]. *Acta Geographica Sinica*, 6, 006
- Kääb, A., Berthier, E., Nuth, C., Gardelle, J., & Arnaud, Y. (2012). Contrasting patterns of early twenty-first-century glacier mass change in the Himalayas. *Nature*, 488, 7412-498
- Kalnay, E., Kanamitsu, M., Kistler, R., Collins, W., Deaven, D., Gandin, L., et al. (1996). The NCEP/NCAR 40-year reanalysis project. *Bulletin of the American Meteorological Society*, 77, 437-471
- Kang, S., Xu, Y., You, Q., Flügel, W., Pepin, N., & Yao, T. (2010). Review of climate and cryospheric change in the Tibetan Plateau. *Environmental Research Letters*, 5, 015101
- Kang, S., Qin, D., Ren, J., Zhang, Y., Kaspari, S., Mayewski, P.A., et al. (2007). Annual accumulation in the Mt. Nyainqentanglha ice core, Southern Tibetan Plateau, China: Relationships to atmospheric circulation over Asia. *Arctic, Antarctic, and Alpine Research*, 39, 663-670
- Kang, S., Mayewski, P., Qin, D., Yan, Y., Hou, S., Zhang, D., et al. (2002). Glaciochemical records from a Mt. Everest ice core: relationship to atmospheric circulation over Asia. *Atmospheric Environment*, 36, 3351-3361
- Kang, X., & Xie, Y. (1989). The character of the weather and climate in the West Kunlun Mountains area in summer, 1987. *Bulletin of glacier Research*, 7, 77-81
- Karimi, N., Farokhnia, A., Karimi, L., Eftekhari, M., & Ghalkhani, H. (2012). Combining optical and thermal remote sensing data for mapping debris-covered glaciers (Alamkouh Glaciers, Iran). *Cold Regions Science and Technology*, 71, 73-83
- Kaser, G., Cogley, J., Dyurgerov, M., Meier, M., & Ohmura, A. (2006). Mass balance of glaciers and ice caps: Consensus estimates for 1961–2004. *Geophysical Research Letters*, 33, L19501
- Kehrwald, N.M., Thompson, L.G., Tandong, Y., Mosley-Thompson, E., Schotterer, U., Alfimov, V., et al. (2008). Mass loss on Himalayan glacier endangers water resources. *Geophysical Research Letters*, 35, 113-130
- Koji, F., Ageta, Y., Pu, J., & Yao, T. (2000). Mass balance of Xiao Dongkemadi glacier on the central Tibetan Plateau from 1989 to 1995. *Annals of Glaciology*, 31, 159-163
- Kumar, K.K., Rajagopalan, B., & Cane, M.A. (1999). On the weakening relationship between the Indian monsoon and ENSO. *Science*, 284, 2156-2159
- Kutzbach, J., Prell, W., & Ruddiman, W.F. (1993). Sensitivity of Eurasian climate to surface uplift of the Tibetan Plateau. *The Journal of geology*, 101, 177-190

- Leonard, K.C., & Fountain, A.G. (2003). Map-based methods for estimating glacier equilibrium-line altitudes. *Journal of Glaciology*, *49*, 329-336
- Li, C., & Cheng, P. (1978). Recent research on glaciers on the Chinghai-Tibet Plateau. *Proceedings of the Riederalp Workshop*, *126*, 121-127
- Li, J., & Zeng, Q. (2002). A unified monsoon index. *Geophysical Research Letters*, *29*, 1274
- Li, J., Wu, Z., Jiang, Z., & He, J. (2010a). Can global warming strengthen the East Asian summer monsoon? *Journal of Climate*, *23*, 6696-6705
- Li, S., & Shi, Y. (1991). Glacial and lake fluctuations in the area of the West Kunlun Mountains during the last 45 000 years. *Annals of Glaciology*, *16*, 79-84
- Li, X., Cheng, G., Jin, H., Kang, E., Che, T., Jin, R., et al. (2008). Cryospheric change in China. *Global and Planetary Change*, *62*, 210-218
- Li, Z., Xing, Q., Liu, X., Zhou, J., & Huang, L. (2010b). Monitoring thickness and volume changes of the Dongkemadi Ice Field on the Qinghai-Tibetan Plateau (1969–2000) using Shuttle Radar Topography Mission and map data. *International Journal of Digital Earth*, *5*, 516-532
- Li, C., Yang, T., & Tian, H. (2013). Variation of West Kunlun Mountains glacier during 1990-2011. *Progress in Geography*, *32*, 548-559
- Lioubimtseva, E., Cole, R., Adams, J., & Kapustin, G. (2005). Impacts of climate and land-cover changes in arid lands of Central Asia. *Journal of Arid Environments*, *62*, 285-308
- Liu, X., & Yin, Z. (2002). Sensitivity of East Asian monsoon climate to the uplift of the Tibetan Plateau. *Palaeogeography, Palaeoclimatology, Palaeoecology*, *183*, 223-245
- Liu, X., & Chen, B. (2000). Climatic warming in the Tibetan Plateau during recent decades. *International Journal of Climatology*, *20*, 1729-1742
- Liu, X., Yin, Z., Shao, X., & Qin, N. (2006). Temporal trends and variability of daily maximum and minimum, extreme temperature events, and growing season length over the eastern and central Tibetan Plateau during 1961–2003. *Journal of Geophysical Research: Atmospheres (1984–2012)*, *111*
- Liu, S., Sun, W., Shen, Y., & Li, G. (2003). Glacier changes since the Little Ice Age maximum in the western Qilian Shan, northwest China, and consequences of glacier runoff for water supply. *Journal of Glaciology*, *49*, 117-124
- Long, D., Scanlon, B.R., Longuevergne, L., Sun, A.Y., Fernando, D.N., & Save, H. (2013). GRACE satellite monitoring of large depletion in water storage in response to the 2011 drought in Texas. *Geophysical Research Letters*, *40*, 3395-3401
- Lu, A., Yao, T., Liu, S., Ding, L., & Li, G. (2002). Glacier change in the Geladandong area of the Tibetan Plateau monitored by remote sensing. *Journal of Glaciology and Geocryology*, *24*, 559-562
- Massif, K.Y., & Ladakh, N.I. (2012). Changes of High Altitude Glaciers from 1969 to 2010 in the Trans-Himalayan. *Arctic, Antarctic, and Alpine Research*, *44*, 107-121

- Matsuo, K., & Heki, K. (2010). Time-variable ice loss in Asian high mountains from satellite gravimetry. *Earth and Planetary Science Letters*, 290, 30-36
- Maussion, F., Scherer, D., Mölg, T., Collier, E., Curio, J., & Finkelburg, R. (2014). Precipitation Seasonality and Variability over the Tibetan Plateau as Resolved by the High Asia Reanalysis*. *Journal of Climate*, 27, 1910-1927
- McFeeters, S. (1996). The use of the Normalized Difference Water Index (NDWI) in the delineation of open water features. *International Journal of Remote Sensing*, 17, 1425-1432
- Memarsadeghi, N., Mount, D.M., Netanyahu, N.S., & Le Moigne, J. (2007). A fast implementation of the ISODATA clustering algorithm. *International Journal of Computational Geometry & Applications*, 17, 71-103
- Mölg, T., Maussion, F., & Scherer, D. (2013). Mid-latitude westerlies as a driver of glacier variability in monsoonal High Asia. *Nature Climate Change*, 4, 68-73
- Molnar, P., & Tapponnier, P. (1978). Active tectonics of Tibet. *Journal of Geophysical Research: Solid Earth (1978–2012)*, 83, 5361-5375
- Narama, C., Kääb, A., Duishonakunov, M., & Abdrakhmatov, K. (2010). Spatial variability of recent glacier area changes in the Tien Shan Mountains, Central Asia, using Corona (~1970), Landsat (~2000), and ALOS (~2007) satellite data. *Global and Planetary Change*, 71, 42-54
- Neckel, N., Kropáček, J., Bolch, T., & Hochschild, V. (2014). Glacier mass changes on the Tibetan Plateau 2003–2009 derived from ICESat laser altimetry measurements. *Environmental Research Letters*, 9, 014009
- New, M., Hulme, M., & Jones, P. (2000). Representing twentieth-century space-time climate variability. Part II: Development of 1901-96 monthly grids of terrestrial surface climate. *Journal of Climate*, 13, 2217-2238
- Niu, T., Chen, L., & Zhou, Z. (2004). The characteristics of climate change over the Tibetan Plateau in the last 40 years and the detection of climatic jumps. *Advances in Atmospheric Sciences*, 21, 193-203
- Oerlemans, J., & Fortuin, J.P. (1992). Sensitivity of glaciers and small ice caps to greenhouse warming. *Science*, 258, 115-117
- Ohmura, A. (2010). Completing the world glacier inventory. *Annals of Glaciology*, 50, 144-148
- Paul, F., Huggel, C., Kääb, A., Kellenberger, T., & Maisch, M. (2002a). Comparison of TM-derived glacier areas with higher resolution data sets. In *EARSeL eProceedings, Bern, Norway*, 2, 15-21
- Paul, F., Kaab, A., Maisch, M., Kellenberger, T., & Haeberli, W. (2002b). The new remote-sensing-derived Swiss glacier inventory: I. Methods. *Annals of Glaciology*, 34, 355-361
- Paul, F., Huggel, C., & Kääb, A. (2004). Combining satellite multispectral image data and a digital elevation model for mapping debris-covered glaciers. *Remote Sensing of Environment*, 89, 510-518

- Paul, F., Barrand, N., Baumann, S., Berthier, E., Bolch, T., Casey, K., et al. (2013). On the accuracy of glacier outlines derived from remote-sensing data. *Annals of Glaciology*, *54*, 171-182
- Paul, F., Bolch, T., Kääb, A., Nagler, T., Nuth, C., Scharrer, K., et al. (2015). The glaciers climate change initiative: Methods for creating glacier area, elevation change and velocity products. *Remote Sensing of Environment*, *162*, 408-426
- Pfeffer, W.T., Sassolas, C., Bahr, D.B., & Meier, M.F. (1998). Response time of glaciers as a function of size and mass balance: 2. Numerical experiments. *Journal of Geophysical Research: Solid Earth (1978–2012)*, *103*, 9783-9789
- Pfeffer, W.T., Arendt, A.A., Bliss, A., Bolch, T., Cogley, J.G., Gardner, A.S., et al. (2014). The Randolph Glacier Inventory: a globally complete inventory of glaciers. *Journal of Glaciology*, *60*, 537
- Pieczonka, T., & Bolch, T. (2015). Region-wide glacier mass budgets and area changes for the Central Tien Shan between ~ 1975 and 1999 using Hexagon KH-9 imagery. *Global and Planetary Change*, *128*, 1-13
- Pu, J., Yao, T., Yang, M., Tian, L., Wang, N., Ageta, Y., et al. (2008). Rapid decrease of mass balance observed in the Xiao (Lesser) Dongkemadi Glacier, in the central Tibetan Plateau. *Hydrological Processes*, *22*, 2953-2958
- Purdie, H., Mackintosh, A., Lawson, W., Anderson, B., Morgenstern, U., Chinn, T., et al. (2011). Interannual variability in net accumulation on Tasman Glacier and its relationship with climate. *Global and Planetary Change*, *77*, 142-152
- Quan, X., Diaz, H.F., & Hoerling, M.P. (2004). Changes in the tropical Hadley cell since 1950. *The Hadley Circulation: Present, Past, and Future*, 85-120
- Quincey, D.J., Braun, M., Glasser, N.F., Bishop, M.P., Hewitt, K., & Luckman, A. (2011). Karakoram glacier surge dynamics. *Geophysical Research Letters*, *38*, 1/8/2014
- Rabus, B., Eineder, M., Roth, A., & Bamler, R. (2003). The shuttle radar topography mission—a new class of digital elevation models acquired by spaceborne radar. *ISPRS Journal of Photogrammetry and Remote Sensing*, *57*, 241-262
- Racoviteanu, E.A., Williams, W.M., & Barry, G.R. (2008a). Optical Remote Sensing of Glacier Characteristics: A Review with Focus on the Himalaya. *Sensors*, *8*, 3355-3383
- Racoviteanu, E.A., Yves, A., Williams, W.M., & Ordonez, J. (2008b). Decadal changes in glacier parameters in the Cordillera Blanca, Peru, derived from remote sensing. *Journal of Glaciology*, *54*, 499-510
- Raible, C., Yoshimori, M., Stocker, T., & Casty, C. (2007). Extreme midlatitude cyclones and their implications for precipitation and wind speed extremes in simulations of the Maunder Minimum versus present day conditions. *Climate Dynamics*, *28*, 409-423
- Ramillien, G., Lombard, A., Cazenave, A., Ivins, E., Llubes, M., Remy, F., et al. (2006). Interannual variations of the mass balance of the Antarctica and Greenland ice sheets from GRACE. *Global and Planetary Change*, *53*, 198-208

- Rangwala, I., Miller, J.R., & Xu, M. (2009). Warming in the Tibetan Plateau: possible influences of the changes in surface water vapor. *Geophysical Research Letters*, *36*, 295-311
- Rangwala, I., Miller, J.R., Russell, G.L., & Xu, M. (2010). Using a global climate model to evaluate the influences of water vapor, snow cover and atmospheric aerosol on warming in the Tibetan Plateau during the twenty-first century. *Climate Dynamics*, *34*, 859-872
- Raup, B., Kääb, A., Kargel, J.S., Bishop, M.P., Hamilton, G., Lee, E., et al. (2007). Remote sensing and GIS technology in the Global Land Ice Measurements from Space (GLIMS) project. *Computers & Geosciences*, *33*, 104-125
- Ren, Z., Zhang, M., Wang, S., Qiang, F., Zhu, X., & Dong, L. (2015). Changes in daily extreme precipitation events in South China from 1961 to 2011. *Journal of Geographical Sciences*, *25*, 58-68
- Riggs, G.A., Hall, D.K., & Salomonson, V.V. (2006). MODIS Snow Products User Guide to Collection 5. 2013, 80
- Rignot, E., Rivera, A., & Casassa, G. (2003). Contribution of the Patagonia Icefields of South America to sea level rise. *Science*, *302*, 434-437
- Rivera, A., Benham, T., Casassa, G., Bamber, J., & Dowdeswell, J.A. (2007). Ice elevation and areal changes of glaciers from the Northern Patagonia Icefield, Chile. *Global and Planetary Change*, *59*, 126-137
- Royden, L.H., Burchfiel, B.C., & van der Hilst, R.D. (2008). The geological evolution of the Tibetan Plateau. *Science*, *321*, 1054-1058
- Sauber, J., Molnia, B., Carabajal, C., Luthcke, S., & Muskett, R. (2005). Ice elevations and surface change on the Malaspina Glacier, Alaska. *Geophysical Research Letters*, *32*, L23S01
- Scherler, D., Bookhagen, B., & Strecker, M.R. (2011). Spatially variable response of Himalayan glaciers to climate change affected by debris cover. *Nature geoscience*, *4*, 156-159
- Schneider, P., Hook, S., Radocinski, R., Corlett, G., Hulley, G., Schladow, S., et al. (2009). Satellite observations indicate rapid warming trend for lakes in California and Nevada. *Geophysical Research Letters*, *36*, L22402
- Screen, J.A., & Simmonds, I. (2013). Exploring links between Arctic amplification and mid-latitude weather. *Geophysical Research Letters*, *40*, 959-964
- Shaman, J., & Tziperman, E. (2005). The effect of ENSO on Tibetan Plateau snow depth: A stationary wave teleconnection mechanism and implications for the South Asian monsoons. *Journal of Climate*, *18*, 2067-2079
- Shangguan, D., Liu, S., Ding, Y., Zhang, Y., Du, E., & Wu, Z. (2008). Thinning and retreat of Xiao Dongkemadi glacier, Tibetan Plateau, since 1993. *Journal of Glaciology*, *54*, 949-951
- Shangguan, D., Liu, S., Ding, Y., Li, j., Zhang, Y., Ding, L., et al. (2007). Glacier changes in the west Kunlun Shan from 1970 to 2001 derived from Landsat TM/ETM and Chinese glacier inventory data. *Annals of Glaciology*, *46*, 204-208

- Sharp, M. (1988). Surging glaciers behaviour and mechanisms. *Progress in Physical Geography*, 12, 349-370
- Shen, F., Royden, L.H., & Burchfiel, B.C. (2001). Large-scale crustal deformation of the Tibetan Plateau. *Journal of Geophysical Research: Solid Earth (1978–2012)*, 106, 6793-6816
- Shen, Y. (2004). An overview of glaciers, retreating glaciers and their impact in the Tibetan Plateau. *World Wildlife Fed. Beijing, China*
- Shen, Y., & Xiong, A. (2015). Validation and comparison of a new gauge-based precipitation analysis over mainland China. *International Journal of Climatology*, 36, 252-165
- Shi, Y., & Liu, S. (2000). Estimation on the response of glaciers in China to the global warming in the 21st century. *Chinese Science Bulletin*, 45, 668-672
- Shi, Y., Liu, C., & Kang, E. (2010). The glacier inventory of China. *Annals of Glaciology*, 50, 1-4
- Shi, Y., Huang, M., Yao, T., & Deng, Y. (2000). Glaciers and their environments in China—the present, past and future. *Beijing: Science Press*, 1-420
- Shukla, A., Gupta, R., & Arora, M. (2010). Delineation of debris-covered glacier boundaries using optical and thermal remote sensing data. *Remote Sensing Letters*, 1, 11-17
- Shuman, C.A., Zwally, H.J., Schutz, B.E., Brenner, A.C., DiMarzio, J.P., Suchdeo, V.P., et al. (2006). ICESat Antarctic elevation data: Preliminary precision and accuracy assessment. *Geophysical Research Letters*, 33, L07501
- Siegfried, M.R., Hawley, R.L., & Burkhart, J.F. (2011). High-Resolution Ground-Based GPS Measurements Show Intercampaign Bias in ICESat Elevation Data Near Summit, Greenland. *IEEE Transactions on Geoscience and Remote Sensing*, 49, 3393-3400
- Simmons, A., Uppala, S., Dee, D., & Kobayashi, S. (2007). ERA-Interim: New ECMWF reanalysis products from 1989 onwards. *ECMWF newsletter*, 110, 25-35
- Slobbe, D., Lindenbergh, R., & Ditmar, P. (2008). Estimation of volume change rates of Greenland's ice sheet from ICESat data using overlapping footprints. *Remote Sensing of Environment*, 112, 4204-4213
- Smith, B.E., Bentley, C.R., & Raymond, C.F. (2005). Recent elevation changes on the ice streams and ridges of the Ross Embayment from ICESat crossovers. *Geophysical Research Letters*, 32, L21S09
- Song, C., Ke, L., Huang, B., & Richards, K.S. (2015). Can mountain glacier melting explains the GRACE-observed mass loss in the southeast Tibetan Plateau: From a climate perspective? *Global and Planetary Change*, 124, 1-9
- Song, C., Huang, B., Richards, K., Ke, L., & Hien Phan, V. (2014). Accelerated lake expansion on the Tibetan Plateau in the 2000s: Induced by glacial melting or other processes? *Water Resources Research*, 50, 3170-3186
- Storey, J., Choate, M., & Lee, K. (2014). Landsat 8 Operational Land Imager On-Orbit Geometric Calibration and Performance. *Remote Sensing*, 6, 11127-11152

- Su, Z., & Shi, Y. (2002). Response of monsoonal temperate glaciers to global warming since the Little Ice Age. *Quaternary International*, 97, 123-131
- Tang, M., Cheng, G., & Lin, Z. (1998). *Contemporary Climatic Variations over Qinghai-Xizang (Tibetan) Plateau and Their Influences on Environments*. (pp. 339-190-193;130-131). Guangzhou: Guangdong Science and Technology Press
- Taschner, S., & Ranzi, R. (2002). Comparing the opportunities of Landsat-TM and Aster data for monitoring a debris covered glacier in the Italian Alps within the GLIMS project. *Geoscience and Remote Sensing Symposium (IGARSS), IEEE International*, 2, 1044-1046
- Thompson, L.G., Yao, T.D., Davis, M.E., Mosley-Thompson, E., Mashiotta, T.A., Lin, P.N., et al. (2006). Holocene climate variability archived in the Puruogangri ice cap on the central Tibetan Plateau. *Annals of Glaciology*, 43, 61-69
- Tian, L., Yao, T., MacClune, K., White, J., Schilla, A., Vaughn, B., et al. (2007). Stable isotopic variations in west China: A consideration of moisture sources. *Journal of Geophysical Research: Atmospheres (1984–2012)*, 112
- Trenberth, K.E., & Hurrell, J.W. (1994). Decadal atmosphere-ocean variations in the Pacific. *Climate Dynamics*, 9, 303-319
- U.S. Geological Survey. (2013). Landsat 8: U.S. Geological Survey Fact Sheet 2013–3060.
- Veetil, B.K. (2012). A Remote sensing approach for monitoring debris-covered glaciers in the high altitude Karakoram Himalayas. *International Journal of Geomatics & Geosciences*, 2, 833-841
- Wahr, J., Swenson, S., Zlotnicki, V., & Velicogna, I. (2004). Time-variable gravity from GRACE: First results. *Geophysical Research Letters*, 31, 293-317
- Wang, B., Wu, R., & Lau, K. (2001). Interannual Variability of the Asian Summer Monsoon: Contrasts between the Indian and the Western North Pacific-East Asian Monsoons*. *Journal of Climate*, 14, 4073-4090
- Wang, C. (2002). Atmospheric circulation cells associated with the El Niño-Southern Oscillation. *Journal of Climate*, 15, 399-419
- Wang, N., Jiang, X., Thompson, L.G., & Davis, M.E. (2007). Accumulation rates over the past 500 years recorded in ice cores from the northern and southern Tibetan Plateau, China. *Arctic, Antarctic, and Alpine Research*, 39, 671-677
- Wang, N.L., Thompson, L.G., Davis, M.E., Mosley-Thompson, E., Yao, T.D., & Pu, J.C. (2003). Influence of variations in NAO and SO on air temperature over the northern Tibetan Plateau as recorded by $\delta^{18}\text{O}$ in the Malan ice core. *Geophysical Research Letters*, 30, 92-106
- Wegmüller, U., & Werner, C. (1997). Land applications using ERS-1/2 Tandem data. *ESA SP*
- Wu, J., & Gao, X. (2013). A gridded daily observation dataset over China region and comparison with the other datasets. *Chinese Journal of Geophysics*, 56, 1102-1111
- Xavier, L., Becker, M., Cazenave, A., Longuevergne, L., & Llovel, W. (2010). Interannual variability in water storage over 2003–2008 in the Amazon Basin from GRACE space

- gravimetry, in situ river level and precipitation data. *Remote Sensing of Environment*, 114, 1629-1637
- Xu, G., Chen, T., Liu, X., Jin, L., An, W., & Wang, W. (2011). Summer temperature variations recorded in tree-ring $\delta^{13}\text{C}$ values on the northeastern Tibetan Plateau. *Theoretical and applied climatology*, 105, 51-63
- Xu, H., Hong, Y.T., Hong, B., Zhu, Y.X., & Wang, Y. (2010). Influence of ENSO on multi-annual temperature variations at Hongyuan, NE Qinghai-Tibet plateau: evidence from $\delta^{13}\text{C}$ of spruce tree rings. *International Journal of Climatology*, 30, 120-126
- Yang, W., Yao, T., Xu, B., Wu, G., Ma, L., & Xin, X. (2008). Quick ice mass loss and abrupt retreat of the maritime glaciers in the Kangri Karpo Mountains, southeast Tibetan Plateau. *Chinese Science Bulletin*, 53, 2547-2551
- Yang, W., Yao, T., Xu, B., Ma, L., Wang, Z., & Wan, M. (2010). Characteristics of recent temperate glacier fluctuations in the Parlung Zangbo River basin, southeast Tibetan Plateau. *Chinese Science Bulletin*, 55, 2097-2102
- Yao, T., Li, Z., Yang, W., Guo, X., Zhu, L., Kang, S., et al. (2010). Glacial distribution and mass balance in the Yarlung Zangbo River and its influence on lakes. *Chinese Science Bulletin*, 55, 2072-2078
- Yao, T., Wang, Y., Liu, S., Pu, J., & Shen, Y. (2007). Recent glacial retreat in High Asia in China and its impact on water resource in Northwest China. *Science in China Series D: Earth Sciences*, 39, 642-650
- Yao, T., Thompson, L., Yang, W., Yu, W., Gao, Y., Guo, X., et al. (2012). Different glacier status with atmospheric circulations in Tibetan Plateau and surroundings. *Nature Climate Change*, 2, 663-667
- Yasuda, T., & Furuya, M. (2013). Short-term glacier velocity changes at west kunlun shan, northwest tibet, detected by synthetic aperture radar data. *Remote Sensing of Environment*, 128, 87-106
- Ye, Q., Kang, S., Chen, F., & Wang, J. (2006). Monitoring glacier variations on Geladandong mountain, central Tibetan Plateau, from 1969 to 2002 using remote-sensing and GIS technologies. *Journal of Glaciology*, 52, 537 - 545
- Yi, S., & Sun, W. (2014). Evaluation of glacier changes in high-mountain Asia based on 10 year GRACE RL05 models. *Journal of Geophysical Research: Solid Earth*, 119, 2504-2517
- Yin, Z., Lin, Z., & Zhao, X. (2000). Temperature anomalies in central and eastern Tibetan Plateau in relation to general circulation patterns during 1951–1993. *International Journal of Climatology*, 20, 1431-1449
- You, Q., Kang, S., Aguilar, E., & Yan, Y. (2008). Changes in daily climate extremes in the eastern and central Tibetan Plateau during 1961–2005. *Journal of Geophysical Research*, 113, D07101
- You, Q., Min, J., Zhang, W., Pepin, N., & Kang, S. (2014). Comparison of multiple datasets with gridded precipitation observations over the Tibetan Plateau. *Climate Dynamics*, 1-16

- You, Q., Kang, S., Pepin, N., Flügel, W., Sanchez-Lorenzo, A., Yan, Y., et al. (2010). Climate warming and associated changes in atmospheric circulation in the eastern and central Tibetan Plateau from a homogenized dataset. *Global and Planetary Change*, *72*, 11-24
- Zhang, G., Yao, T., Xie, H., Kang, S., & Lei, Y. (2013). Increased mass over the Tibetan Plateau: from lakes or glaciers? *Geophysical Research Letters*, *40*, 2125-2130
- Zhang, L., Guo, H., Ji, P., & Chen, J. (2012). A research of glacier change in West Kunlun through remote sensing. *Geoscience and Remote Sensing Symposium (IGARSS), IEEE International*, 4430-4433
- Zhang, Y., Yao, T., Pu, J., Kang, S., Hou, S., OHTA, T., et al. (1997). The Features of Hydrological Processes in the Dongkemadi River Basin, Tanggula Pass, Tibetan Plateau. *Journal of Glaciology & Geocryology*, *19*, 214-222
- Zhang, W., Li, S., Wu, T., & Pang, Q. (2007). Changes and spatial patterns of the differences between ground and air temperature over the Qinghai-Xizang plateau. *Journal of Geographical Sciences*, *17*, 20-32
- Zhang, W., An, R., Yang, H., & Jiao, K. (1989). Conditions of glacier development and some glacial features in the West Kunlun Mountains. *Bulletin of Glacier Research*, *7*, 49-58
- Zhao, H., Xu, B., Yao, T., Wu, G., Lin, S., Gao, J., et al. (2012). Deuterium excess record in a southern Tibetan ice core and its potential climatic implications. *Climate Dynamics*, *38*, 1791-1803
- Zhisheng, A., Kutzbach, J.E., Prell, W.L., & Porter, S.C. (2001). Evolution of Asian monsoons and phased uplift of the Himalaya–Tibetan plateau since Late Miocene times. *Nature*, *411*, 62-66
- Zhou, B., Xu, Y., Wu, J., Dong, S., & Shi, Y. (2015). Changes in temperature and precipitation extreme indices over China: analysis of a high-resolution grid dataset. *International Journal of Climatology*, *16(48)*, 19-21
- Zhu, Z., Wang, S., & Woodcock, C.E. (2015). Improvement and expansion of the Fmask algorithm: cloud, cloud shadow, and snow detection for Landsats 4–7, 8, and Sentinel 2 images. *Remote Sensing of Environment*, *159*, 269–277
- Zwally, H.J., Schutz, B., Abdalati, W., Abshire, J., Bentley, C., Brenner, A., et al. (2002). ICESat's laser measurements of polar ice, atmosphere, ocean, and land. *Journal of Geodynamics*, *34*, 405-445